Simulation of energy filtered electron microscopy

Holbrook, Owen

Award date:
1998

Awarding institution:
University of Bath

SIMULATION OF ENERGY FILTERED ELECTRON MICROSCOPY

Submitted by Owen Holbrook
for the degree of
Doctor of Philosophy
of the University of Bath
1998

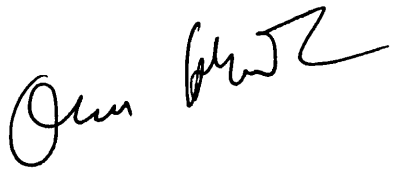

ProQuest LLC
789 East Eisenhower Parkway
P.O. Box 1346
Ann Arbor, MI 48106-1346

Abstract

Energy filtering combined with 2D CCD arrays has been one of the most important developments in electron microscopy in recent years. The theory for elastic scattering has been fully developed for sometime but could not accurately predict experimental scattering intensities due to the large number of inelastic events which occur in real situations. At the same time it was difficult to incorporate inelastic scattering into the theory. Energy filtering leads to much closer correlation between theory and experiment.

Good correlation now depends upon an accurate knowledge of the structure factors for the material under consideration. These values are well known for independent atoms but bonding effects make it more difficult to define them for crystals. Convergent Beam Electron Diffraction (CBED) can be used with a pattern matching technique to obtain these crystal structure factors. However, CBED patterns are complicated and calculation time can be large. The Bethe approximation has been applied and tested as a means of reducing total calculation time. It is demonstrated that it is superior to previous methods and experimental results with Si show that it gives good correlation with known structure factor values from X-ray analysis.

The energy filter can also be used to produce an elemental profile of a particular crystal. In this case it is used to image inelastically scattered electrons, producing a chemical map by imaging the crystal using only the electrons from a set of specific energy losses, corresponding to particular elements. One of the issues relating to chemical mapping is the resolution which can be obtained. It has been shown that it depends upon microscope parameters such as chromatic aberrations and objective aperture size. In this work the underlying physical limit imposed by dynamical diffraction and the excitation process is considered. A model is developed to investigate this by comparing results from an independent atom and one within a crystal. It is shown that the intensity of the image is strongly dependent on the depth of the atom in the crystal due to the intensity of the Bloch wave at that depth and that the inclusion of a crystal produces several fringes. Also, the presence of these fringes make it impossible to create a high resolution image of the crystal using inelastically scattered electrons as claimed [1].

Contents

Acknowledgements

First, I would like to thank my supervisor, David Bird. He has been an inspiration throughout my time at Bath and has always been willing to offer his time and knowledge. He has undoubtedly been the biggest influence in my work.

After this there are many other people who deserve thanks both for their help with my understanding of physics and for making my time at Bath such a pleasurable one. Without listing them all individually, I would like to thank all the theory boys and everyone else who ventured up to level 5.

I must thank SERC and later EPSRC for their financial support.

Finally, I would like to thank Anne for her support, particularly in the last year (or two!) when things were going so slowly.

The prawn is cooked at last!

Chapter 1

Introduction

CCD arrays [2] and energy filtered imaging [3, 4] have revolutionised Transmission Electron Microscopy (TEM). Theory and experiment can now be directly compared in both the elastic and inelastic case. In this thesis we consider a number of areas which imaging Parallel Electron Energy Loss Spectroscopy (PEELS) has opened up for investigation.

1.1 Energy Filtering in the Elastic Scattering Case

Elastic theory can accurately describe the diffraction and image intensities of a crystalline material provided a detail description of the structure being modelled is available, i.e. atomic position, chemical composition, Debye-Waller factor, crystal potential and thickness all need to be known. The element and atomic positions can be found in a variety of ways, e.g. X-ray analysis, but it is much more difficult to determine the distribution of the potential. The potential is described using a Fourier representation, the discrete values being known as structure factors, see section 2.2. The structure factors are known for an independent atom [5]

but the bonding effects in a crystal make these values inaccurate for bulk material.

However, now that theory and experiment can be directly compared it is possible to use a pattern matching technique to find these structure factors. Using a parallel beam of incident electrons will result in only a very limited amount of intensity data being available for matching. If Convergent Beam Electron Diffraction (CBED) is used, see chapter 2 and 3 and [6], then large disks which cover much of the collection area are produced. This allows a better comparison of theory and experiment to be made. Initially, the theoretical model calculates the CBED pattern using the independent atom structure factor values and refines them until the best fit between theory and experiment is found, see chapter 3. Pattern matching can be used to determine these structure factors in one of two ways. Zuo and Spence [7] have developed a technique which uses only a systematic row, where as Bird and Saunders [8] have developed one for use with a zone axis. These techniques are discussed in chapter 3.

The detailed CBED patterns which contain a large amount of dynamical diffraction require a large number of calculations to be performed, particularly for the zone axis technique, see section 3.2.2. This may make the method unattractive as a way of determining these structure factors. Therefore, it is essential to find ways to reduce the calculation time. The largest amount of time is spent calculating the many beam matrix (see chapter 2). These calculations scale as N^3 where N is the order of the matrix. Therefore, if the size of the matrix can be reduced large time savings can be made. Second order perturbation theory has been used to reduce calculation time in the zone axis technique and the Bethe approximation in the systematic row technique.

In chapter 2 the theory for elastic electron diffraction is presented, indicating which approximations are used and why there may be a large number of calculations. In chapter 3 the method of low order structure factor determination is explained and the Bethe approximation is investigated as a means of reducing the calculation time in the Bird and Saunders zone axis method [8]. It is compared to

the second order perturbation theory which has previously been used. Initially, a simple three beam case is considered, being extended to a more realistic system later. The Bethe approximation is found to give accurate answers while needing less calculations than second order perturbation theory. Finally, the pattern matching method of Bird and Saunders, including the Bethe approximation, is used to determine low order structure factors for a Si system and found to give good agreement with X-ray analysis.

1.2 Energy Filtering in the Inelastic Scattering Case

Energy filtering can also be used to study inelastic events by excluding electrons which do not have some specified energy, i.e. those which have either undergone no inelastic scattering or have lost a different amount of energy in the scattering event. If the inelastic event is due to the excitation of an electron from a core state to a higher state then the energy loss will be characteristic of the element. If an image of a crystal is taken at a characteristic energy loss for each element in the crystal then a chemical map of this crystal can be created, see section 4.1.1.

It is known that the microscope aberrations affect the resolution of these maps see [9, 10, 11] and section 4.1.2. However, the underlying physics has been less well investigated, in particular how the dynamical diffraction affects resolution. It is this point which is investigated in chapters 4 and 5. In order to investigate this two models need to be used, one where the atom undergoing excitation is in free space, the other where the atom is surrounded by a crystal, this second model introduces dynamical diffraction effects. These models are developed in chapter 4. A number of approximations are made to ensure that the model is simple and does not add confusing details to the picture. Essentially, we need a source of inelastic electrons but this source does not need to describe the real world precisely. Therefore, the atom is assumed to be hydrogenic and

does not interfere with the surrounding crystal other than to provide a source for the inelastic scattering. The dipole approximation is used in the atomic transition and a single scattering event at the source atom is assumed. These approximations and the others are discussed in more detail in chapter 4.

These approximations are tested in Chapter 5 using the simple free space model. It is found that the dipole approximation does not significantly affect the object functions. The free space model is used to analyse the spatial extent of the object function and how this depends upon transition and energy loss. It is found that even for relatively low energy losses the object function has a half maximum width of only 2Å, indicating that atomic resolution may be possible. The crystal model is then considered and the results compared to the free space model. It is found that the inclusion of a crystal introduces a set of background fringes of atomic lattice spacing which are superimposed on the basic object function. It is also found that by moving the atom in the x-y plane the object function moves in relation to the surrounding fringes, indicating that the interaction between the fast electron and source atom is to some extent localised to within a lattice spacing. Additionally, the intensity of the object function is now dependent upon the depth of the source atom through the crystal. It is shown that this results from the variation of the Bloch wave intensity through the crystal. This variation in the intensities with respect to depth is reduced if a single focus is used, as would be the case in a real system. It was also found that the fringes due to the surrounding crystal reverse as the depth of the source atom changes, it is shown by using a single focus that this is due to changing the position of the focus rather than the depth of the atom.

However, as may be expected using a single focus tends to cause the object functions of the atoms not at the point of focus to spread out. The combination of this spatial spread, the production of fringes and the varying intensity through the depth of the crystal will reduce the level of resolution possible.

It was suggested by Endoh et al [1] that atomic resolution had been achieved

using this inelastic imaging. However, the imaging was not of impurity atoms within a host crystal but of the host crystal itself. It is shown in section 5.4 that the bright spots in an inelastic image of a host crystal are largely made up from the fringes of surrounding crystal columns and do not represent a specific column. Therefore, these pictures cannot be thought of as being atomic imaging.

In chapter 6 these results are reviewed and conclusions drawn.

Chapter 2

Background Theory

In this Chapter some of the basic assumptions and equations that will be used in the rest of the thesis are considered. It begins by assuming the relativistic Schrödinger equation as the governing equation of High Energy Electron Diffraction and introduces the forward scattering (section 2.1) and projected potential (section 2.2) approximations.

These approximations are then used to derive the diffracted wave amplitude (section2.3) and the many beam equations (section 2.4) which allow computation of the intensity of diffracted beams. The effect of inelastic scattering is considered and the resulting absorption effects are included into the theory using the optical potential (section 2.5).

2.1 Forward Scattering Approximation

The work presented here is concerned with experimental conditions where typical electron microscope voltages are of the order of 200keV [12, 13]. At these voltages the electrons travel at $\sim 70\%$ of the speed of light and relativistic corrections must be employed. For this purpose the relativistic Schrödinger equation is used [14]

$$[-\nabla_{\mathbf{r}}^2 + U(\mathbf{r})]\Psi(\mathbf{r}) = k^2\Psi(\mathbf{r}) \tag{2.1}$$

where $U(\mathbf{r})$ is related to the actual crystal potential $V(\mathbf{r})$ by,

$$U(\mathbf{r}) = \frac{2\gamma m_0}{\hbar^2}V(\mathbf{r})$$

and has the units Å^{-2}. m_0 is the rest mass of the electron and γ depends on the accelerating voltage V_0 by $\gamma = 1 + eV_0/m_0c^2$. At accelerating voltages of 200 keV the scattering will be mainly in the forward direction.

The system that will be considered in this work consists of a beam of electrons incident upon a parallel sided crystal at a small angle from the normal. The transverse and longitudinal components of the incident wave vector $\mathbf{k}$ are $\mathbf{K}$ and k_z respectively, see figure 2.1. Experimentally, little difference is found in CBED patterns where the zone axis and surface are not normal to each other so long as the angle remains close to 90 degrees [15]. The diffraction geometry used throughout this thesis is symmetric Laue where the zone axis forms planes perpendicular to the crystal surface [16, 17], see later in this section.

If the wave vector $\mathbf{k}$ of the incident electron is split into transverse and longitudinal components as in figure 2.1 then it should be noted that the transverse wave vector component $\mathbf{K}$ is only a few Å^{-1} while the $\mathbf{k}_z$ component is approximately 250Å^{-1} [18]. If the wavefunction $\Psi(\mathbf{r})$ is split into a rapidly varying function $\exp(ikz)$ and a slowly varying function $\phi(\mathbf{r})$, i.e. $\Psi(\mathbf{r}) = \exp(ikz)\phi(\mathbf{r})$ then equation (2.1) becomes [14],

$$[-\nabla_{\mathbf{R}}^2 + U(\mathbf{r})]\phi(\mathbf{r}) = 2ik\frac{\partial\phi}{\partial z} + \frac{\partial^2\phi}{\partial z^2} \tag{2.2}$$

where $\mathbf{R}$ is the transverse component of $\mathbf{r}$. Since $\phi(\mathbf{r})$ is slowly varying $\partial^2\phi/\partial z^2$ will be small compared to $2ik\partial\phi/\partial z$ and can be neglected and equation (2.2) becomes,

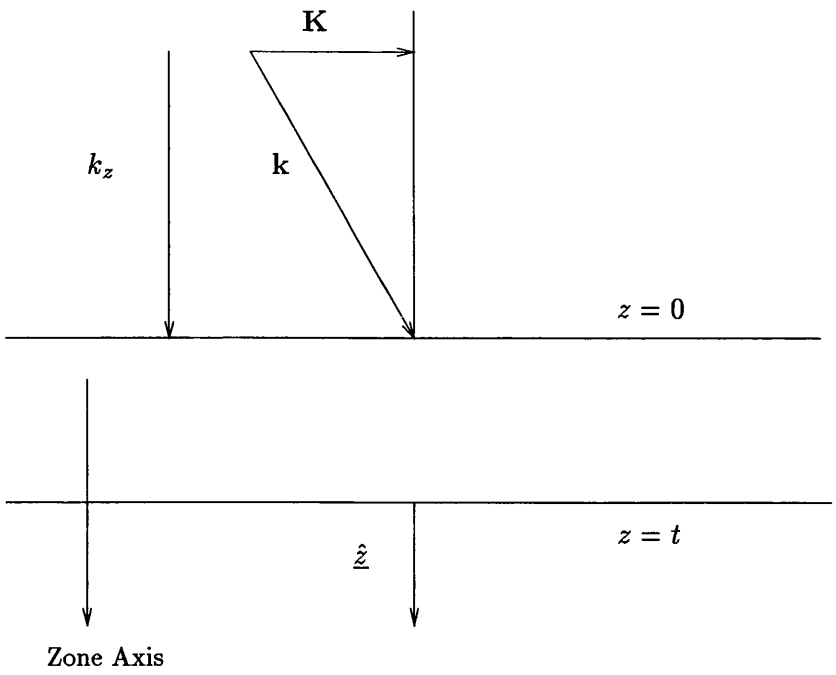

Figure 2.1: Geometry of electron diffraction considered here. The components of incident electron wave vector **k** are **K** in the x-y plane and k_z in the z direction.

$$[-\nabla^2_{\mathbf{R}} + U(\mathbf{r})]\phi(\mathbf{r}) = 2ik\frac{\partial\phi}{\partial z}. \tag{2.3}$$

This is known as the forward scattering approximation. The effect of dropping the second term in equation (2.2) can be seen if the free space solutions are considered, i.e. $U(\mathbf{r}) = 0$. The solutions are then,

$$\begin{aligned} \phi &= \exp[i(\mathbf{K}.\mathbf{R} - K^2 z/2k)]; \\ \Psi &= \exp(i\mathbf{K}.\mathbf{R})\exp[i(k - K^2/2k)z]. \end{aligned} \tag{2.4}$$

In free space the z component of the plane wave should be $k_z = \sqrt{(k^2 - K^2)}$ but in the forward scattering approximation this has been replaced by $k_z = k - K^2/2k$. The free electron sphere has been replaced by a free electron parabola which is an unimportant approximation except for the case of large angle scattering. During

the work presented here this will not be significant since the scattering angles will generally be small.

2.2 Projected Potential Approximation

Equation 2.3 can be further simplified when the form of the potential $U(\mathbf{r})$ is taken into account. In a perfect crystal the potential is periodic with $U(\mathbf{r}+\mathbf{l}) = U(\mathbf{r})$, where $\mathbf{l}$ is any lattice vector. This potential can now be expressed as a Fourier series [18]

$$U(\mathbf{r}) = \sum_{\mathbf{g}} U_{\mathbf{g}} \exp(i\mathbf{g}.\mathbf{r}) \tag{2.5}$$

where $U_{\mathbf{g}}$ is known as the structure factor and is given by

$$U_{\mathbf{g}} = \frac{1}{v_c} \int_{cell} d\mathbf{r} U(\mathbf{r}) \exp(-i\mathbf{g}.\mathbf{r}). \tag{2.6}$$

Here $\mathbf{g}$ is a reciprocal lattice vector and v_c is the volume of the unit cell. When the fast electron is incident along a zone axis the reciprocal lattice points lie in a set of two dimensional layers perpendicular to the incident direction as shown in figure 2.2. Thus, a general reciprocal lattice vector can be written as $\mathbf{g}^{(n)} = (\mathbf{G}, -ng_z)$, where $\mathbf{G}$ is the component perpendicular to the incident electron wave vector $\mathbf{k}$, g_z is the spacing between the layers and n is the layer number. The minus sign in front of n follows the convention of Bird [14] where scattering into the $\mathrm{n^{th}}$ HOLZ layer is due to diffraction by $\mathbf{g}^{(n)}$ rather than $\mathbf{g}^{(-n)}$.

Thus equation (2.5) can be written as,

$$\begin{aligned} U(\mathbf{r}) &= \sum_{n} \exp(-ing_z z) \sum_{\mathbf{G}} U_{\mathbf{g}}^{(n)} \exp(i\mathbf{G}.\mathbf{R}) \\ &= \sum_{n} \exp(-ing_z z) U^{(n)}(\mathbf{R}) \end{aligned} \tag{2.7}$$

where,

$$U^{(n)}(\mathbf{R}) = \sum_{\mathbf{G}} U_{(\mathbf{G},-ng_z)} \exp(i\mathbf{G}.\mathbf{R}). \tag{2.8}$$

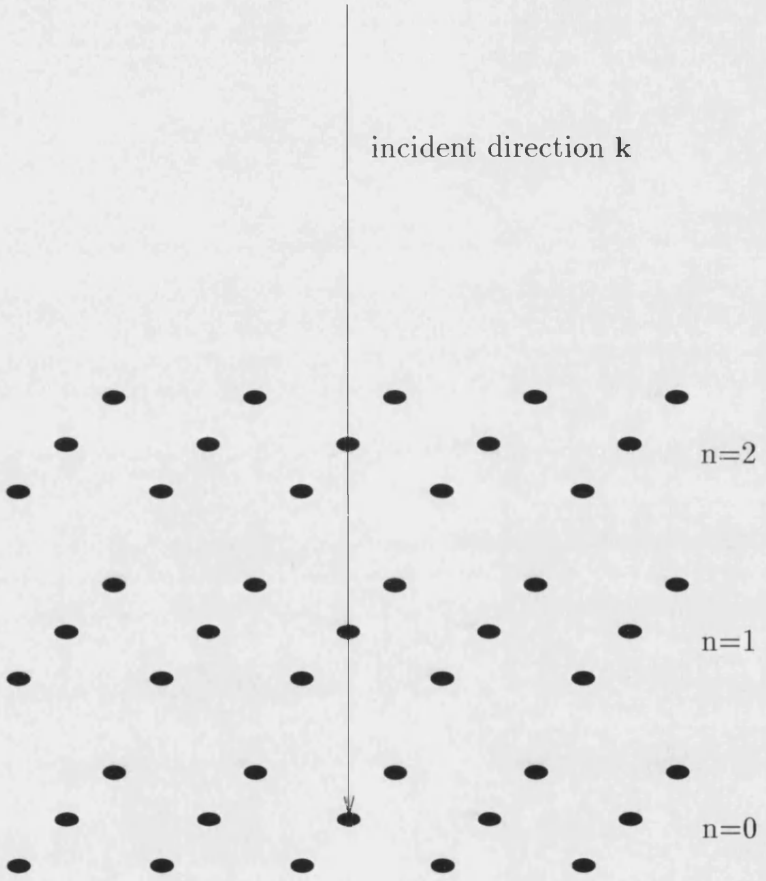

Figure 2.2: When the electron is incident down a zone axis the reciprocal lattice lattice points lie in planes perpendicular to the incident direction.

If $\{\mathbf{L}\}$ is the projection of the real lattice onto a plane then the zero layer of the reciprocal lattice of figure 2.2, $\{\mathbf{G}\}$, is reciprocal to $\{\mathbf{L}\}$. The projection of a real lattice unit cell has an area of A_c. As indicated by equations (2.7) and (2.8) each of the n layers contributes a two dimensional potential. These $U^{(n)}$'s are known as conditional projected potentials and are described in detail in [19]. The potential associated with the zero layer $U^{(0)}(\mathbf{R})$ is known as the projected potential and is the full crystal potential projected down the zone axis under consideration onto a two dimensional plane. It follows that [20],

$$U^{(0)}(\mathbf{R}) = \frac{1}{d}\int_0^d U(\mathbf{r})\mathrm{d}z, \tag{2.9}$$

where d is the repeat distance along the zone axis direction and is given by $d = 2\pi/g_z$. $U^0(\mathbf{R})$ is then given by,

$$U^0(\mathbf{R}) = \sum_{\mathbf{G}} U_{\mathbf{G}} \exp(i\mathbf{G}.\mathbf{R}). \tag{2.10}$$

In the projection approximation only the zero layer terms $U^{(0)}(\mathbf{R})$ are used and equation (2.3) becomes [14]

$$[-\nabla^2_{\mathbf{R}} + U^{(0)}(\mathbf{R})]\phi(\mathbf{r}) = 2ik\frac{\partial\phi}{\partial z}. \tag{2.11}$$

This is justified when considering the Ewald sphere construction of figure 2.3. It can be seen that for diffraction into a HOLZ layer $\mathbf{g}$ must be large, resulting in weak scattering. Additionally, a large number of zero layer points lie close to the Ewald sphere while for higher order layers there are comparatively few. This becomes more pronounced as the wave vector $\mathbf{k}$ increases, for an accelerating voltage of 200keV the difference in the number of points and size of the $\mathbf{g}$ vector would be considerably larger than indicated by figure 2.3.

It should be noted, however, that HOLZ effects are seen and can be quite sig-

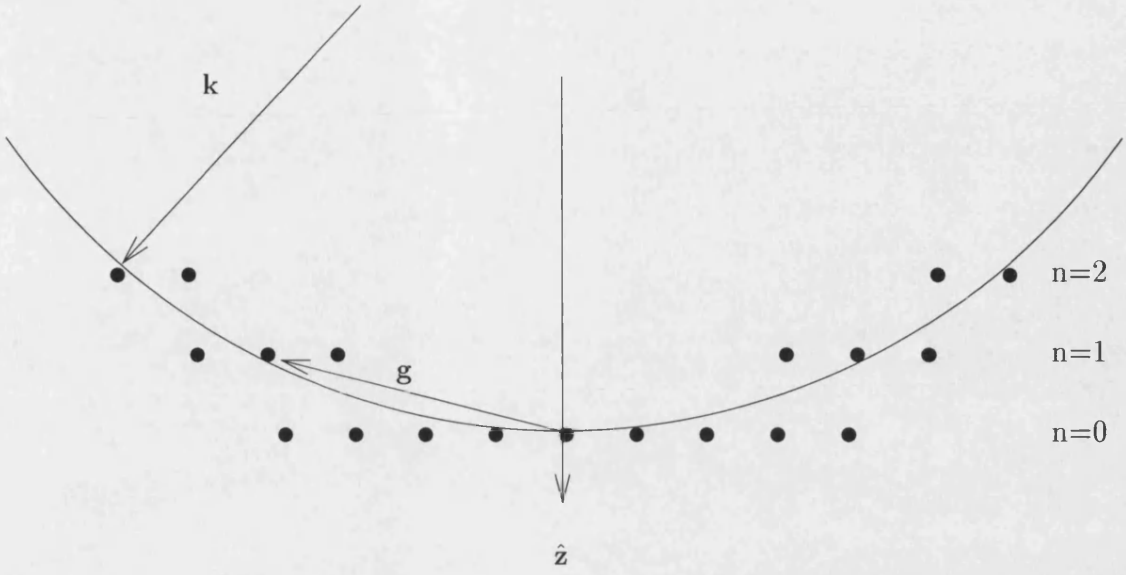

Figure 2.3: Ewald sphere construction showing that large **g** vectors are required for HOLZ scattering. In reality the differences are much larger than shown here.

nificant if the geometry of the problem is right. In the work presented here, the geometries have been chosen so as to minimise HOLZ effects and so no detailed description is given.

2.3 Diffracted Wave Amplitude

Equation 2.11 is separable since the terms $-\nabla^2_{\mathbf{R}} + U^{(0)}(\mathbf{R})$ are not dependent upon z. Substituting $\phi(\mathbf{R}, z)$ with $\tau(\mathbf{R}).Z(z)$ results in the equations,

$$[-\nabla^2_{\mathbf{R}} + U^{(0)}(\mathbf{R})]\tau_m(\mathbf{R}) = s_m\tau_m(\mathbf{R}) \tag{2.12}$$

and

$$2ik\frac{\partial Z_m}{\partial z} = s_m Z_m \tag{2.13}$$

where s_m is the separation constant with the subscript m used to identify different

solutions. Equation 2.13 can be solved to give $Z_m = \exp(-is_m z/2k)$ and gives as the general solution,

$$\begin{aligned} \phi(\mathbf{R}, z) &= \sum_m \epsilon_m \phi_m \\ &= \sum_m \epsilon_m \tau_m(\mathbf{R}) \exp(-is_m z/2k) \end{aligned} \tag{2.14}$$

where ϵ_m are a set of expansion coefficients.

Equation 2.12 is like a two-dimensional time independent Schrödinger equation, $\hat{H}\Psi = E\Psi$ with a two dimensional Hamiltonian $\hat{H} = -\nabla^2_{\mathbf{R}} + U^{(0)}(\mathbf{R})$ and periodic potential $U^{(0)}$. The solutions are Bloch waves as in standard solid state theory [21]. In this case τ_m is generally written as $\tau^j(\mathbf{K}, \mathbf{R})$ where $\mathbf{K}$ is a two dimensional Bloch wave vector and j represents the different bands which are generally referred to as branches in electron diffraction. Similarly s_m is written as $s^j(\mathbf{K})$ and is known as the transverse energy [16] and ϵ_m is written as $\epsilon^j(\mathbf{K})$.

The z dependence of each Bloch state is given through equation (2.14), putting this into the new terminology gives,

$$\phi^j(\mathbf{K}, \mathbf{r}) = \tau^j(\mathbf{K}, \mathbf{R}) \exp[-is^j(\mathbf{K})z/2k] \tag{2.15}$$

or

$$\Psi^j = \exp(ikz)\psi^j = \tau^j \exp[i(k - s^j/2k)z]. \tag{2.16}$$

Each state has a different effective z component of wave vector k_z^j, given by $(k - s^j/2k)$. As $\mathbf{K}$ is varied the resulting changes to k_z^j give the dispersion surface. The total wave function in the crystal must in principle include every distinct state on the dispersion surface and is written as [14],

$$\phi = \sum_{\mathbf{K}} \sum_j \epsilon^j(\mathbf{K}) \tau^j(\mathbf{K}, \mathbf{R}) \exp[-is^j(\mathbf{K})z/2k]. \tag{2.17}$$

The sum over $\mathbf{K}$ is over the first Brillouin zone only. The incident electron wave is given by $\exp(i\mathbf{K_0}.\mathbf{R})$. The expansion coefficients or excitation amplitudes $\epsilon^j(\mathbf{K})$ can be found by matching the incident electron wave to equation (2.17) at the top surface of the crystal, $z = 0$, where $\mathbf{K_0}$ defines the incident orientation of the incoming electron. Noting that only Bloch waves with $\mathbf{K} = \mathbf{K_0}$ can be excited [18], multiplying both sides of equation (2.17) with $\tau^{j*}(\mathbf{K_0}, \mathbf{R})$ and integrating over the projected unit cell gives the excitation amplitude as,

$$\epsilon^j(\mathbf{K_0}) = \frac{1}{A_c} \int_{cell} d\mathbf{R} \exp(i\mathbf{K_0}.\mathbf{R}) \tau^{j*}(\mathbf{K_0}.\mathbf{R}) \tag{2.18}$$

where A_c is the area of the projected unit cell. Using the same criterion for excited Bloch waves the wave function within the crystal simplifies to,

$$\phi = \sum_j \epsilon^j(\mathbf{K_0}) \tau^j(\mathbf{K_0}, \mathbf{R}) \exp[-is^j(\mathbf{K_0})z/2k)]. \tag{2.19}$$

Finally, to find the diffracted wave amplitudes below the crystal it should be noted that each Bloch wave $\tau^j(\mathbf{K_0}, \mathbf{R})$ can only contain Fourier components of $(\mathbf{K_0}+\mathbf{G})$. Since the wave function within the crystal and the diffracted wave below the crystal must be matched the diffracted wave must also have components $(\mathbf{K_0}+\mathbf{G})$. Therefore, the diffracted wave has the form, $\sum_{\mathbf{G}} A_{\mathbf{G}}(\mathbf{K_0}, t) \exp[i(\mathbf{K_0}+\mathbf{G}).\mathbf{R}]$ and the matching equation is,

$$\sum_j \epsilon^j \tau^j \exp(-is^j t/2k) = \sum_{\mathbf{G}} A_{\mathbf{G}}(\mathbf{K_0}, t) \exp[i(\mathbf{K_0} + \mathbf{G}).\mathbf{R}]. \tag{2.20}$$

Here, reference to the depth coordinate z is replaced with thickness t since it will always be at the bottom of the crystal that the matching takes place i.e. $z = t$. $A_{\mathbf{G}}(\mathbf{K_0}, t)$ is the amplitude of each plane wave component below the crystal and is given explicitly by multiplying both sides of equation (2.20) by $\exp[-i(\mathbf{K_0}+\mathbf{G}).\mathbf{R}]$ and integrating over the projected unit cell [14], i.e.

$$A_{\mathbf{G}}(\mathbf{K}_0,t)=\sum_j \epsilon^j \exp(-is^j t/2k)\frac{1}{A_c}\int d\mathbf{R}\tau^j(\mathbf{K}_0,\mathbf{R})\exp[-i(\mathbf{K}_0+\mathbf{G}).\mathbf{R}] \quad (2.21)$$

The intensity below the crystal for a given reflection $\mathbf{G}$ and incident orientation $\mathbf{K}_0$ is given by,

$$I_{\mathbf{G}}(\mathbf{K}_0,t)=|A_{\mathbf{G}}(\mathbf{K}_0,t)|^2. \quad (2.22)$$

2.4 Many Beam Equations

In order to solve equations (2.18), (2.19), (2.21) it is necessary to determine the Bloch waves $\tau(\mathbf{K}_0,\mathbf{R})$, this can be achieved by expanding them in terms of plane waves [21] i.e.,

$$\tau^j(\mathbf{K}_0,\mathbf{R})=\sum_{\mathbf{G}} C^j_{\mathbf{G}}(\mathbf{K}_0)\exp[i(\mathbf{K}_0+\mathbf{G}).\mathbf{R}]. \quad (2.23)$$

$C^j_{\mathbf{G}}$ are the Bloch wave coefficients, giving the amount of each plane wave present in branch j. Substituting this expansion into equation (2.12), multiplying through by $\exp[-i(\mathbf{K}_0+\mathbf{G}).\mathbf{R}]$ and integrating over the projected unit cell gives [14],

$$\sum_{\mathbf{G}}([\mathbf{K}_0+\mathbf{G})^2-s^j(\mathbf{K}_0)]\delta_{\mathbf{G},\mathbf{G}'}+\frac{1}{A_c}\int_{cell} d\mathbf{R}\exp[i(\mathbf{G}-\mathbf{G}').\mathbf{R}]U^{(0)}(\mathbf{R})=0. \quad (2.24)$$

The potential term in the above equation is the structure factor $U_{\mathbf{G}-\mathbf{G}'}$ as given in equation (2.6) and leads to the many beam equations,

$$\sum_{\mathbf{G}}\left([(\mathbf{K}_0+\mathbf{G})^2-s^j(\mathbf{K}_0)]\delta_{\mathbf{G},\mathbf{G}'}+U_{\mathbf{G}'-\mathbf{G}}\right)C^j_{\mathbf{G}}(\mathbf{K}_0)=0. \quad (2.25)$$

This is a standard matrix equation which can be solved by numerical diagonalisation with the incident orientation $\mathbf{K}_0$ being chosen for the system under consideration and the structure factors $U_{\mathbf{G}}$ taken from tabulated form factors [5]. The sum over $U_{\mathbf{G}}$ is infinitely large but the equation converges with an increasing number of $U_{\mathbf{G}}$, for numerical calculations the sum must be truncated at some point, see section 3.4.3. These form factors have been calculated for independent atoms assuming that no electrons are lost from the scattering i.e. there is no absorption (see next section). They are not accurate for atoms within a crystal due to bonding effects but only a few will be significantly altered from the independent atom value, see chapter 3. Thus the excitation amplitudes, wave function and diffracted wave amplitudes are found by substituting equation (2.23) into equations (2.18), (2.19), (2.21) respectively and solving the many beam equation (2.25). Thus, the final expressions, ignoring absorption, are given by,

$$\epsilon^j(\mathbf{K}_0) = C_{\mathbf{0}}^{j*}(\mathbf{K}_0) \tag{2.26}$$

$$\begin{aligned}\phi &= \sum_j \sum_{\mathbf{G}} C_{\mathbf{0}}^{j*}(\mathbf{K}_0) C_{\mathbf{G}}^{j}(\mathbf{K}_0) \exp[i(\mathbf{K}_0 + \mathbf{G}).\mathbf{R}] \\ &\quad \exp[-is^j(\mathbf{K}_0)z/2k]\end{aligned} \tag{2.27}$$

$$A_{\mathbf{G}}(\mathbf{K}_0, t) = \sum_j C_{\mathbf{0}}^{j*} C_{\mathbf{G}}^{j} \exp(-is^j t/2k). \tag{2.28}$$

2.5 Inclusion of Absorption

The above treatment of diffraction does not take into account any inelastic events. These events due to thermal diffuse scattering, atomic electron excitation, plasmons etc. tend to deflect the electrons from their elastic path and away from the Bragg positions. These electrons are said to be absorbed since they do not contribute to the expected intensity for the elastic theory.

To include this effect in a mathematical model it is necessary to find a method by which the Bloch states decay as they proceed through the crystal since the total

number of inelastic events will increase through the crystal. This can be achieved by the inclusion of an imaginary part to the crystal potential so that [22]

$$U(\mathbf{r}) = U^R(\mathbf{r}) + \lambda U^I(\mathbf{r})$$

Various contributions to the imaginary potential $U^I(\mathbf{r})$ have been considered but thermal diffuse scattering is generally assumed to be the most important [23, 24, 25]. Using this assumption Bird and King [26] have tabulated the complex structure factor values. In the rest of this thesis if absorption needs to be taken into account these structure factors will be used, the basic Doyle and Turner [5] values being used otherwise.

The major implication for the theory previously described is that the resulting many beam matrix becomes non-Hermitian and is therefore more difficult to solve [18], with the resulting eigenvalues becoming complex. This is an essential part of the model as the complex eigenvalues cause the Bloch states to decay as they proceed through the crystal, due to the exponential term of equation (2.28) now having an imaginary and real part.

Although it is possible to solve the original Hermitian matrix and calculate the new value for $s^j(\mathbf{K}_0)$ using perturbation theory [18] the work presented here solves the non-Hermitian matrix exactly. The non-Hermitian matrix has two sets of eigenvalue and eigenvector solutions which are found by diagonalising the many beam matrix equation (2.25) and its transpose [27]. The diagonalisation of the transpose of the many beam matrix leads to the production of the left hand set of eigenvectors $\hat{C}^j_{\mathbf{G}}$ which must be introduced into equations (2.27), (2.28) and (2.28) as shown below [28], s^j now being complex,

$$\epsilon^j(\mathbf{K}_0) = \hat{C}^{j*}_{\mathbf{0}}(\mathbf{K}_0) \tag{2.29}$$

$$\phi = \sum_j \sum_{\mathbf{G}} \hat{C}^{j*}_{\mathbf{0}}(\mathbf{K}_0) C^j_{\mathbf{G}}(\mathbf{K}_0) \exp[i(\mathbf{K}_0 + \mathbf{G}).\mathbf{R}] \exp[-is^j(\mathbf{K}_0)z/2k] \tag{2.30}$$

$$A_{\mathbf{G}}(\mathbf{K}_0, t) = \sum_j \hat{C}_{\mathbf{0}}^{j*} C_{\mathbf{G}}^j \exp(-is^j t/2k). \tag{2.31}$$

2.6 Summary

In this chapter the basic equations for high energy electron diffraction and CBED have been given. The relativistic Schrödinger equation was taken for the starting point and the forward scattering and projected potential approximations used to simplify the expressions. The intensity values are given by equations (2.21) and (2.22).

The many beam equations were then derived as a means of calculating equation (2.21) and expressions for the diffracted wave intensity found. Thus computation of CBED patterns can now be performed. Finally, the effects of inelastic scattering were considered and a complex potential expression was introduced. This accounted for the absorption of electrons due to thermal diffuse scattering.

Chapter 3

Convergent Beam Electron Diffraction

In this chapter Convergent Beam Electron Diffraction (CBED) is introduced. It is shown that by matching theoretical and experimental CBED patterns it is possible to determine the low order structure factors of crystals defined in equation (2.6). However, this is a time consuming technique and approximations need to be used to reduce the calculation time.

In section 3.1 Convergent Beam Electron Diffraction (CBED) is introduced and the principle of pattern matching to determine structure factors is explained. Comparisons are made between the two methods of structure factor determination, the zone axis and systematic row techniques, in section 3.2. More details of the zone axis technique are given in section 3.3. The mathematical and computational details of this second method are given in section 3.4 where second order perturbation theory and the Bethe approximation are introduced as possible methods of reducing calculation time. In section 3.5 comparisons are made between these two approximation methods within the zone axis approach. Initially, using a simple three beam case and then using a larger and more realistic system where the Bethe approximation is fully tested. Finally, in section 3.6 the

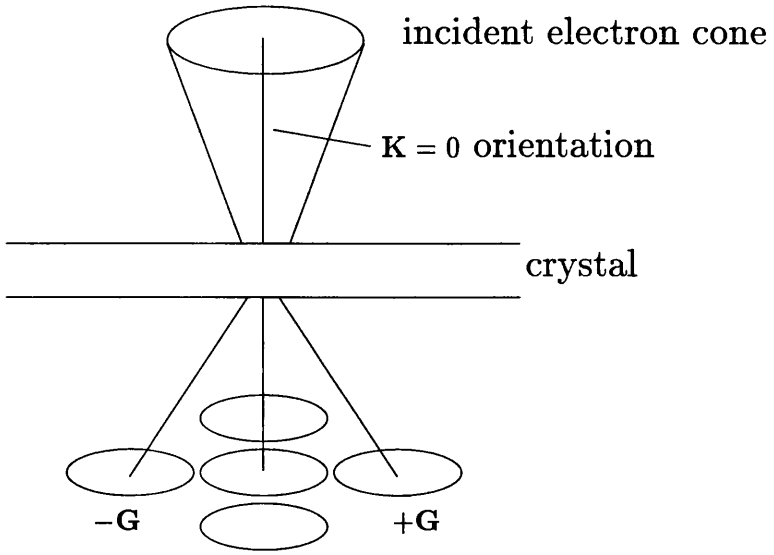

Figure 3.1: Geometry of CBED.

Bethe approximation is applied to an experimental system and the results are shown to give values close to those obtained using X-ray analysis.

3.1 Introduction

In Chapter 2 the governing equations of High Energy Electron Diffraction were derived for an electron of incident wave vector $(\mathbf{K}, k_z)$. In CBED the incident electrons have a range of values for $\mathbf{K}$ or equivalently, a range of incident orientations (see fig 3.1). The resulting diffraction pattern will no longer be a series of spots as in standard diffraction theory [29] but rather a series of discs each corresponding to a particular reflection $\mathbf{G}$ [6]. Every point within each disc corresponds to a particular incident value of $\mathbf{K}$ and for theoretical calculations requires a separate matrix diagonalisation of the many-beam equations (2.25).

Although more complicated to study than standard spot diffraction patterns CBED patterns are useful since they contain far more information. A set of CBED discs for a Si [110] system is shown in figure 3.13 of section 3.6, where the

CBED patterns are used to experimentally determine some low order structure factors for this system. The extra information is due to the range of incident orientations and the resulting differences in diffraction intensities. In order to maximise the information available the microscope user will normally adjust the range of incident orientations until the discs shown in figure 3.1 are almost touching but not overlapping as this would lead to a degradation in the information available from the pattern.

3.1.1 Quantitative CBED

Until quite recently obtaining quantitative results from CBED was not easy due to the non-linear nature of photographic film and the presence of large amounts of inelastically scattered electrons. Thus CBED could only provide qualitative or semi quantitative information such as pattern symmetry and HOLZ line measurements [30, 31], more details of this type of CBED theory and experimental methods can be found in Spence and Zuo [6].

The development of the CCD detector overcame the problem of accurate linear recordings of diffraction patterns, although there are still some issues relating to accurate detection, see section 3.3.2. Even without these issues quantitative CBED was difficult since theoretical models of the diffracted wave amplitude, equation (2.31), assume that all scattering is elastic. There are a number of inelastic processes which can cause the fast electrons to deviate from their elastic path in particular by atomic electron excitation, plasmons and phonons.

Consider first the phonon scattering. The thermal vibration of atoms within the crystal being studied tends to be coupled so that the movement of one atom about its equilibrium point affects the atoms which surround it. Phonons are the representation of this coupled movement of atoms. The fast electron can interact with these vibrations either absorbing energy from or donating energy to them. The scattering angle of the fast electron is usually small but in relation

to high energy electron diffraction the path changes are still significant and can cause background noise both in the CBED discs and between them. The energy change of the fast electron undergoing one of these interactions is usually of the order of 10 meV.

Turning now to the electron excitation, the fast electron may interact with a core or valence atomic electron and give it enough energy to become excited into a higher unfilled state. In this case the fast electron will always lose energy in the process, the size of the energy loss depends upon the atomic transition and may range from a few 10s of eV to $\sim$ 1000 eV. The angle of scattering will tend to be large in comparison to the CBED disc, although this depends on the energy loss, and so produces a background throughout the pattern. The probability of the transition taking place tends to decrease as the energy required to produce the transition increases. A detailed investigation of this process is undertaken in chapters 4 and 5.

Finally, the valence band electrons can move collectively in a similar manner to the phonon case. These collective movements are called plasmons. However, these plasmons do not have a continuous energy range as in the phonon case and typically require the fast electron energy loss to be in the order of 20 eV. The scattering angle tends to be very small with narrow peaks around the Bragg position in a diffraction pattern. This tends to preserve contrast and so, in terms of CBED, are not as important as the other two loss processes described.

These processes are discussed in many articles e.g. [32, 33, 34] but it is a difficult problem to include the exact form in the theory. To some extent the loss of electrons from the purely elastic diffraction patterns due to these inelastic events can be accounted for by the inclusion of an imaginary term to the crystal potential as described in section 2.5. However, quantitative CBED is still difficult due to the introduction of a background of noise from these processes.

Although cooling the sample down to liquid nitrogen temperatures helps to re-

duce the background which results from thermal diffuse (phonon) scattering, accurate quantitative information could not be obtained until energy filtering systems became available [3, 35] which can eliminate the background contributions of plasmon and other electron excitations. These systems, whether serial or parallel, eliminate electrons from the final pattern which have lost more than approximately 5eV of energy in the inelastic process. Although there still remains some inelastic background due to thermal diffuse scattering it can be subtracted using a simple model where the background intensity just outside a disc is measured and this intensity is subtracted from the whole disc [28]. This is not a completely accurate method of accounting for the thermal diffuse scattering but it has been shown that using this method there is good correlation between theoretical elastic patterns and experimentally measured patterns [8]. Figure 3.2 shows an example of the difference between an unfiltered and filtered image for the diamond [110] zone axis pattern at a thickness of 1 μm, the picture was taken by P.A. Midgley at the University of Bristol. The improvement is quite dramatic in this case although it should be noted that diamond is a particularly good material to use this technique on since it suffers from very little thermal diffuse scattering which is the main background component left after filtering.

With energy filtered images it becomes much easier to compare experimental results with theoretical calculations, since the theory now describes much more closely the processes which the electrons have undergone. In order to calculate the theoretical CBED patterns it is necessary to know what the structure factors of the particular crystal are, see chapter 2. However, these are generally unknown for elements in the bulk state and in this chapter we will be concerned with improving a method to determine these bulk values, and therefore determining the bonding charge density.

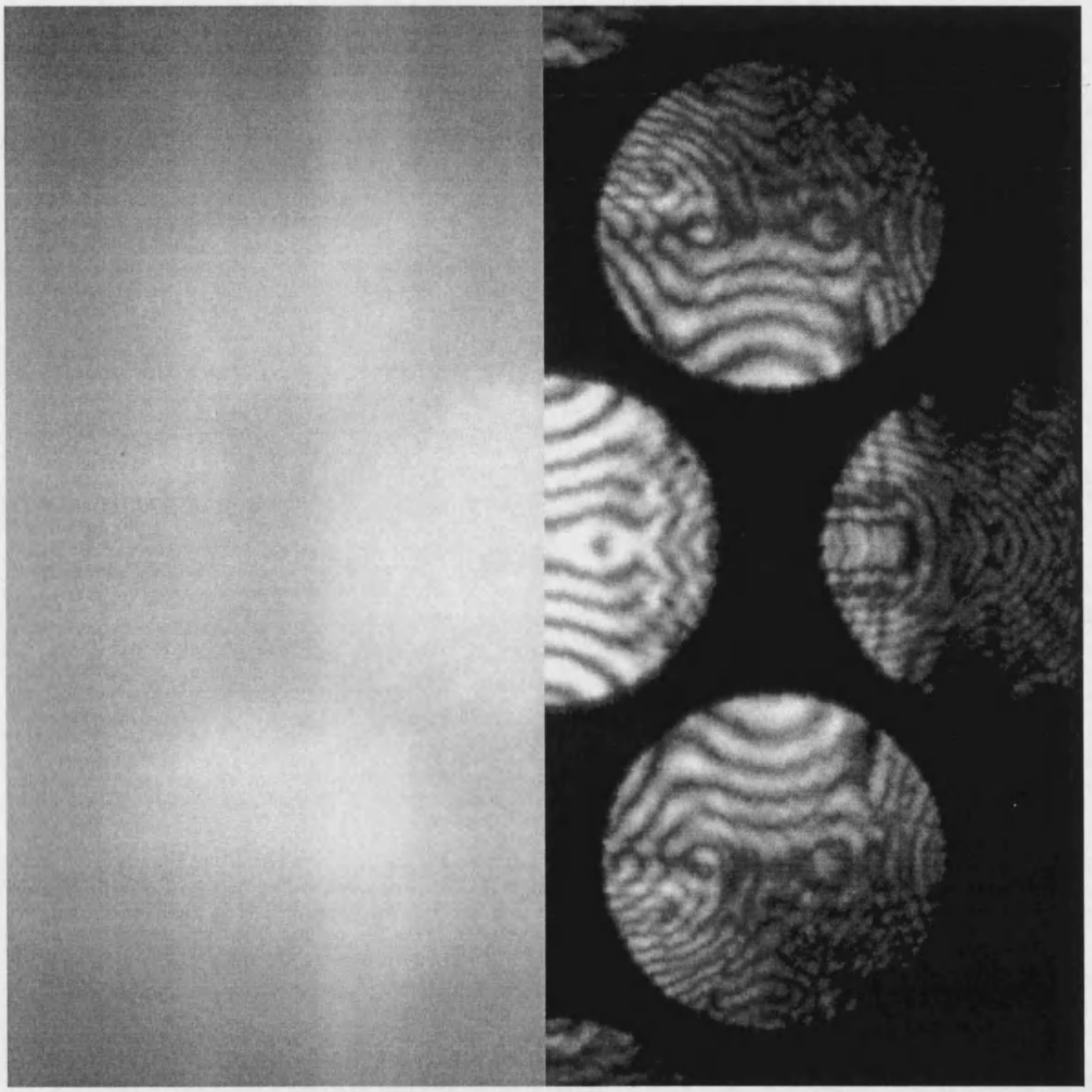

Figure 3.2: The difference between an unfiltered (left) and filtered (right) image of a diamond [110] structure. The improvement is greater than normal since there is very little thermal diffuse scattering present.

3.1.2 Bonding Charge Density

The charge density of independent atoms can be recreated using the tabulated structure factors of Doyle and Turner [5]. However, in a solid the charge becomes redistributed so that the atoms 'bond' together. The change in the independent charge density to the bulk charge density is known as the bonding charge density. If both the independent atom structure factors and the bulk structure factors are known then it is a simple problem to construct the bonding charge density [28]. Understanding these bonding effects can be very important in understanding the properties of materials [36]. The low order structure factors, $U_{\mathbf{g}}$ with small $\mathbf{g}$ (see equation (2.6), are changed the most by this change in charge density [37].

3.1.3 Structure Factor Determination

Before quantitative electron diffraction became possible the method of determining atomic bonding consisted of measuring the differences between the structure factors of the independent atom and the crystal structure using X-ray methods e.g. [38]. However, the nature of X-ray analysis requires that large areas of perfect crystal are available to the experimentalist. With the advent of quantitative electron diffraction much smaller areas could be probed using the CBED technique and the differences between the structure factors of the independent atom and crystal investigated.

However, unlike X-ray analysis electron diffraction results from both the nuclear and electronic component of the charge density with the nuclear component dominating at high spatial frequencies. Therefore, only the low order, $U_{\mathbf{g}}$, structure factors are sensitive to the changes due to the bonding of atoms. Although this is a restriction, the majority of the change in charge density will occur in the low order structure factors and much of the bonding information will be available using this method alone [38].

Within CBED there are two major methods for determining the low order structure factors, the zone axis pattern matching technique of Bird and Saunders [8, 28] and the one dimensional systematic row method of Zuo and Spence [6, 7]. Both of these methods will be discussed in more detail in section 3.2.

They both rely on fitting theoretical data to experimental data with a χ^2 measure of the goodness of fit. The structure factors are adjustable parameters altered to reduce χ^2 to a minimum using either a quasi Newton minimisation routine from the Numerical Algorithms Group (NAG) library [39] (used by Bird and Saunders) or the 'simplex' method [40] (Spence and Zuo). Initial structure factor values are taken from Doyle and Turner for the real part and Bird and King for the imaginary part (incorporating phonon absorption). The zone axis technique is particularly time consuming due to its much larger beam set which is needed to account for the large amount of dynamical diffraction. However, it is able to determine a much larger number of structure factors in one analysis than the systematic row.

3.2 Pattern Matching Technique

A comparison between these two methods will be made in this section, further details of the zone axis method can be found in section 3.3

3.2.1 Systematic Row

In the systematic row approach a line of energy filtered intensity values are taken along the length of a systematic row (see figure 3.3) and the equivalent theoretical intensities calculated using the independent atom structure factors. It is essential that the correct crystal orientation and thickness is used with this method, therefore these parameters are included in the fit. Two and three beam

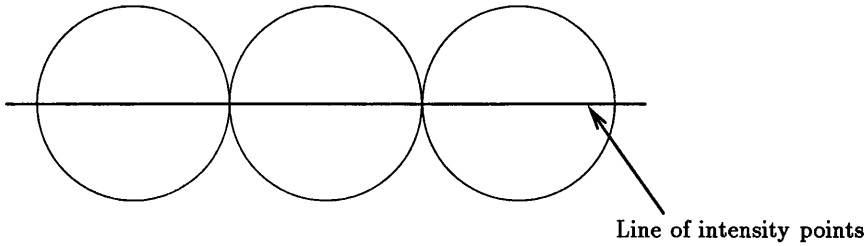

Figure 3.3: Line of intensity points used in the systematic row technique for determining bulk structure factors.

analysis is used to determine which parts of the pattern are most sensitive to the structures factors being considered. Only two structure factors can be considered at one time using this method since the CBED disks will overlap if more than two Bragg angles are included in the incident orientation range of figure 3.1 [6]. The many beam equations (2.25) which must be solved before the theoretical intensities can be calculated are infinite in extent and some finite cut off must be chosen. Typically, $\sim$ 30 beams are enough for a converged pattern in this method [7].

Perturbation theory can be used to reduce the total time taken for the calculation [41]. This involves splitting the total number of beams into two sets, one set being a perturbation on the other.

Once the initial theoretical intensity pattern has been calculated it must be compared with the experimental values, the difference between the patterns is defined using a sum of squares error, χ^2,

$$\chi^2 = \sum_i \frac{f^{(i)}.(cI_{th}^{(i)} - I_{ex}^{(i)})^2}{\sigma_i^2} \tag{3.1}$$

where the sum is over all data points i measured by the CCD. Here, f_i is the weight attached to each point resulting from how sensitive it is to the structure factor under examination, determined by two and three beam analysis. $I_{th}^{(i)}$ and $I_{ex}^{(i)}$ are the values of the theoretical and experimental intensity at i respectively.

σ_i^2 is the variance of the ith point and can either be measured or taken as $I_{ex}^{(i)}$ if Poisson statistics are assumed. c is the normalisation coefficient which ensures that the theoretical values are scaled correctly with respect to the experimental values, it is given by [6],

$$c = \frac{\sum_i f_i/\sigma_i^2 I_{ex}^{(i)} I_{th}^{(i)}}{\sum_i f_i/\sigma_i^2 I_{th}^{(i)} I_{th}^{(i)}}. \tag{3.2}$$

Inelastic background noise can be measured close to the edge of each disk and the intensity subtracted from the experimental data. Since the CCD detector affects the recorded intensity due to the point spread function (see section 3.3) some way of compensating for these differences must be found. In this technique the theoretical data tends to be convoluted with the measured detector response rather than the experimental data being deconvoluted [6, 42]. Having obtained the χ^2 error between the two patterns the theoretical parameters are altered and the pattern recalculated. The 'Simplex' minimisation algorithm [40] is used to minimise the error until χ^2 falls below some predefined limit.

3.2.2 Zone Axis Technique

The zone axis method of Bird and Saunders differs from the systematic row approach in a number of ways. First, the diffraction geometry is different. Rather than choosing a systematic row where only one or two structure factors can be determined a zone axis is used where many diffraction conditions will be included in the incident orientation range without any overlap of discs (this was the condition shown in figure 3.1). This means that there is increased dynamical diffraction of the fast electron wave and, therefore, there will be greater sensitivity to the structure factors under investigation. This also enables a large number of structure factors to be investigated with a single pattern rather than having to record a number of diffraction patterns.

In this method the intensity is measured at points across the whole disk rather than taking a single line of points as before, see section 3.3. Tests have shown that in zone axis patterns there is not a large amount of local sensitivity in a disc to a particular structure factor, therefore, no scaling factor such as that used in the systematic row approach (section 3.2.1) is introduced [28]. As before the same points on the disk are calculated theoretically from the independent atom structure factor values. This time the difference between the experimental and theoretical patterns is given by,

$$\chi^2 = \frac{1}{N_{data}} \sum_{i=1}^{N_{data}} \frac{(I_{ex}^{(i)} - cI_{th}^{(i)} - B_n)^2}{\sigma_i^2}. \tag{3.3}$$

Here I_{ex} and I_{th} are the experimental and theoretical intensities respectively and c normalises the relative intensities of the two. B_n is an approximate way of accounting for the remaining inelastic scattering which still forms a background of noise on the image. It is assumed to be a constant value for each disc since the background is a slowly decaying function of scattering angle [28], n connects all the symmetry related discs which have the same background. If Poisson statistics are assumed for the collection system σ_i^2 can be replaced by I_{ex}^i. For a perfect fit with Poisson noise the error in χ^2 will be 1 due to the scaling of equation (3.3) to $1/N_{data}$. A quasi-Newton minimisation routine is used to fit the theoretical pattern and therefore obtain the bulk structure factor values.

One of the important differences between this method and the systematic row approach is that this method has a large time penalty attached. This is due not only to the increased number of discs but also the much larger number of points in each disc, typically 150 - 200 [8], and the larger beam set required for convergence of the pattern. This can easily require diagonalisation of a 350 beam set for each point (see section 3.5). The perturbation theory used in the systematic row method is now an essential part of the zone axis technique, required to give answers in a reasonable time span.

The two methods discussed here use very similar principles but the zone axis technique should be more sensitive due to the greater amount of dynamical diffraction undergone by the electron wave. It is also able to determine a larger number of structure factors in one analysis. However, this requires considerably more computer power since a larger number of diffraction amplitudes must be calculated. The rest of this chapter will deal with the zone axis technique and in particular how to optimise the analysis so that the calculation time is reduced to a minimum.

3.3 Experimental Considerations with the Zone Axis Technique

There are a number of practical points concerning implementation of this technique that need to be addressed.

3.3.1 Issues Concerning Structure Factor Refinement

The theory described in chapter 2 used only the zero layer contributions to $U(\mathbf{r})$ i.e. the projection approximation was made. Therefore, all HOLZ effects were ignored. If the theoretical calculation of the pattern is to use this same approximation it is essential that the zone axis chosen does not give rise to large amounts of HOLZ reflections.

For testing purposes it was decided to concentrate on the Si crystal since there are accurate X-ray analysis results available to compare against. Certain reflections in the Si, diamond, (as well as bcc and fcc) lattice are not allowed due to symmetry [21]. For the diamond structure of Si if the [110] axis is chosen then the FOLZ reflections are forbidden since in the diamond and fcc structure h,k and l must be all odd or all even. Therefore, HOLZ effects are likely to be much

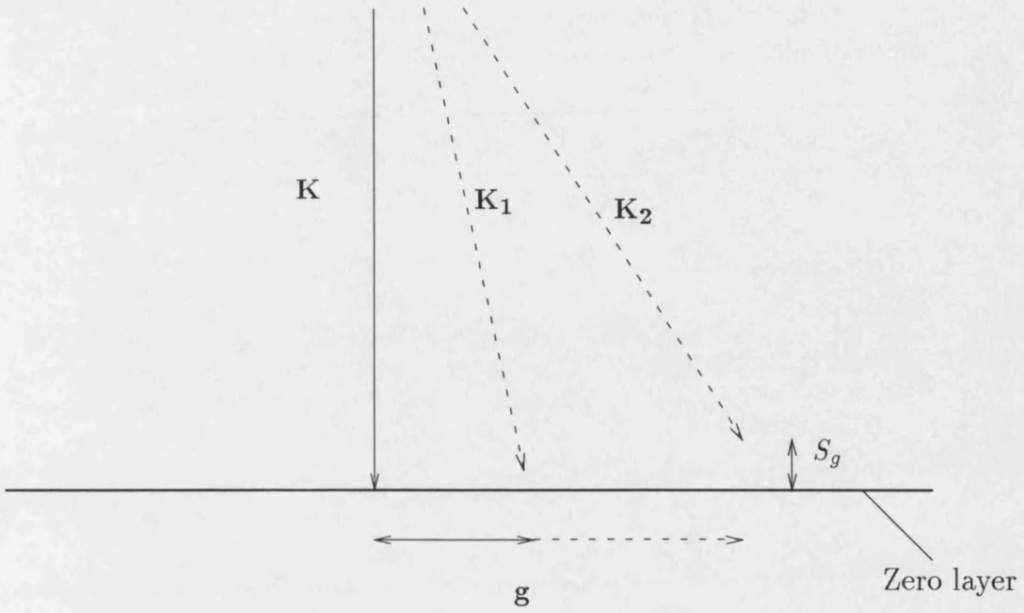

Figure 3.4: As **g** gets larger so the excitation error $S_{\mathbf{g}}$ gets larger and the intensity in the CBED disc gets smaller.

less important than for a zone axis where the FOLZ is allowed.

The next point which must considered is which discs in the zone axis pattern to use and the related question of which structure factors can be determined using a given zone axis pattern. Experimental conditions make it inevitable that any zone axis pattern will have noise due to the collection system and small energy loss inelastic scattering. At the same time the intensity of the CBED discs will tend to decrease as they get further away from the centre of the pattern due to the excitation error i.e. the Ewald sphere is further from the diffraction point, see figure 3.3.1, with the excitation error being given by, $S_{\mathbf{g}} \sim \frac{1}{2k}(-2\mathbf{K}.\mathbf{g} - g^2)$.

Therefore, some point will be reached where the signal to noise ratio will be too low for the signal to be useful. For the Si [110] zone axis this has been found to occur after including the first nine discs, i.e. the bright field disc and the {111}, {002} and {220} discs [28]. Additionally, the {220} discs have been found to contain relatively little information and have tended to be omitted, leaving a total of seven discs from which to extract the data and compare to theoretical

calculations.

As mentioned earlier not all structure factors are sensitive to this method of measurement and we must decide, given the discs we have chosen, which structure factors should be included as variable parameters and which should be left as constants. This is an important choice since if we do not include structure factors to which the pattern is sensitive other structure factors may be forced to compensate, leading to errors in the final bulk structure factor values. On the other hand including structure factors to which the patterns are not sensitive will lead to unnecessary calculation time and possible instabilities in the fit due to local minimums being found rather than the global minimum.

It has been found that the fitting procedure is most sensitive to structure factors which have associated discs in the CBED pattern being considered. Therefore, these structure factors should be included as variable parameters. However, it is also worth including structure factors which link the discs in the pattern as there should be some sensitivity to these. Therefore, the typical structure factors to be varied in a seven disc Si [110] pattern are the real and imaginary parts (to include absorption) of U_{111}, U_{220}, U_{113}, U_{222} and U_{004}. All other structure factors are left fixed at the neutral atom values.

Although we are using this technique to measure the structure factors shown above there are a number of other parameters which must be included into the fit since they alter the intensity and details of the theoretical pattern. These are the effective thickness and microscope voltage, $t/2k$, Debye-Waller factor [43], normalisation coefficient, c, and the background intensities, B_n. For the pattern matching technique to work a good initial guess must be made for each of the variable parameters so that the global minimum is found rather than a local minimum.

The structure factors can be started at the independent atom values and the background intensities can be estimated using values between the discs. However,

the starting point for the thickness (or t/2k) and normalisation coefficient is more complicated. For the thickness value a scanning method is used where the theoretical pattern is calculated for a range of thicknesses using the independent atom values and the χ^2 error of equation (3.3) is calculated using the experimental pattern. There is generally a dominant minimum when the value of χ^2 is plotted against $t/2k$ and this value should be taken as the initial guess of $t/2k$. The normalisation coefficient is then calculated using equation (3.2) at the value of the initial guess of $t/2k$ [28].

3.3.2 Measurement Issues

Before considering the details of the minimisation routine there are a number of experimental points to be considered. It was explained in section 3.2 that the intensities were extracted on a grid of points across the whole disc since the sensitivity to the structure factors showed no significant bias towards particular areas. The number of data points on the grid is to some extent arbitrary, however, it should be remembered that having too few will make the procedure ineffective and too many will cause the time taken for a calculation to become very large. A typical size for the grid is 13×13 pixels per disc [8]. It is very important that the grid points at which the intensities are measured are the same points at which the theoretical intensities are calculated. An accurate grid extraction process has been developed by Burgess and is detailed in [28].

The introduction of the CCD detector (section 3.2) makes quantitative electron diffraction easier but also introduces problems. The number of pixels covering the area of the CBED pattern is less than with photographic film, therefore, the measured points are unlikely to correspond exactly to the grid extraction points mentioned above. To over come this the intensity of the required orientation is found using a bilinear interpolation algorithm. Here, the intensities of the surrounding pixels are used to determine the value of the required point.

CCD cameras also suffer from damping of high spatial frequencies characterised by the point spread function of a particular camera and when this is combined with the low resolution due to a limited number of pixels severe distortions can be introduced [44]. This problem can be overcome using standard deconvolution algorithms [45] if the point spread function of the camera is known [46]. Although the use of the CCD detector introduces these new problems the advantages have ensured that the use of the CCD has become almost universal in quantitative CBED.

Additionally, if a Gatan imaging filter is used, as in section 3.6, where the data is collected in parallel, it is no longer acceptable to assume Poisson statistics for the sum of squares error of equation (3.3) and the variance σ^2 must be measured. Saunders et al [47] have detailed a method of achieving this where a set of white noise images are taken which cover the whole intensity range of the CCD and the standard deviation is plotted against the mean for the set of images. Various functions of the form $\sigma = mean^n$ are tried until some value of n is found which gives the best fit. The variance is then taken to be I^n_{theory}, for Poisson statistics n will be 0.5 which is assumed for the tests below.

3.4 Theoretical Calculation of CBED Patterns

In the last chapter the theory of elastically scattered electrons was explained, allowing us to make a theoretical calculation of a CBED pattern. In this chapter we have seen how to obtain an accurate elastic pattern and how to find the χ^2 difference between these patterns. We now consider how to minimise the differences between these two patterns and keep the total calculation time to a minimum.

3.4.1 Minimisation

As explained earlier the fitting method employed here minimises the differences between the two patterns (measured using χ^2) by allowing a set of fitting parameters to vary, principally the low order structure factors $U_{\mathbf{g}}$ but including thickness, normalisation coefficient and the background intensities. The quasi-Newton minimisation routine was chosen as a highly efficient method of minimising χ^2 [48, 49]. In this method the minimisation is achieved not merely by calculating the sum of squares function but also its gradient with respect to each varying parameter. If the gradients can be calculated quickly then this method offers substantial time savings over other minimisation methods which do not require the gradients [40] such as the simplex method used in the systematic row approach 3.2.1. However, in the zone axis approach it is a difficult task to obtain the gradients.

3.4.2 Gradient Calculation

The gradient of χ^2 with respect to each of the varied fitting parameters is given by,

$$\frac{\partial \chi^2}{\partial P} = \frac{1}{N_{data}} \sum_i \frac{\partial}{\partial P} (I^i_{ex} - cI^i_{th} - B_n)^2 / \sigma_i^2. \tag{3.4}$$

Here P is the parameter being varied and σ_i^2 is the variance of the ith point. The other symbols have the same meaning as previously.

Although the analytic gradients are relatively simple to find for the background, thickness and normalisation coefficient [28] it is a more difficult problem to find the analytic gradients for parameters of which the theoretical intensity is a function, i.e. the structure factors.

It is possible to find these gradients numerically by altering each parameter in

turn by a small amount and recalculating the pattern. However, the time taken for this method scales as N^3M where N is the size of the many-beam matrix and M is the number of parameters being varied. This is a very time consuming method when a large number of parameters need to be varied which is the case for zone axis fitting.

To overcome this time problem an expression for the analytic gradients was found by Bird and Saunders [8, 28] where, for the non absorptive case,

$$\begin{aligned}\frac{\delta A_{\mathbf{G}}}{\delta U_{\mathbf{H}}} &= -i\sum_{jj'}\left(\frac{\Sigma_{\mathbf{G}}\, C^{j}_{\mathbf{G}} C^{j'*}_{\mathbf{H+G}} t}{2k}\right) C^{j*}_{\mathbf{0}} C^{j*}_{\mathbf{G}} \\ &\times \left[-i(s^j + s^{j'})t/4k\right]\left[\frac{\sin((s^j - s^{j'})t/4k)}{(s^j - s^{j'})t/4k}\right]. \end{aligned} \tag{3.5}$$

When a Fast Fourier Transform method was used [28] it was found that the new method scaled as $N^3 \log N$. Thus for a sufficient number of parameters the use of analytic gradients will give a considerable time saving over the numeric case.

3.4.3 Calculation Time of a CBED Pattern

Although the gradient expressions described above can efficiently calculate the required gradients for minimisation the question of calculation time for a theoretical CBED pattern has not been fully addressed. As was stated in chapter 2 the many-beam matrix, which must be solved before the diffracted wave amplitude of equation (2.31) (and therefore intensity) can be found, is infinite and must be truncated at some point.

Where to choose this cut off point depends upon two conflicting demands. First, the many-beam matrix must be large enough to ensure that the theoretical pattern is fully converged, i.e. the introduction of additional beams should not change the pattern significantly. Otherwise, systematic errors will be introduced into the

pattern matching technique and the procedure cannot be expected to give valid results.

However, opposing the requirement for a large matrix is the need to keep calculation time to a reasonable level. To achieve this the matrix size must be kept to a minimum since the calculation time of the diffracted wave amplitude scales with the matrix order, N as N^3. To meet these conflicting demands Bird and Saunders [8] have reduced the size of the matrix to be diagonalised while including the additional beams needed for full convergence as a perturbation, as described below.

As a starting point let us consider the intensity of a point in one of the discs which is given by the modulus squared of the diffraction wave amplitude of equation (2.28),

$$I = |A_{\mathbf{G}}(\mathbf{K}, t)|^2 = |\sum_j \hat{C}_{\mathbf{0}}^{(j)*} C_{\mathbf{G}}^{(j)} \exp(-is^{(j)}t/2k)|^2 \tag{3.6}$$

where the many-beam equations (2.25) are used to calculate the eigenvalues $s^j(\mathbf{K})$ and eigenvectors $C_{\mathbf{G}}^j(\mathbf{K})$. Here, $\mathbf{K}$ is the component of the incident electron wave vector which is perpendicular to the zone axis being studied, it is equivalent to $\mathbf{K_0}$ in chapter 2, the left hand eigenvector has been included to take absorption into account and $s^{(j)}$ is complex.

Before implementing any approximation techniques we must first find the number of beams which will give a fully converged pattern. Figure 3.5 shows the convergence of $GaAs$ [110] where the sum of squares error, χ^2, between a 483 beam calculation and various smaller calculations is plotted against the number of beams in the smaller calculations. The intensities from the 483 beam calculation have been set so that the maximum intensity is given a value of 4000 simulating experimental data where the maximum value is 4096 for a 12 bit CCD. χ^2 was then given by,

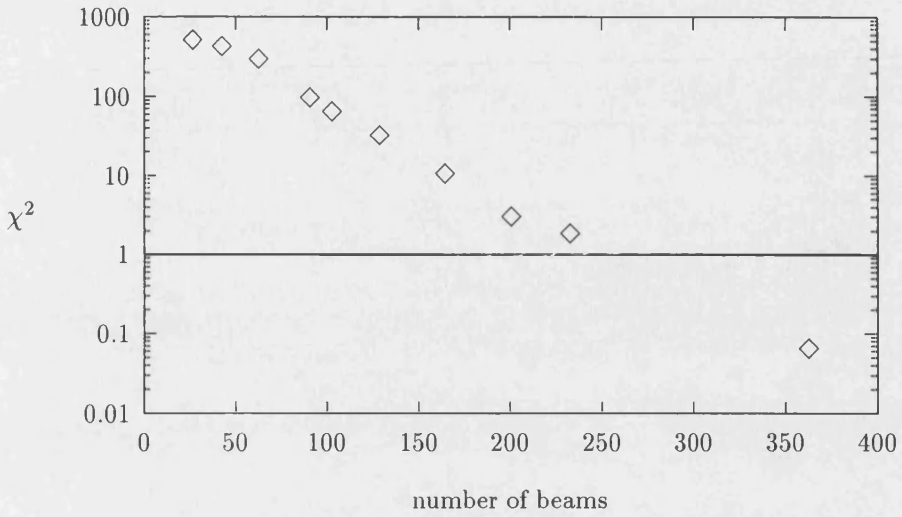

Figure 3.5: Graph of sum of squares error between 483 beam calculation and some smaller calculations against number of beams in smaller calculation. It can be seen that by ~ 370 beams the χ^2 is below 0.1.

$$\chi^2 = \frac{1}{N_{data}} \sum_i \frac{(I_{483}^{(i)} - cI_{sm}^{(i)})^2}{I_{483}^{(i)}}. \tag{3.7}$$

The sum i is over all 1183 data points (i.e. 169 orientations in 7 discs), c is a scaling factor as in equation (3.2), $I_{483}^{(i)}$ and $I_{sm}^{(i)}$ are the intensities of the 483 and smaller matrices at point i respectively and σ_i^2 has been replaced with $I_{483}^{(i)}$ since no experimental work is involved here allowing Poisson statistics to be assumed. It can be seen that by ~ 370 beams $\chi^2 \ll 1$ and the pattern is effectively converged at this point.

To be able to compare the theoretical and experimental intensities the theoretical pattern must be calculated at the same points as the experimental data was taken i.e. on a 13×13 grid giving a total of 169 orientations each of which requires a matrix diagonalisation. As several iterations are necessary before a best fit can be achieved calculation time becomes an important factor in the viability of this method. However, since the time taken for each diagonalisation scales as N^3 any reduction in the size of the matrix to be diagonalised will significantly reduce the

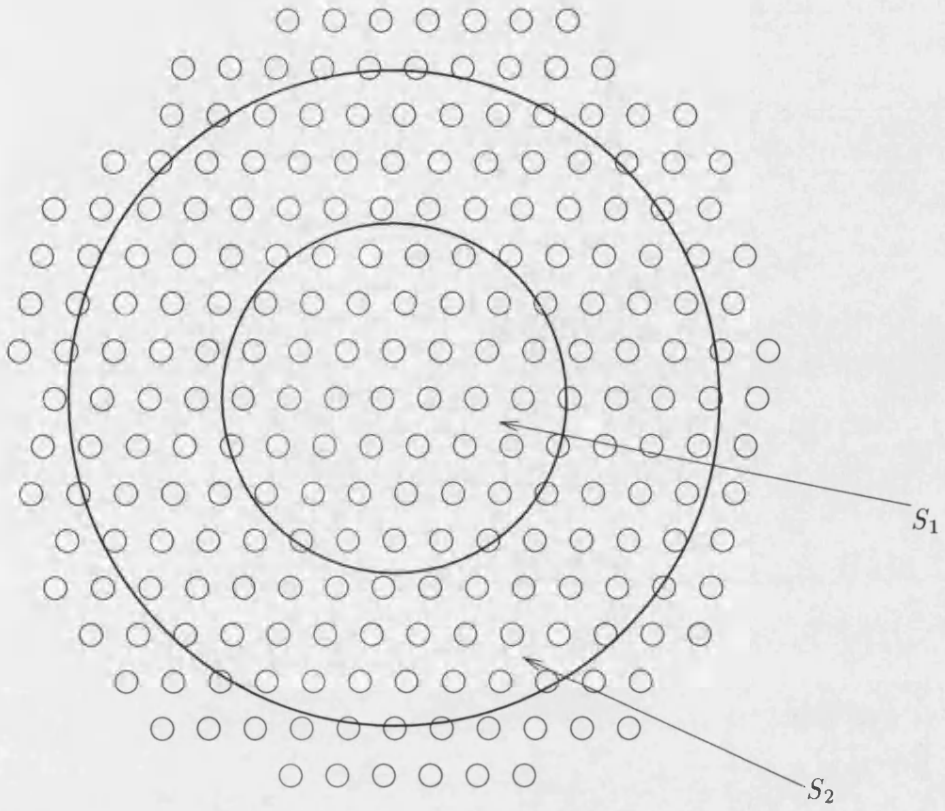

Figure 3.6: drawing of how the inner (S_1) and outer (S_2) beam sets are split. The outer beam set is assumed to be weak compared to the inner beams. The outer circle is assumed to be at the well converged limit.

computation time.

For a converged pattern some beams in the many beam matrix will be weak compared to the others and the matrix can be reduced to include only the relatively strong beams, the weaker ones being included as a perturbation. If the truncated many beam matrix includes S_c **G** vectors then perturbation theory will introduce two sub sets S_1 and S_2 where the matrix of size S_1 is calculated exactly by diagonalisation and contains all the strong beams while S_2 is included as a perturbation, see figure 3.6. In this case the sum in equation (3.6) is only over S_1 beams.

There are two methods of reducing the size of the matrix to be diagonalised which

we will consider here, second order perturbation theory originally used by Bird and Saunders [8] and the Bethe approximation originally used for the systematic row technique[6]. We will consider second order perturbation theory in the next section.

3.4.4 Second Order Perturbation Theory

If the total number of beams needed for a fully converged pattern can be split into two parts one with a strong contribution to the final intensities and the other with only a weak contribution then standard perturbation theory can be used to reduce the size of the many-beam matrix which must be diagonalised [50]. Thus if the full many-beam matrix is represented by,

$$H = \begin{pmatrix} a_{1,1} & a_{1,2} & \dots & a_{1,n} & a_{1,n+1} & \dots & a_{1,N} \\ \vdots & \vdots & \vdots & \vdots & \vdots & \vdots & \vdots \\ a_{n,1} & \dots & \dots & a_{n,n} & a_{n,n+1} & \dots & a_{n,N} \\ a_{n+1,1} & \dots & \dots & a_{n+1,n} & a_{n+1,n+1} & \dots & a_{n+1,N} \\ \vdots & \vdots & \vdots & \vdots & \vdots & \ddots & \vdots \\ a_{N,1} & \dots & \dots & a_{N,n} & a_{N,n+1} & \dots & a_{N,N} \end{pmatrix} \tag{3.8}$$

then it can be split into two sub matrices H^0, for the main contributions, and V acting as a perturbation on H^0. These matrices will be given by,

$$H^0 = \begin{pmatrix} a_{1,1} & a_{1,2} & \dots & a_{1,n} & 0 & 0 & \dots & 0 \\ \vdots & \vdots & \vdots & \vdots & \vdots & \vdots & \vdots & \vdots \\ a_{n,1} & \dots & \dots & a_{n,n} & 0 & 0 & \dots & 0 \\ 0 & \dots & \dots & 0 & a_{n+1,n+1} & 0 & \dots & 0 \\ \vdots & \vdots & \vdots & \vdots & 0 & \ddots & \vdots & \vdots \\ \vdots & \vdots & \vdots & \vdots & \vdots & \vdots & \ddots & \vdots \\ 0 & \dots & \dots & 0 & 0 & \dots & 0 & a_{N,N} \end{pmatrix}$$

$$V = \begin{pmatrix} 0 & \dots & \dots & 0 & a_{1,n+1} & a_{1,n+2} & \dots & a_{1,N} \\ \vdots & \vdots & \vdots & \vdots & \vdots & \vdots & \vdots & \vdots \\ 0 & \dots & \dots & 0 & a_{n,n+1} & a_{n,n+2} & \dots & a_{n,N} \\ a_{n+1,1} & \dots & \dots & a_{n+1,n} & 0 & 0 & \dots & 0 \\ \vdots & \vdots & \vdots & \vdots & \vdots & \vdots & \ddots & \vdots \\ a_{N,1} & \dots & \dots & a_{N,n+1} & 0 & 0 & \dots & 0 \end{pmatrix}.$$

V contains all zeros in the bottom righthand corner (from $a_{n+1,n+1}$) since it is only by assuming this that either perturbation theory or the Bethe approximation can be used. However, for the case where the outer beam set is weak compared to the inner beam set these values will be small and can be approximated to zero since they correspond to diffraction from one weak beam into another. The H^0 matrix is diagonalised and perturbation theory gives the corrected values for the eigenvalues and eigenvectors, to the second order, according to the formulae below [50],

$$s^j = s_0^j + \langle j|V|j\rangle + \sum_{i \neq j} \frac{\langle j|V|i\rangle^2}{s_0^j - s_0^i} + \dots \tag{3.9}$$

and

$$\psi_j = \psi_j^0 + \sum_{i \neq j} \psi_j^0 \frac{\langle i|V|j\rangle}{s_0^j - s_0^i} + \dots . \tag{3.10}$$

Here, s_0 is the eigenvalue and ψ^0 is the eigenfunction obtained by diagonalising the matrix of size S_1, j is the sum over all inner states and i is the sum over all outer states, where the outer states are those which are considered to be small compared to the inner states, i.e. those which lie between the first and second circle in figure 3.6. The first order term in equation (3.9) i.e. $\langle j|V|j\rangle$ will be identically zero since the V matrix contains only zero valued elements out to $a_{n,n}$ (where $n \equiv S_1$) and j only ranges over these elements. Therefore, the second order term must be used to perturb the eigenvalues. s^j is now given by,

$$s^j = s_0^j + \sum_{i \neq j} \frac{\langle j|V|i\rangle^2}{s_0^j - s_0^i}. \tag{3.11}$$

Originally Bird and Saunders proposed using second order perturbation on the eigenvalues alone since changing the eigenvectors involved considerably more calculation and it was thought that the eigenvalues would be the most significant in accurate determination of A_G. Changing the value of the eigenvectors also means that the analytic gradients developed by Bird and Saunders would no longer be correct whereas changing the eigenvalues leaves the gradient expressions exact.

3.4.5 Bethe Approximation

As an alternative method the Bethe approximation [51, 6] can be used where rather than diagonalising the sub matrix H^0 first and later altering the basic values of s_0, the H^0 matrix is altered to include the additional S_2 beams before diagonalisation. This was proposed as a method of reducing the size of the calculation for the systematic row approach in Spence and Zuo [6] and has been shown to be effective in a number of papers [52, 53]. This approximation has the advantage that the eigenvectors are also altered from their S_1 value without the need to perform additional calculations.

To show how this is done we start by noting that the matrix H given in equation (3.8) satisfies,

$$(H - Is)\Psi = 0 \tag{3.12}$$

where I is the identity matrix, Ψ is the eigenvector matrix and s are the eigenvalues. If we now split H into it's component parts as in the last section and write the matrix equation in terms of explicit sums we obtain,

$$\sum_i \sum_j (H^0_{ij} - s\delta_{ij} + V_{ij})C_j = 0 \tag{3.13}$$

where i, j sum over all beams, S_c. If we now consider i only over the second subset

of S_c i.e. over S_2 and make the same approximation as second order perturbation theory that $V_{ij} = 0$ when both i and j are in S_2 we find that,

$$C_i = -\sum_{j \neq i} \frac{V_{ij} C_j}{H^0_{ii} - s}. \tag{3.14}$$

In this case the sum over j need only contain the S_1 terms since $V_{ij} = 0$ otherwise. Let us now consider i over the first subset of S_c i.e. over S_1; writing equation (3.12) as separate sums over S_1 and S_2 gives,

$$\sum_i \sum_j (H^0_{ij} - s\delta_{ij}) C_j + \sum_k V_{ik} C_k = 0 \tag{3.15}$$

where the sums i, j are over S_1 and k is over S_2, then we can use equation (3.14) to replace C_k if we assume that $H^0_{ii} \gg s$. This gives,

$$\sum_i \sum_j (H^0_{ij} - s\delta_{ij}) C_j + \sum_k V_{ik} (-\sum_l \frac{V_{kl} C_l}{H^0_{kk}}) = 0. \tag{3.16}$$

The sum l is over S_1 as in equation (3.14) and can therefore be included in the sum over j, simplifying the equation to,

$$\sum_i \sum_j (H^0_{ij} - s\delta_{ij}) C_j + \sum_k \frac{V_{ik} V_{kj}}{H^0_{kk}} C_j = 0. \tag{3.17}$$

This equation defines a matrix which must be diagonalised to solve for the eigenvalues and eigenvectors, this matrix is defined by,

$$M_{ij} = H^0_{ij} - \sum_k \frac{V_{ik} V_{kj}}{H^0_{kk}} \tag{3.18}$$

or writing this in terms of the many-beam matrix gives,

$$M_{\mathbf{G},\mathbf{G}'} = H^0_{\mathbf{G},\mathbf{G}'} - \sum_{\mathbf{H}} \frac{U_{\mathbf{G}-\mathbf{H}} U_{\mathbf{H}-\mathbf{G}'}}{(\mathbf{K}+\mathbf{H})^2} \tag{3.19}$$

where H^0 is the matrix of size S_1 and the sum $\mathbf{H}$ is over the outer set of $\mathbf{G}$ vectors S_2. $M_{\mathbf{G},\mathbf{G}'}$ is now diagonalised and gives corrected values for both the eigenvalues and eigenvectors in a single operation.

It may be that this method will reduce the calculation time for a structure factor refinement since both eigenvalues and eigenvectors are altered, requiring fewer beams to be used to produce the same χ^2 error. However, there are a number of issues concerning the implementation of the method with the zone axis technique which must be considered. The next section will deal with these issues in depth.

3.5 Evaluation of Perturbation Methods

The Bethe approximation has been shown to work for the systematic row pattern matching technique and the inclusion of corrected eigenvectors as well as eigenvalues implies more accurate/faster pattern matching if used in the zone axis technique. However, it is essential that the approximation is fully evaluated before including it into the structure factor refinement code. We must insure that the gradient expression, which is no longer exact due to the additional $C_{\mathbf{G},\mathbf{G}'}$ terms introduced via equation (3.17), does not cause problems. It is important to avoid introducing additional errors and verify the decrease in calculation time.

We will first consider a simple three beam case so that we can see exactly how each method operates, where they begin to break down and give an indication of how accurate each method is. Next, a more realistic system is used to assess how many beams each method needs and therefore how long each method will take. This same system is then used to investigate the accuracy of the analytic gradients.

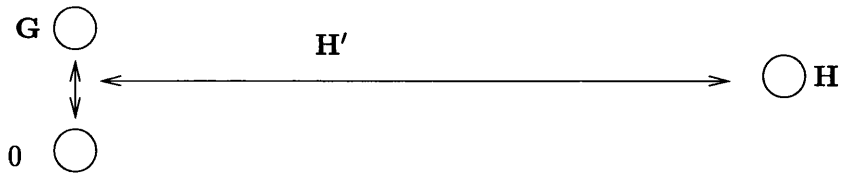

Figure 3.7: Geometry of the 3 beam example. k is going into the page with **K** always along $(0, \mathbf{G})$ ensuring the diffraction into **H** is always weak.

Finally, the Bethe approximation will be used in a full fitting calculation where the experimental results are first substituted by a full pattern calculation and the initial starting values of the structure factors are altered by 1-2%. In section 3.6 genuine experimental results are used and the full fitting method with the new Bethe approximation is used to determine accurate low order structure factors for the Si[110] system.

3.5.1 Three Beam Comparisons

Consider a three beam calculation as shown in fig 3.7 where the first two beams are strong and the third is weak. In this example we will assume for simplicity that there is no absorption. The incident wave vector, **k**, goes into the page and we will choose its transverse component **K** to always go along (**0**,**G**), ensuring that the diffraction into **H** is always weak. Using the many-beam equations of the last chapter we get the many-beam matrix,

$$\begin{pmatrix} (\mathbf{K}+\mathbf{0})^2 - s^j & U_{\mathbf{0-G}} & U_{\mathbf{0-H}} \\ U_{\mathbf{G-0}} & (\mathbf{K}+\mathbf{G})^2 - s^j & U_{\mathbf{G-H}} \\ U_{\mathbf{H-0}} & U_{\mathbf{H-G}} & (\mathbf{K}+\mathbf{H})^2 - s^j \end{pmatrix}. \tag{3.20}$$

Here U are the structure factors, $U_{\mathbf{0-G}}$ and $U_{\mathbf{G-0}}$ are equal if the potential is real which we assume here, for simplicity we will replace these by U_1. $U_{\mathbf{0-H}}$ and $U_{\mathbf{G-H}}$ and their conjugates can be replaced by U_2 since the geometry chosen makes them the same. For the conditions shown in figure (3.7) U_1 will be large

and U_2 will be small so that the above matrix can be split into two parts H^0 and V as in section 3.4.3 where V is a perturbation on H^0. To simplify the calculations we define $\mathbf{K}$ as $-\mathbf{G}/2 + \delta\mathbf{K}$ i.e. for $\delta\mathbf{K} = 0$, $\mathbf{K}$ is half way between $\mathbf{0}$ and $\mathbf{G}$ and satisfies the Bragg condition for $\mathbf{G}$. Noting the following identities,

$$(\mathbf{K} + \mathbf{0})^2 = \frac{\mathbf{G}^2}{4} + \delta\mathbf{K}^2 - \mathbf{G}.\delta\mathbf{K}$$

and

$$(\mathbf{K} + \mathbf{G})^2 = \frac{\mathbf{G}^2}{4} + \delta\mathbf{K}^2 + \mathbf{G}.\delta\mathbf{K},$$

we see that the only difference between these equations is the sign of $\mathbf{G}.\delta\mathbf{K}$. Therefore, we can substitute a variable w into the many beam matrix (3.20) where $w = \mathbf{G}.\delta\mathbf{K}$ and a value of $w = 0$ will give the exact Bragg condition.

To further simplify the calculation $\mathbf{H}$ is chosen so that $\mathbf{H} = \mathbf{G}/2 + \mathbf{H}'$ where $\mathbf{H}'$ is perpendicular to both $\mathbf{K}$ and $\mathbf{G}$. This gives $(\mathbf{K} + \mathbf{H})^2$ as

$$(\mathbf{K} + \mathbf{H})^2 = \delta\mathbf{K}^2 + 2\mathbf{H}'.\delta\mathbf{K} + \mathbf{H}'^2.$$

However, $2\mathbf{H}'.\delta\mathbf{K} = 0$ as $\delta\mathbf{K}$ is perpendicular to $\mathbf{H}$. A second substitution can be made by subtracting $\frac{\mathbf{G}^2}{4}$ from each of the diagonal elements and defining $\beta = \delta\mathbf{K}^2 + \mathbf{H}'^2 - \frac{\mathbf{G}^2}{4}$ The three beam case described above can now be written as,

$$\begin{pmatrix} w - s^j & U_1 & U_2 \\ U_1 & -w - s^j & U_2 \\ U_2 & U_2 & \beta - s^j \end{pmatrix} \tag{3.21}$$

where we are assuming that $\beta \gg w$ and $U_1 \gg U_2$. Splitting this into two separate parts as described earlier gives,

$$H^0 = \begin{pmatrix} w - s^j & U_1 & 0 \\ U_1 & -w - s^j & 0 \\ 0 & 0 & \beta - s^j \end{pmatrix} \tag{3.22}$$

$$V = \begin{pmatrix} 0 & 0 & U_2 \\ 0 & 0 & U_2 \\ U_2 & U_2 & 0 \end{pmatrix}. \tag{3.23}$$

If the second order perturbation theory of equation (3.9) i.e.,

$$s^j = s_0^j + \sum_{i \neq j} \frac{\langle j|V|i\rangle^2}{s_0^j - s_0^i} \tag{3.24}$$

is applied to the eigenvalues of the diagonalised H^0 matrix then the eigenvalues are given by,

$$s^1 = (w^2 + U_1^2)^{1/2} + \frac{U_2^2(w^2 + U_1^2)^{1/2} + U_1 U_2^2}{w^2 + U_1^2 - \beta(w^2 + U_1^2)^{1/2}}$$

and

$$s^2 = -(w^2 + U_1^2)^{1/2} + \frac{U_2^2(w^2 + U_1^2)^{1/2} - U_1 U_2^2}{w^2 + U_1^2 - \beta(w^2 + U_1^2)^{1/2}}. \tag{3.25}$$

In order not to complicate the analysis these expressions are derived in appendix A. These now represent the three beam altered eigenvalues that are used to calculate $A_{\mathbf{G}}(\mathbf{K}, t)$ in the original zone axis pattern matching technique of Bird and Saunders.

If we now turn our attention to the Bethe approximation the H^0 matrix above is altered using the expression previously derived,

$$M_{\mathbf{G},\mathbf{G}'} = H^0_{\mathbf{G},\mathbf{G}} - \sum_{\mathbf{H}} \frac{U_{\mathbf{G}-\mathbf{H}} U_{\mathbf{H}-\mathbf{G}'}}{(\mathbf{K} + \mathbf{H})^2}. \tag{3.26}$$

Here $H^0_{\mathbf{G},\mathbf{G}}$ is the H^0 matrix in equation (3.22), the sum over $\mathbf{H}$ which includes only the outer, S_2, beam set leads to only the U_2 terms being added to the refined matrix and $M_{\mathbf{G},\mathbf{G}'}$ is the altered matrix which has to be diagonalised. $M_{\mathbf{G},\mathbf{G}'}$ is given by,

$$M_{\mathbf{G},\mathbf{G}'} = \begin{pmatrix} w - (U_2^2/\beta) - s^j & U_1 - U_2^2/\beta \\ U_1 - U_2^2/\beta & -w - (U_2^2/\beta) - s^j \end{pmatrix}. \tag{3.27}$$

We can easily write down an expression for the eigenvalues from this matrix, these are given below,

$$s^j = -\frac{U_2^2}{\beta} \pm \frac{1}{2}\left(\frac{4U_2^2}{\beta} - 4(\frac{2U_1U_2}{\beta}) - w^2 - U_1^2\right)^{\frac{1}{2}} \tag{3.28}$$

At first sight there are very few similarities with the second order expression. However, if we expand the expression to the second order we find that the expressions are very similar. This has been done in appendix A and the results are shown below,

$$s^j = (w^2 + U_1^2)^{1/2} + \frac{U_2^2(w^2 + U_1^2)^{1/2} + U_1U_2^2}{-\beta(w^2 + U_1^2)^{1/2}} + \ldots \tag{3.29}$$

and

$$s^j = -(w^2 + U_1^2)^{1/2} + \frac{U_2^2(w^2 + U_1^2)^{1/2} - U_1U_2^2}{-\beta(w^2 + U_1^2)^{1/2}} + \ldots . \tag{3.30}$$

It can be seen that the only difference in the expressions for the eigenvalues is the additional term $(w^2 + U_1^2)$ on the bottom of equation (3.25). However, the expression of equation 3.28 includes all the higher terms which are left out in second order perturbation theory. It should also be remembered that although the expression for the eigenvalues are very similar in both cases it is only in the Bethe case that the eigenvectors will be altered.

We are now in a position to compare the relative merits of the two approximations. To do this we first find the diffraction amplitudes $A_{\mathbf{G}}$ by diagonalising:-

- the full three beam case of equation (3.21)
- the basic 2×2 matrix of equation (3.22)
- the altered Bethe matrix of equation (3.27)
- applying the second order approximation of equation (3.9) to the eigenvalues from the basic 2×2 matrix.

There are a number of variables in the expression for the diffracted wave amplitude of equation 2.31 which need to be defined. $t/2k$ is set to unity, which is equivalent to a thin non absorbing crystal at normal microscope voltages (e.g. 500Å crystal at 200keV). U_1 is set to 1 for simplicity with the product of U_2 and β also being set to 1. In the work here U_2 is set to either 0.1 or 0.25 with corresponding values of β, as the difference between these values decreases it is expected that the amplitudes produced using the approximations will become less accurate. Finally, w has been altered in a 'rocking curve' manner from -10 to +10, to include values where the assumption that $\beta \gg w$ is not valid.

Let us first consider a situation where $U_2 = 0.1$ and $\beta = 10$ i.e. the approximation that $\beta \gg U_2$ is a very good one. In all results shown here the intensity values have been normalised so that the maximum intensity value of the full 3×3 calculation is equal to 1. Fig 3.8 shows the differences between each of the three approximations and the exact solution i.e. the difference between I calculated using the full 3×3 matrix and:-

- the basic 2×2 matrix.
- the Bethe matrix
- second order perturbation theory

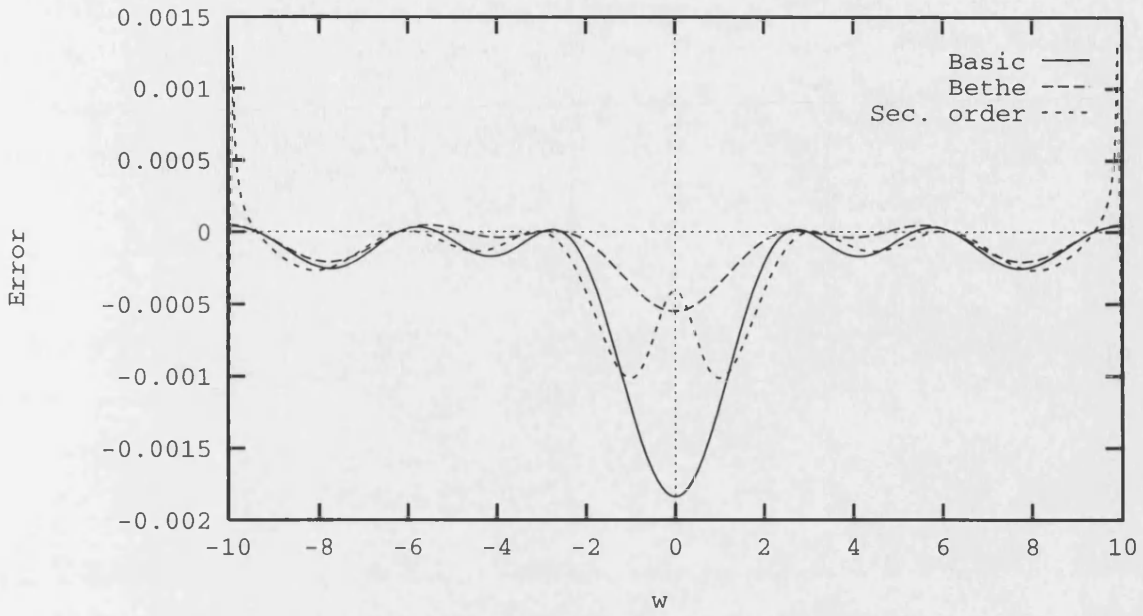

Figure 3.8: differences between the intensities of each approximation and the exact intensity for the three beam case. Here, $U_1 = 1, t/2k = 1, U_2 = 0.1, \beta = 10$.

At these values the approximations are good with $\beta \gg U_2$ and the errors being small. A Total of 100 points were calculated across the rocking curve, If the errors at each point are added together, the Bethe approximation gives an error of 0.048, second order perturbation theory of 0.104 and the basic 2×2 matrix of 0.123. It can be seen that even at these low levels of error the Bethe approximation is giving a better fit to the true 3×3 calculation than either of the other methods.

However, when U_2 is set to 0.25 and β to 4 as shown in figure 3.9 the normalised errors are much larger corresponding to a total error of 2.4 for the Bethe approximation, 3.55 for the second order perturbation theory and 3.45 for the simple 2×2 calculation respectively. Another important feature is shown more clearly in this example. In both figure 3.8 and 3.9 when w approaches β the errors increase dramatically for the second order perturbation case, giving a discontinuity in the line graph. If we consider equation (3.25) we can see that at $\beta = (w^2 + U_1^2)^{1/2}$ the eigenvalue will suffer from a division by zero. This is what is happening at $w = 4$ in figure 3.9 (and $w = 10$ in figure 3.8). In more conventional terms this corresponds to $(\mathbf{K} + \mathbf{G})^2 = (\mathbf{K} + \mathbf{H})^2$ i.e. the approximation that $\mathbf{H}$ is a long way

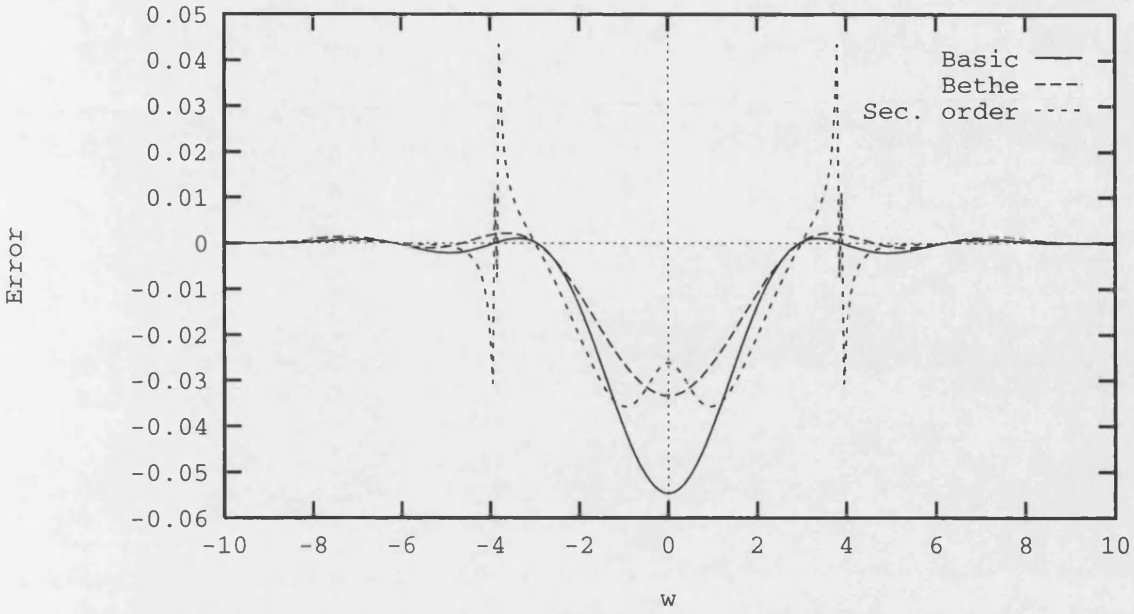

Figure 3.9: differences between the intensities of each approximation and the exact intensity for the three beam case. Here, $U_1 = 1, t/2k = 1, U_2 = 0.25, \beta = 4$.

from $\mathbf{0} - \mathbf{G}$ does not hold. This accounts for why the total errors in the second order perturbation theory look so large. In the last case where $\beta = 4$ if the cut off is made at $w = \pm 3.0$ i.e. before the approximation completely breaks down then the errors are, 2.17, 2.82 and 3.26 for the Bethe, second order and 2×2 approximations respectively.

In a realistic system the discontinuity in the above graphs is a problem since it is not possible to choose two beam sets S_1 and S_2 such that the beams in S_2 are small compared to all the beams in S_1. Bird and Saunders overcame this problem by creating a third beam set S_s say, which is a subset of S_1 but whose eigenvalues are not altered using equation (3.9). Figure 3.10 shows a schematic representation of these beams sets. However, the beam set S_s was difficult to choose and the criterion of which beams were included was to some extent subjective. However, it is clear from both the line graphs and equation (3.19) that the Bethe approximation does not suffer from this division by zero. Therefore, the Bethe approximation can be used on all beams in S_1 and no artificial cut off, which may result in a loss of accuracy, is necessary.

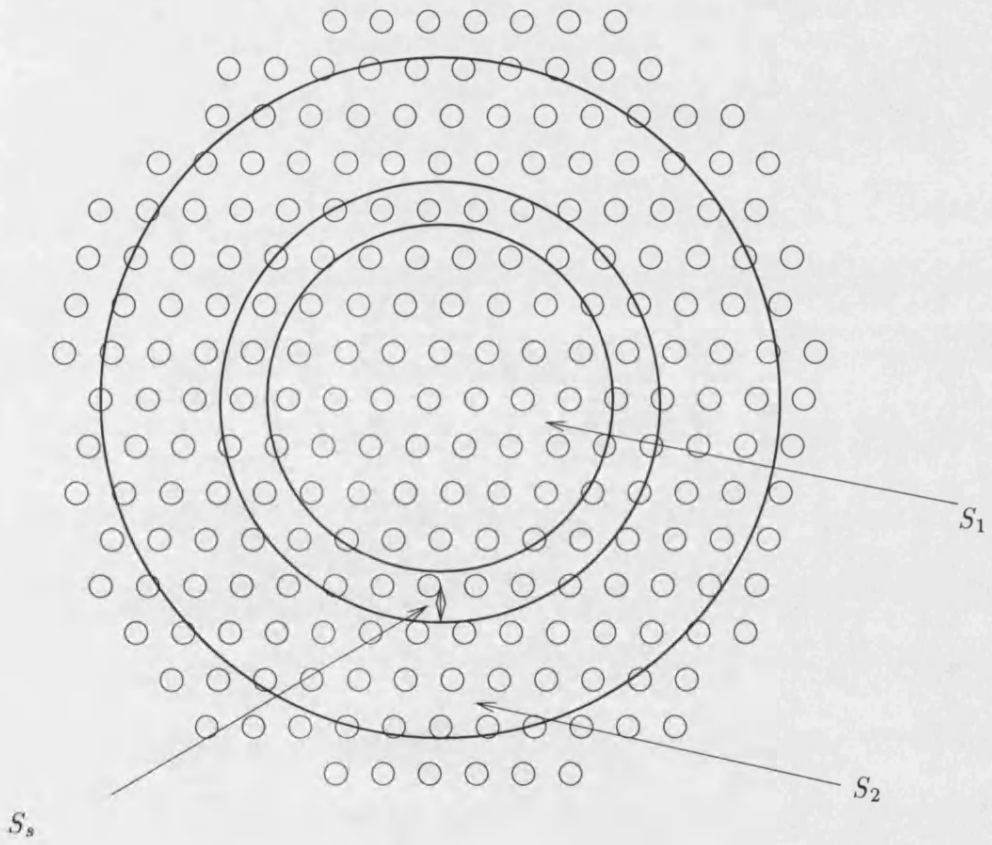

Figure 3.10: Schematic representation of the three beam sets necessary when using second order perturbation.

In this section we have used a simple 3 beam case to show how second order perturbation theory and the Bethe approximation can be applied to the many-beam equation to reduce the size of the matrix which needs to be diagonalised. The error in intensity for both approximations was shown to be of a similar order of magnitude but with the Bethe approximation giving smaller errors in each case. It was shown that the expressions for the corrected eigenvalues are similar for both approximations, although the Bethe approximation includes the higher order terms left out in second order perturbation theory. Additionally, the Bethe expression will not lead to a division by zero when the approximations are no longer valid. Hence, it was shown that there is no need for an artificial cut off to prevent this from happening. Therefore, the Bethe approximation may prove to be more accurate. However, the Bethe approximation is being implemented in order to save computing time and some evaluation of the relative speeds of the two approximations is necessary. This will be done on the next section.

3.5.2 Relative Speed of the Approximations

By far the most time consuming aspect of these calculations are the matrix diagonalisations, these scale as N^3 where, N is the order of the matrix. Therefore, if one method uses fewer beams in the diagonalisation routine to obtain the same level of convergence in the diffraction pattern then this will be the fastest method.

To find which method requires the fewest inner beams we must first obtain a CBED pattern against which to compare the approximation patterns. Although an experimental pattern could be used, a much fairer test is to calculate a fully converged CBED pattern where the matrix has been truncated to a finite size but the inner beam set S_1 equals the total number of beams S_c, i.e. $S_2 = 0$. Two systems have been chosen to test the approximations, the Si [110] and GaAs [110] axes with Debye Waller factors of 0.26 for Si, 0.2516 for Ga and 0.2657 for As [12]. The $(000), (00\bar{2}), (\bar{1}11), (\bar{1}1\bar{1}), (1\bar{1}\bar{1}), (1\bar{1}1)$ and (002) discs were used. The accelerating voltage was set to 200keV and the thickness parameter $t/2k$ was set

at 6.25 which is equivalent of a crystal thickness of $\sim$ 3000 Å which is typical of experimental thicknesses, see section 3.6. The structure factors were assumed to be the independent atom values of Doyle and Turner with no absorption included. For this calculation S_c was set to 400 since tests show that at this level the patterns are well converged (see section 3.4.3). This 'exact' calculation was then used as the benchmark against which the approximations could be tested.

The next step was to keep the total number of beams S_c constant at the fully converged limit and reduce the number of inner beams to be diagonalised, i.e. reduce the size of S_1 and increase S_2. The intensity pattern was recalculated using the new values of S_1 and S_2. These new intensity values were then compared with the previously calculated fully converged set of points. The comparison is made using a sum of squares difference χ^2 between the 'exact', I_{exact}, and the approximate, I_{approx}, intensities and is similar to that of equation (3.3) with

$$\chi^2 = \frac{1}{N_{data}} \sum_{i=1}^{N_{data}} \frac{(I_{exact}^{(i)} - cI_{approx}^{(i)})^2}{I_{exact}^{(i)}}. \tag{3.31}$$

In order to mimic the real zone axis fitting procedure, where a 12 bit CCD detector is commonly used to record the CBED pattern, the exact intensities are scaled to a maximum of 4096 with each intensity being stored as an integer. To avoid $I_{exact}^{(i)}$ on the bottom of equation (3.31) causing the equation to blow up any exact intensity of zero is changed to one. N_{data} is the total number of data points and consists of a 13 $\times$ 13 grid on each of the 7 discs, i.e. 1183 pieces of data as in the typical experimental set up. c is the scaling factor whose optimum value is given by,

$$c = \frac{\sum_i I_{approx}^{(i)}}{\sum_i I_{approx}^{(i)2}/I_{exact}^{(i)}}. \tag{3.32}$$

Plots of χ^2 against the size of S_1 are shown in figures 3.11 and 3.12 for Si[110] and GaAs[110] respectively. For comparison the worst case limit is shown where no adjustment is made to the values obtained by diagonalising the inner matrix i.e. S_c is reduced to the value of S_1.

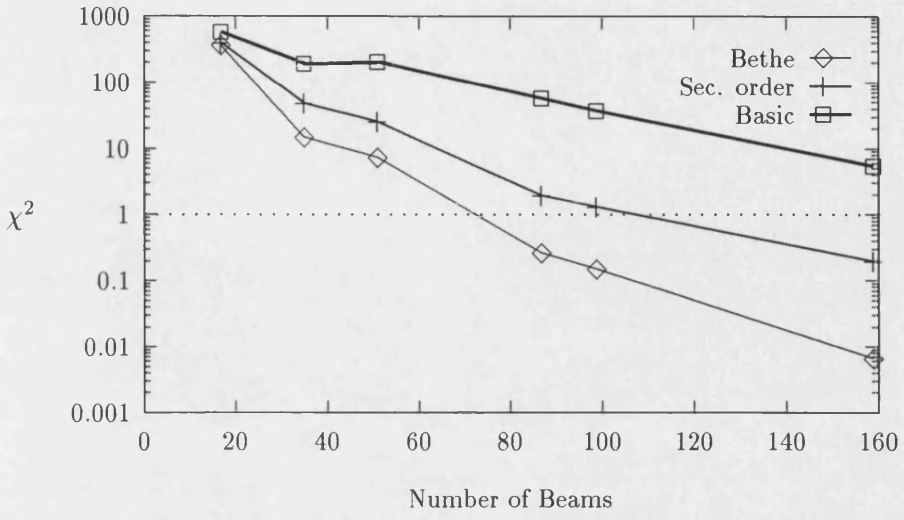

Figure 3.11: Sum of squares error plotted against the number of beams being diagonalised for Si[110], for the Bethe approximation, Second order approximation and S_c reduced to S_1.

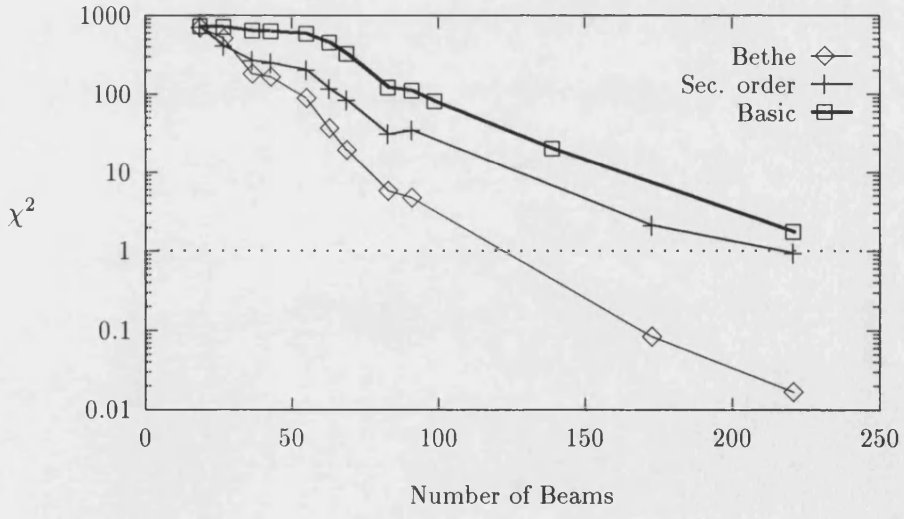

Figure 3.12: Sum of squares error plotted against the number of beams being diagonalised for GaAs[110].

The smallest possible value of χ^2 obtainable in a fit between theory and experiment is 1. Therefore, any fit between theory and experiment requires that the χ^2 error between the theoretical exact intensities and the truncated approximate solutions is much less than 1 to avoid systematic errors. It has been assumed in the work presented here that a χ^2 value of 0.1 will be adequate to prevent systematic errors. It can be seen in figures 3.11 and 3.12 that the Bethe approximation achieves this in $\sim$ 140 beams for Si and 160 for GaAs where as second order perturbation theory requires many more beams. Therefore, for a single pattern the Bethe approximation converges using fewer beams and will be a faster computational method.

3.5.3 Inexact Gradient Evaluation

Although it has been shown that the Bethe approximation achieves converged CBED patterns in fewer beams than second order perturbation theory this is not the only issue which must be addressed when considering the pattern matching technique. In order for the method to find the values of the structure factors it must find the gradients for the sum of squares error, χ^2, with respect to each of the varied parameters efficiently. The analytic gradient expressions of equation (3.5) only apply to the exact calculation, however, the expressions have been adapted for use with second order perturbation theory by Bird and Saunders [8, 28] but their use with the Bethe approximation has not previously been tested.

The essential difference between using the exact calculation and the Bethe approximation is that in the exact case each $U_{\mathbf{G}}$ only occurs in a limited number of off-diagonal matrix elements. Whereas for the Bethe approximation it occurs in many of the elements of $M_{\mathbf{G}-\mathbf{G}'}$ through the second term on the right hand side of equation (3.19). It may be that it is possible to use the same gradient expressions used for the second order case even though they are no longer exact. To understand why this may be true consider a matrix element where a low order structure factor we are trying to determine is included. The right hand side of

equation (3.19) only sums over the outer beam set S_2 i.e. **H** is large. The matrix element in equation (3.19) must be in the inner beam set S_1 by definition. Now, for the low order structure factor being considered to be in the expression for the matrix element **G** or **G'** must be very close to **H** i.e. it too must be large. Therefore, it seems reasonable that large diffraction away from the incident direction and back is unlikely and the overall matrix element will be small. Therefore, changes in the low order structure factor will not be significant for these matrix elements and the overall accuracy. However, it is important to measure the effect so we know if the gradient expressions can still be used.

To test this a pattern of $S_c = 345$ was calculated using the independent atom structure factors for the GaAs [110] system described above i.e. accelerating voltage of 200keV, $t/2k$ of 6.25 and Debye Waller factors of 0.2516 and 0.2657 for Ga and As respectively. This was used as a reference 'experimental' or 'exact' pattern. 345 beams were used since it was important to use a similar number of beams as needed in a real calculation but complete convergence was not necessary for the tests and the calculations are quicker with this number of beams (rather than using the 483 beam calculation used to test for convergence). Next the real and imaginary parts of six structure factors were changed by 1-2% so that the gradients of χ^2 with respect to each structure factor would be significant. Finally, the pattern was recalculated with an inner beam set of $S_1 = 181$, which was shown to give good convergence in figure 3.12, and total beams $S_c = 345$ and the Bethe approximation was used to include the remaining S_2 beams.

The gradient expression of equation (3.4) was used to find the gradient due to each of the six structure factors. To determine how close the real gradients and the now inexact analytic gradients are each of the six structure factors were changed by 10^{-5} in turn and the pattern recalculated. Each time the numeric gradient was found using,

$$\frac{\partial \chi^2}{\partial U_{\mathbf{G}}} = \frac{\chi^2_{orig} - \chi^2_{changed}}{10^{-5}} \tag{3.33}$$

The results are shown in Table 3.1 for the real and imaginary parts of the struc-

Parameter	analytic gradient	numerical gradient
$\Re(1\bar{1}1)$	-85.183	-85.222
$\Im(1\bar{1}1)$	-223.331	-223.288
$\Re(1\bar{1}\bar{1})$	182.447	182.429
$\Im(1\bar{1}\bar{1})$	-160.087	-160.111
$\Re(002)$	-77.349	-77.362
$\Im(002)$	-108.513	-108.495
$\Re(00\bar{2})$	36.529	36.545
$\Im(00\bar{2})$	-112.347	-112.365
$\Re(2\bar{2}0)$	53.981	53.963
$\Im(2\bar{2}0)$	15.188	15.153
$\Re(1\bar{1}3)$	-4.101	-4.098
$\Im(1\bar{1}3)$	23.412	23.417
$\Re(1\bar{1}\bar{3})$	30.287	30.291
$\Im(1\bar{1}\bar{3})$	3.507	3.511
$\Re(2\bar{2}2)$	29.638	29.634
$\Im(2\bar{2}2)$	2.892	2.895

Table 3.1: Comparison of analytic and numeric gradients, showing that there is very little difference between them despite using the Bethe approximation.

ture factors out to (220). Comparing the 'analytic' gradients with the numerical gradients reveals that there is very little difference between them, less than 0.3% in all cases. Therefore, it seems safe to assume that the quasi Newton minimisation routine will be able to find the χ^2 minimum using the gradients which result from the analytic gradient expression (equation (3.5)) of Bird and Saunders.

However, before being completely confident that the new method will introduce no unexpected errors we must complete one final test which mimics a real structure factor refinement process as closely as possible. This will be attempted in the next section.

3.5.4 Full Fitting

As a final test for the overall accuracy of the fitting method using the Bethe approximation the fitting routine was allowed to run to completion. Again the exact 345 beam calculation was used to represent the experimental data set and the values of the real and imaginary parts of six low order structure factors altered randomly by 1-2%, thereby simulating the real situation where independent atom structure factors are used as a starting point for the routine. The routine was then allowed to run until no further change in the structure factors was obtained.

The results are shown in table 3.2. It can be seen that the error between the structure factors used to calculate the exact pattern (labelled True Value in the table) and the final structure factors when χ^2 has been minimised (labelled Fitted Value) are small, in most cases correct to three decimal places. This compares to experimental results which are often correct to two decimal places or less, see section 3.6 and [54].

Section 3.5 has shown that the Bethe approximation is an improvement over second order perturbation theory since it requires fewer inner beams to produce an accurate pattern. It has also been shown that it can be applied to the full pattern

Structure factor	True Value	Fitted value	Error
$\Re(1\bar{1}1)$	-2.26811	-2.26781	0.00030
$\Im(1\bar{1}1)$	0.06149	0.06115	0.00034
$\Re(1\bar{1}\bar{1})$	-2.25989	-2.26057	0.00068
$\Im(1\bar{1}\bar{1})$	-0.18140	-0.18044	0.00096
$\Re(002)$	-0.00583	-0.00579	0.00004
$\Im(002)$	0.15926	0.15943	0.00017
$\Re(00\bar{2})$	0.00583	0.00786	0.00203
$\Im(00\bar{2})$	-0.15926	-0.15954	0.00028
$\Re(2\bar{2}0)$	-2.13336	-2.13035	0.00301
$\Im(2\bar{2}0)$	-0.08139	-0.08570	0.00431
$\Re(1\bar{1}3)$	1.27982	1.27840	0.00142
$\Im(1\bar{1}3)$	0.10669	0.10879	0.00210

Table 3.2: Fitted values of the first six structure factors with the 'true' value and error.

matching routine without having to alter the method of gradient calculation. It can now be applied to a real system as described in the next section.

3.6 Experimental Results

It is now possible to run a fit between theory and experiment to find the values of some low order structure factors. This was done for the Si[110] zone axis using a Hitachi HF2000 FEG-TEM at Bristol University by Saunders et al [12]. The microscope had an operating voltage of 198.6 $\pm$0.2kV and a probe size of 3 nm and the nominal sample thickness was about 3150Å. To reduce the background noise the sample was cooled to liquid nitrogen temperatures and a Gatan Imaging Filter was attached to the microscope. The experimental CBED pattern, taken

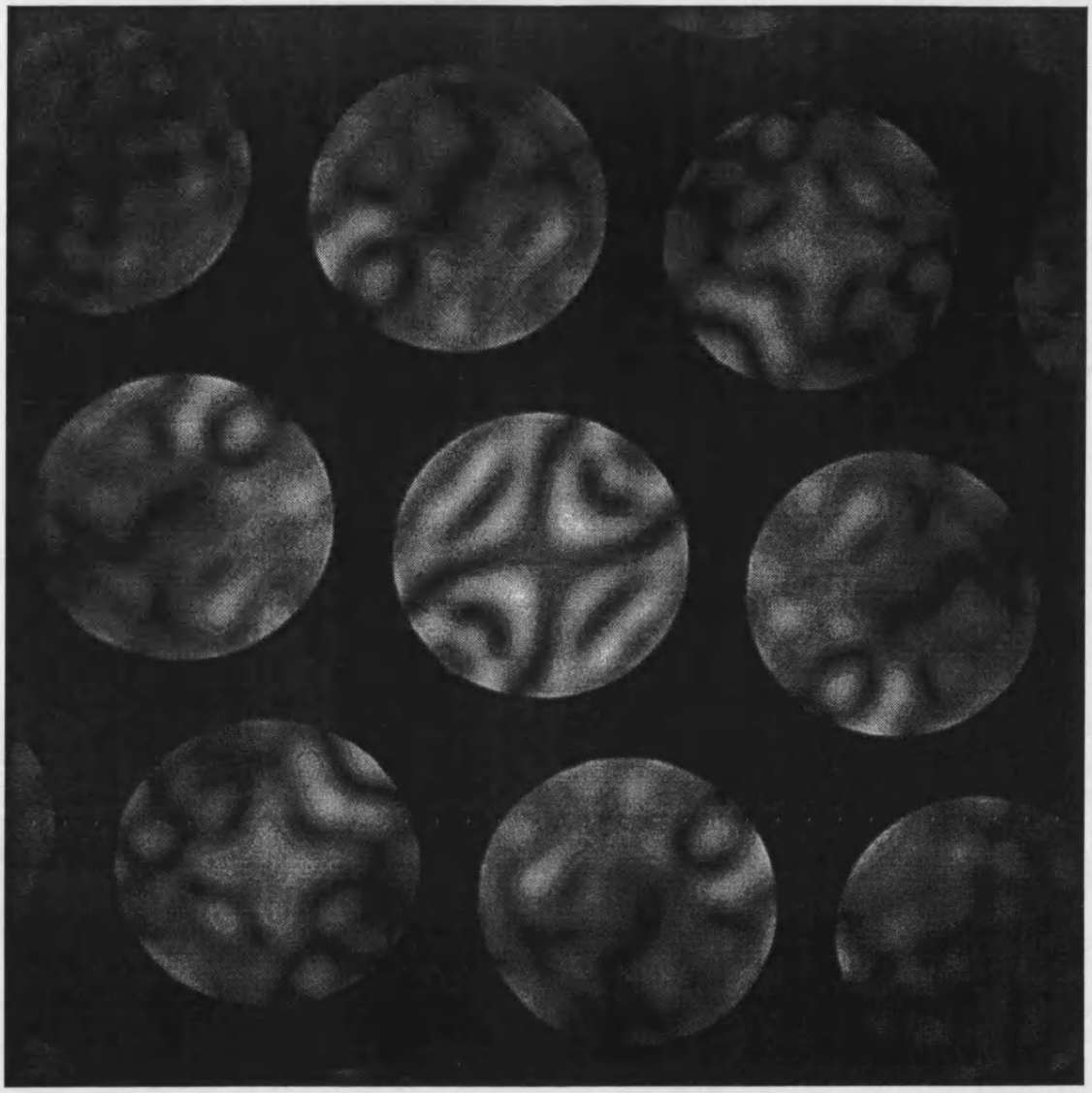

Figure 3.13: Si {110} experimental CBED pattern used in structure factor determination.

by P.A. Midgley, is shown in figure 3.13, the inner seven discs (000, 111, 002) were used for fitting as described in section 3.3. A grid of 21×21 pixels was used for each disc, giving a total of 3087 data points.

The theoretical patterns were calculated using an inner beam set of 121 beams with an additional 270 beams included using the Bethe approximation. The total time taken for the fitting was approximately two days using a DEC Alpha 3400 work station. The Debye-Waller factor used for Si in these calculations at liquid Nitrogen temperature was 0.25Å^2. The starting values of the structure

Structure Factor	X-ray Measurement	CBED Measurement
{111}	10.603(3)	10.600(1)
{220}	8.388(2)	8.385(5)
{113}	7.681(2)	7.68(2)
{222}	0.182(1)	0.15(1)
{004}	6.996(1)	6.98(5)
{331}	6.726(2)	6.79(6)

Table 3.3: X-ray and CBED measured values for the first six structure factors of Si[110]. Error in last place is shown in brackets.

factors were those of the independent atom values. The background levels were estimated by measuring intensities between discs and the thickness and normalisation constant were estimated using the thickness scan method, explained in section 3.3. More details of the experimental operation can be found in [12] along with a detailed discussion of the results.

The results of this fit for the first six structure factors are shown in table 3.3 where the structure factors have been converted into the equivalent X-ray structure factors of units $e/atom$ using the Mott formula given below [55],

$$f_g^X = Z\exp(-Ms^2) - \frac{4\pi\epsilon_0 2h^2}{m_0\gamma e^2} f_g^{el} s^2 \tag{3.34}$$

where Z is the atomic number, $s = |g|/4\pi$, $\exp(-Ms^2)$ is the Debye-Waller factor and f_g^{el} is the electron scattering factor given by,

$$U_{\mathbf{g}}^{el} = \frac{4\pi}{v_c}\sum_i f_{\mathbf{g}}^{el}\exp(-i\mathbf{g}.\mathbf{r}_i). \tag{3.35}$$

Here, v_c is the volume of the unit cell and the sum is over all atomic positions in the unit cell $\mathbf{r}_i$.

Equivalent results from X-ray Pendellosung measurements have been included. It can be seen that the measured values are in close agreement in most cases with

only the result from the (222) structure factor being significantly different.

3.7 Summary

The use of CBED as a method of determining low order structure factors has been considered. For this method to be effective there are two major requirements. First, only elastically scattered electrons can be used as including the theory of inelastic scattering would make the pattern matching method too complicated to be practical. Therefore, the sample must be cooled and the CBED patterns must be energy filtered. Second, the theoretical calculations must be fully converged. However, the time taken to get a fully converged CBED pattern can be prohibitively long and some form of approximation is needed to reduce this time.

The approximation method used in the work presented here is the Bethe approximation. It has been shown that this method has several advantages over second order perturbation theory which had previously been used. Both the eigenvectors and the eigenvalues are altered with the changes in the eigenvalues not being limited to the second order as in second order perturbation theory. Also, no additional cut off between the inner and outer beam sets is required since there cannot be a division by zero in this method. It has been shown that this combination of advantages leads to the Bethe approximation giving a converged pattern with fewer beams than the second order perturbation theory. Additionally, it was found that the analytic gradients derived for use with second order perturbation theory could still be used for the Bethe approximation. Therefore, the full fitting routine could be expected to work correctly with this approximation.

Finally, the fitting method, including the new Bethe approximation, was used to determine the low order structure factors of Si [110] and was found to give similar results to previous measurements using X-rays.

Chapter 4

Inelastic Electron Diffraction and Imaging

In this chapter and the next we will be concentrating on some of the inelastic effects of High Energy Electron Diffraction discussed earlier. In particular we will be considering atomic electron excitation. It will be shown that the energy loss filtering system used in the last chapter to eliminate these contributions can be used to study them instead. Images arising from fast electrons which have caused a particular atomic excitation will be considered. In particular we wish to gain an understanding of crystalline structures through chemical mapping i.e. determining the elements which make up the crystal and their distribution through that crystal.

If the fast electrons are energy filtered then they can be used to image the atoms of any element and thus produce a chemical map. Much work has already been done to understand how the resolution limit of these images is affected by the electron microscope itself [56, 11]. Here we will be considering how the underlying physics of the process limits resolution and affects the final image i.e. we will consider the differences between an image from a single atom and one from an atom within a surrounding crystal, highlighting the effects of dynamical diffraction.

In Section 4.1 of this chapter chemical mapping and the limits to the obtainable resolution of these maps will be discussed. In section 4.2 the model of the atomic electron excitation used for our work will be developed and the approximations explained. The model was developed to emphasise the fundamentals of imaging and diffraction, i.e. size of image, effect of dynamical diffraction etc. It was essential to have a source of localised inelastic electrons but it was not necessary to exactly reproduce the practical situation. Thus the limitations of the microscope were largely ignored and several physical approximations were made.

A hydrogenic model is used to describe the atom in which the atomic excitation takes place. These electronic transitions are assumed to be from one bound state to another rather than ionising the atom. Expressions for the object function intensity are obtained by considering the fast electrons which have caused the excitation. These are developed both for a single atom and for an atom within a surrounding crystal.

In this latter case we must take into account the effects of dynamical diffraction. In section 4.3 the exact form of the transition is taken into account i.e. the atomic number and the electron shells which are involved in the transition (e.g. s to p, p to d). The computer implementation of these models is described in section 4.4 and the results are then summarised in section 4.5.

4.1 Inelastic Scattering

As discussed in chapter 2 the scattering of electrons cannot be described entirely by the theory of elastic scattering. Even if absorption is included into the theory to account for the loss of electrons from the diffraction pattern the theoretical model will differ from the experimental results due to the background of inelastically scattered electrons. Energy filtering systems [35, 3] are an important method of minimising the inelastic background and allowing quantitative comparisons of

elastically scattered CBED patterns to be made, see chapter 3.

However, the use of these filtering systems is not restricted to eliminating inelastic scattering. The filters can be adjusted to allow electrons of any particular energy to pass through (to within $\sim$ 5eV) [3]. Therefore, it is possible to study a material using electrons which have lost some specific amount of energy through an inelastic process. Both plasmon loss (e.g. [57, 58]) and atomic electron excitation (e.g. [59, 60]) are used in this manner. However, thermal diffuse scattering is difficult to use since the energy losses involved are typically $\leq$ 50 meV and cannot be resolved from the purely elastically scattered electrons. One of the important applications of energy filtering has been the understanding of the chemical composition of materials which is discussed below.

4.1.1 Principles of Chemical Mapping

An important step in understanding the properties of a material is to know its chemical composition. There are a number of ways of measuring this e.g. Energy Dispersive X-ray spectroscopy (EDX) [61] and Z-contrast imaging [62]. However, the results of an analysis give limited information about the location of individual elements or are limited to well defined grain boundaries. With the development of energy filtering, or Electron Energy Loss Spectroscopy (EELS), it has become possible to study the spatial position of different elements within a particular structure by making use of atomic electron excitations.

To understand the principle behind this type of chemical mapping we must first consider how the number of fast electrons causing the transitions varies with the amount of energy lost due to inelastic collision. Consider the electron intensity versus energy loss graph shown in figure 4.1, the greatest number of electrons is found in the zero loss peak with the intensity falling off as the energy loss increases. This indicates that the majority of scattering is elastic or low loss and explains why energy filtering of elastically scattered electrons removes the

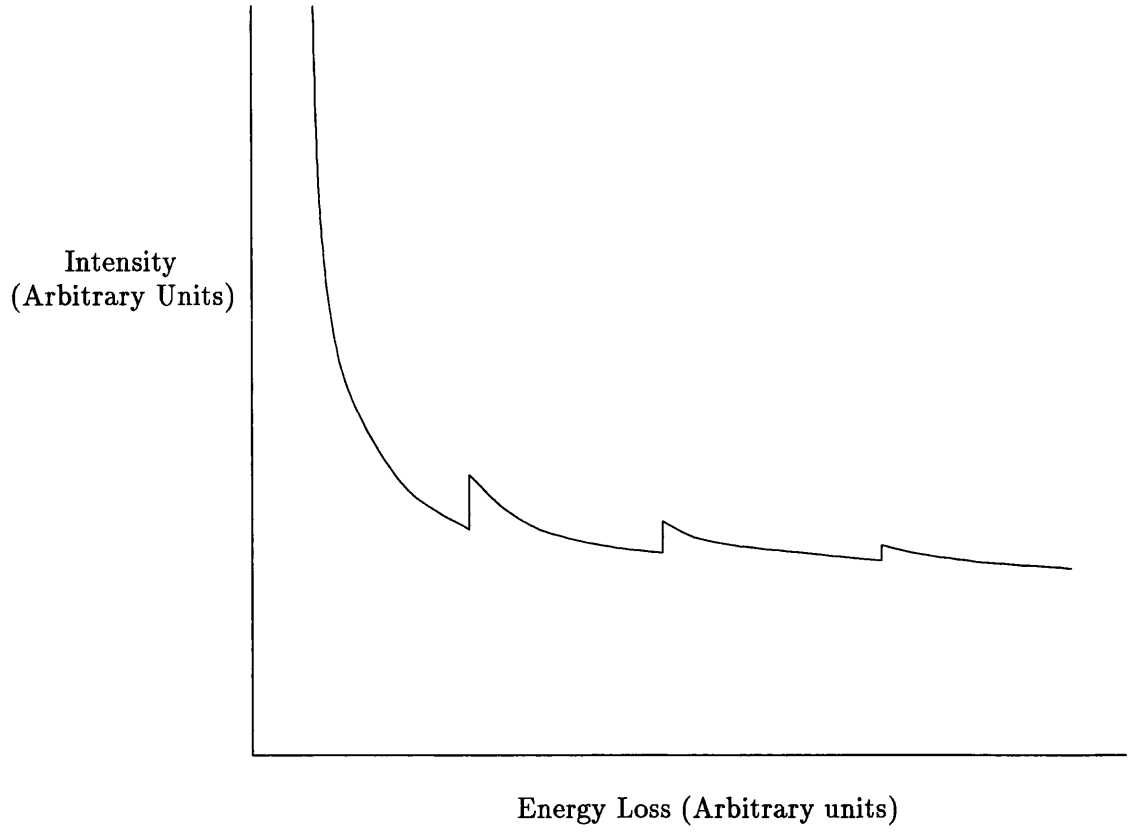

Figure 4.1: Idealised EELS spectrum.

background haze while keeping the diffraction features. The fall off in intensity can be understood since, except for atomic electron excitation, as the energy loss increases so too does the average number of inelastic events. Atomic electron excitation is also less likely at higher energy losses but only a single scattering event is required.

Superimposed on this decline in intensity is a set of peaks which are formed when fast electrons excite a core electron to some higher state, each peak representing a different core excitation. These different peaks may be due to excitation of different core electrons within the same element or the same core electron excitation but from different elements each of which have different energies. By studying these different peaks it is possible to gain an understanding of the proportion of various elements within the crystal [35, 63].

4.1.2 Limits of Resolution in Chemical Mapping

It can be seen from the above that if an energy filter is set to collect electrons which have lost a certain amount of energy (corresponding to a core excitation) then a significant proportion of the electrons collected will have lost their energy due to an interaction with a specific element. There are a number of points to consider before using this information to create a chemical map. First, a large number of electrons will have lost their energy due to multiple scattering and must be subtracted. There are two main ways of subtracting this background, see figure 4.2. The simplest is to measure the intensity of the image at each pixel just before the excitation edge i.e. use only the values from I_2 in figure 4.2 and assume that this value is constant for the whole peak and subtract it from the intensity values at the equivalent pixel [64]. The other method takes two measurements which do not overlap, I_1 and I_2, before the edge and uses a power law to estimate the true value of the background in the region where the measurement is being taken. The background intensity to be subtracted is then given by [65, 66],

$$I_b = \frac{A}{1-r}\left[E_4^{1-r} - E_3^{1-r}\right]. \tag{4.1}$$

There are two major ways of using EELS to produce chemical maps [63], the first relies on the use of a focused electron probe (STEM) being scanned over an area of the sample allowing detailed information of the chemical make up of the material to be found. A single scan can be used to produce the complete chemical map since as many energy loss windows can be examined as required. See [67, 68, 69] for examples of this method.

However, using this technique restricts the area of sample which can be considered since the beam must be scanned over the whole sample which for a large area can take of the order of one hour. During this time specimen drift may occur making the measurements inaccurate. Therefore, the method tends to be used for intermediate resolution chemical maps. The other method of creating chemical

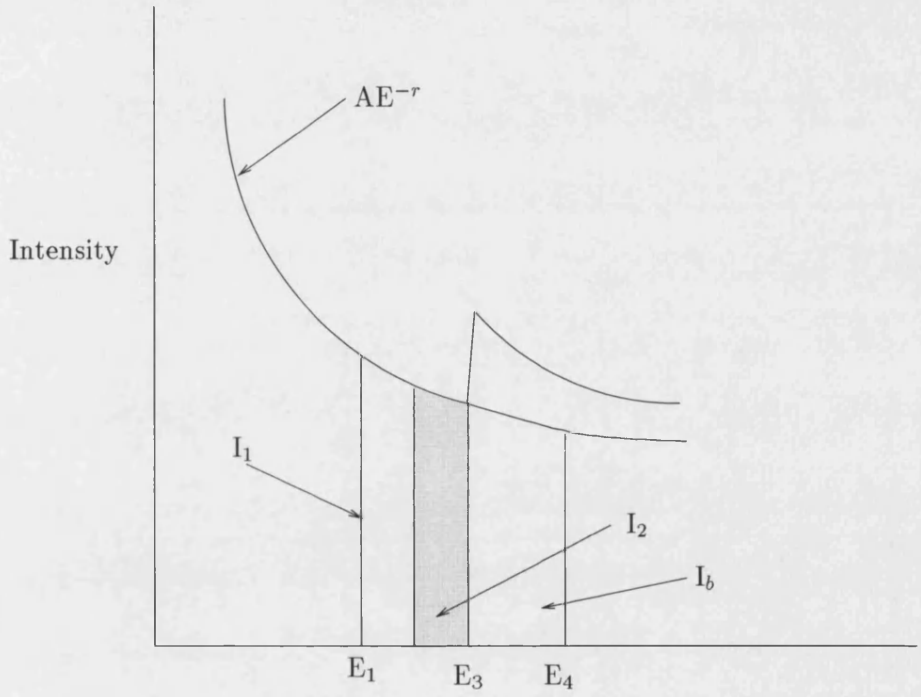

Figure 4.2: Diagram showing how the background is subtracted from an EELS map. I_1 and I_2 are measured and a power law is used to extrapolate the background value to the exact energy loss window being measured.

maps using electron excitation uses a GATAN imaging PEELS system [3]. In this case a parallel beam illuminates the whole area of interest and the whole image is formed at once but only for a single energy loss window. Therefore, for a complete chemical map of the region several images must be obtained, thus increasing the radiation dose and the potential damage to the sample. The time taken to do this can be of the order of a few seconds and if only a few energy loss windows need to be taken the problem of specimen drift can be overcome.

However, in both of these methods there are important restrictions on the resolution limit due to both the underlying physics and microscope parameters. These have been addressed in a number of papers for example, [70, 71, 72, 73, 74]. Here we will concentrate on the restrictions imposed on the Transmission Electron Microscope, using a GATAN imaging PEELS, although many of the problems are common to both methods.

There are several practical restrictions on how high a resolution can be obtained using Energy Filtered TEM (EFTEM) for chemical mapping. A detailed description has been given in [11] and references there in. The important parameters have been shown to include, signal to noise ratio, spherical aberration, radiation damage, instrument instabilities and imperfect image detectors. The most important factors are considered below.

First, the signal to noise ratio plays an important role [75], it must be noted that the signal used to produce the chemical map can be several times lower than the elastic scattering level, becoming smaller as the energy loss increases. Therefore, if the number of atoms which contribute to the signal gets smaller i.e. higher resolution, then the signal becomes even less significant until a point is reached where no signal can be detected due to the ever increasing importance of statistical fluctuations [10]. However, it is claimed that although signal to noise ratio is important, by using brighter illumination, FEG rather than LaB_6 sources, and longer exposure times this need not be the most significant limiting factor [11]. However, it should be noted that these solutions will lead to greater

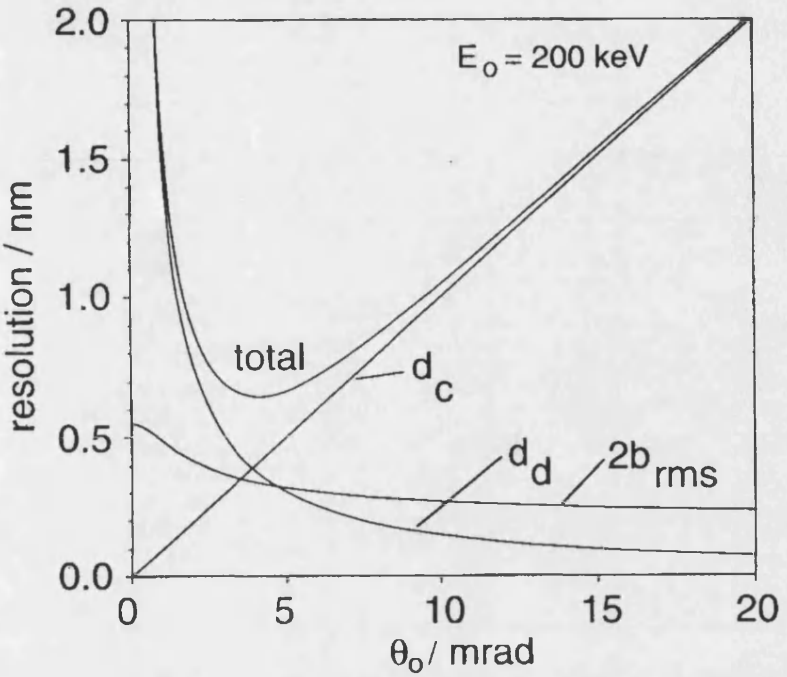

Figure 4.3: Factors limiting resolution, see text for details.

sample damage and possibly specimen drift.

Another important problem which has been considered in several papers is the chromatic aberration of the magnetic lenses which form the image. This is primarily a problem for CTEM where the objective lens focuses a beam with a spread of energies (at least 5eV) where as for STEM the objective lens focuses a nearly monochromatic beam of electrons. The maximum delocalisation due to chromatic aberrations is given by,

$$d_c = \left(\frac{C_c w}{E_0}\right)\theta_0. \tag{4.2}$$

Here, C_c is the coefficient of chromatic aberration, w is the size of the energy window of the filter, E_0 is the energy of the fast electron and θ_0 is the maximum scattering angle allowed by the objective aperture. As can be seen from equation (4.2) the image localisation depends upon the size of the objective aperture, the smaller the aperture the smaller the effect of chromatic aberration. It has been

demonstrated [56, 11, 76] that this aberration is likely to limit the resolution, possibly to a minimum of 1nm.

The diffraction limit is determined by the wavelength of the electron and the size of the objective aperture, so that smaller aperture sizes lead to lower resolution limits [77]. It is given by,

$$d_d = \frac{0.6\lambda}{\theta_0} \tag{4.3}$$

where λ is the electron wavelength. Finally, the last limit to resolution we will consider is the delocalisation of the interaction between the fast and atomic electron. A simple expression given by [78] is often used, although it does not take into account the quantum mechanical nature of the interaction. If the fast electron can excite the atomic electron at a distance b then the image is broadened by $2b_{rms}$ where,

$$b_{rms} = \frac{\hbar\nu\theta_0}{\Delta E}\left[(\theta_0^2 + \theta_E^2)\ln(1 + \frac{\theta_0^2}{\theta_E^2})\right]^{1/2}. \tag{4.4}$$

Here, ν is the speed of the fast electron, ΔE is the energy loss and θ_E is given by $\theta_E = \Delta E/2E_0$ with E_0 being the initial energy of the fast electron. The value of b_{rms} is nearly constant with respect to the objective aperture. See [79] for a discussion of semiclassical and full quantum mechanical representations of the delocalisation using the impact parameter.

Figure 4.3 shows the resolution loss due to delocalisation, chromatic aberration and the diffraction limit as a function of the objective aperture at an energy loss of 500eV, energy window of 20 eV and a coefficient of chromatic aberration of 1mm on a 200keV EFTEM [11]. In this particular case it can be seen that the maximum resolution of $\sim$ 6Å is achieved for an objective aperture of about 5 mrads. Typical recent investigations have demonstrated resolutions down to 1nm [80]. Claims of higher resolution have been made and are discussed in more

detail in section 5.4.

It can be seen from the above discussion and figure 4.3 that a compromise must be made to achieve the highest possible resolution. The value of objective aperture is dictated primarily by the chromatic aberration of the microscope since the effect of both the diffraction limit and the impact parameter or delocalisation are set for a given system. Detailed investigations into the effects of this aberration have been undertaken by a number of people [56, 81]. However, the underlying physical limit to the attainable resolution is set by the diffraction limit and delocalisation, and these are less well understood. In the models developed in the rest of this chapter, the microscope limitations are ignored, e.g. chromatic aberration and signal to noise ratio but the diffraction limit and a full quantum mechanical model of the delocalisation are implicit in the models. Thus we are able to investigate the situation where all the scattered electrons are used to create the image, i.e. a very large objective aperture and where chromatic aberrations are no longer an issue. This gives an indication of the fundamental resolution limit to this type of elemental imaging, this model is developed in section 4.2.1. Additionally, the previous work on this topic has considered only an isolated atom, the effects of the surrounding crystal have not been considered. A model will be developed in section 4.2.3 to examine the effects the dynamical diffraction, which results from the inclusion of a surrounding crystal, has on the basic object function.

4.2 Atomic Excitation Models

The aim of the work presented here is to study the underlying physics of the fast electron / source atom interaction rather than the experimental limitation outlined in section 4.1.2. Therefore, the model used to study the interaction needs to be as simple as possible, so that the results are not clouded with needless detail but at the same time it must retain the essential physics of the real world.

As a starting point it was decided that since the microscope capabilities were well researched there was no need to include the parameters which limited their effectiveness, i.e. chromatic aberrations and signal to noise ratio. Therefore, the images that we will be studying are better described as object functions since they remain unaltered by any experimental imaging techniques.

In the next section we will introduce the model to be used for this investigation, the approximations used will be explained and an expression for the intensity of the free space object function derived. This model will also provide the basis for the dynamical diffraction model which will be derived in the section following.

4.2.1 Independent Atom Model

To study the underlying resolution limit it is not necessary to calculate either the exact shape or intensity of the object function for a specific real case, rather we are interested in the qualitative results which will provide approximate answers as well as showing trends. For this reason several simplifications can be used to make the model both easier to calculate and more adaptable.

First, the atom in which the inelastic event takes place will be assumed to be a hydrogenic atom. This is done so that the calculations can be made easier as only the atomic and single electron charge need to be considered when modelling the interaction. It is then simple to change the energy loss of the interaction by changing the atomic number of the hydrogenic atom.

The second major approximation concerns the final state of the atomic electron. In a real system the electron would have to be excited from a bound state into a free (conduction band) state [82, 83]. However, the calculation is considerably simplified if the atomic electron in the hydrogenic atom is excited from one bound state to another. This is because only one final state of the atomic electron has to be considered rather than many. However, by doing this it appears that the

source atom is left in two very different states. In the real case the final state is delocalised whereas in the proposed approximation it is localised.

If we remember that the purpose of this model is to provide a source of inelastically scattered electrons with which we can investigate the effect of dynamical diffraction rather than give an accurate quantitative representation of reality then this approximation need not be a problem. However, the differences between the two approaches should not be over emphasised. At the edge of the conduction band the final states may be like the bound states we are considering in this model, for example consider the case of atomic excitation on the Carbon atom. Think of the excited state in the Linear Combination of Atomic Orbital (LCAO) framework [21]. The core states fill the $1s^2 2s^2 2p^2$ set of orbitals and at the edge of the conduction band the state simplifies to sp^3. Therefore, at the edge, the final state consists of atomic like $2s$ and $2p$ states over the region in which the atomic orbital is significant. Making our bound to bound calculation a reasonable approximation to the edge of a bound to free transition.

The problem of defining an excitation from one bound state to another has been developed previously [84] and is given here. We begin by considering the Hamiltonian of the interaction between a fast electron and a single hydrogenic source atom which can be written as,

$$\hat{H} = -\frac{\hbar^2}{2m}\nabla_1^2 - \frac{\hbar^2}{2m}\nabla_2^2 - \frac{e^2}{4\pi\epsilon_0|\mathbf{r}_1|} - \frac{e^2}{4\pi\epsilon_0|\mathbf{r}_2|} + \frac{e^2}{4\pi\epsilon_0|\mathbf{r}_1 - \mathbf{r}_2|}. \qquad (4.5)$$

The nucleus is assumed to be fixed at the origin. The subscripts refer to the fast (1) and source or atomic (2) electrons, the other symbols have their usual meanings. The wave function of the system is given by

$$\hat{H}\Psi = (E_1 + E_2)\Psi \qquad (4.6)$$

with a non relativistic fast electron energy of $E_1 = \hbar^2 k^2/2m$ and source electron energy of $E_2 = -13.6eV$ for the ground state of the hydrogen atom. If it is

assumed that the fast and source electrons are distinguishable and no exchange effects need be included, then a solution of the form $\Psi = \sum_m \phi_m(\mathbf{r}_1)u_m(\mathbf{r}_2)$ can be sought where m is a set of orthogonal states. Equation (4.6) becomes,

$$\begin{aligned}
\sum_m u_m(\mathbf{r}_2)\left(\frac{-\hbar^2}{2m}\right)\nabla_1^2\phi_m(\mathbf{r}_1) &+ \sum_m \phi_m(\mathbf{r}_1)\left(\frac{-\hbar^2}{2m}\right)\nabla_2^2 u_m(\mathbf{r}_2) \\
-\sum_m \frac{e^2}{4\pi\epsilon_0 r_1}u_m(\mathbf{r}_2)\phi_m(\mathbf{r}_1) &- \sum_m \frac{e^2}{4\pi\epsilon_0 r_2}u_m(\mathbf{r}_2)\phi_m(\mathbf{r}_1) \\
+\sum_m \frac{e^2}{4\pi\epsilon_0|\mathbf{r}_1-\mathbf{r}_2|}\phi_m(\mathbf{r}_1)u_m(\mathbf{r}_2) &= \sum_m (E_1+E_2)\phi_m(\mathbf{r}_1)u_m(\mathbf{r}_2). \qquad (4.7)
\end{aligned}$$

We know that the atomic states for a hydrogenic atom are given by,

$$\left(\frac{-\hbar^2}{2m}\nabla_2^2 - \frac{e^2}{4\pi\epsilon_0 r_2}\right)u_n(\mathbf{r}_2) = E_n u_n(\mathbf{r}_2) \qquad (4.8)$$

thus if the second and third terms of equation (4.7) are combined and $\sum_m (E_1 + E_2)\phi_m(\mathbf{r}_1)u_m(\mathbf{r}_2)$ is subtracted from both sides we get,

$$\begin{aligned}
\sum_m u_m(\mathbf{r}_2)(\frac{-\hbar^2}{2m})\nabla_1^2\phi_m(\mathbf{r}_1) &+ \sum_m \phi_m(\mathbf{r}_1)u_m(\mathbf{r}_2)(E_m - E_1 - E_2) \\
-\sum_m \frac{e^2}{4\pi\epsilon_0 r_1}u_m(\mathbf{r}_2)\phi_m(\mathbf{r}_1) &+ \sum_m \frac{e^2}{4\pi\epsilon_0|\mathbf{r}_1-\mathbf{r}_2|}\phi_m(\mathbf{r}_1)u_m(\mathbf{r}_2) = 0. \qquad (4.9)
\end{aligned}$$

As explained earlier rather than allowing the atom to be ionised it can be chosen to be excited to some bound state u_n. To refine equation (4.9) so that we can consider only the excitation into this state we multiply it by $u_n^*(\mathbf{r}_2)$ and integrating over all $\mathbf{r}_2$ we obtain,

$$\begin{aligned}
\frac{-\hbar^2}{2m}\nabla_1^2\phi_n(\mathbf{r}_1) - (E_1+E_2-E_n)\phi_n(\mathbf{r}_1) &- \frac{e^2}{4\pi\epsilon_0|\mathbf{r}_1|}\phi_n(\mathbf{r}_1) \\
+\sum_m \langle u_n|\frac{e^2}{4\pi\epsilon_0|\mathbf{r}_1-\mathbf{r}_2|}|u_m\rangle\phi_m(\mathbf{r}_1) &= 0. \qquad (4.10)
\end{aligned}$$

The Dirac brackets contain an implicit integral over $\mathbf{r}_2$. We can now split this equation to show the elastic and inelastic parts separately, i.e. we move the inelastic diffraction (from state m into state n) onto the right hand side of the equation leaving only the elastic diffraction of the inelastically scattered electron on the left hand side (state n to state n).

$$\left(\frac{-\hbar^2}{2m}\nabla_1^2 - (E_1 + E_2 - E_n) + \langle u_n|\frac{e^2}{4\pi\epsilon_0|\mathbf{r}_1 - \mathbf{r}_2|}|u_n\rangle - \frac{e^2}{4\pi\epsilon_0|\mathbf{r}_1|}\right)\phi_n(\mathbf{r}_1) = -\sum_{m\neq n}\langle u_n|\frac{e^2}{4\pi\epsilon_0|\mathbf{r}_1 - \mathbf{r}_2|}|u_m\rangle\phi_m(\mathbf{r}_1) \quad (4.11)$$

If we assume that the right hand side of equation (4.11) is small i.e. ignoring inelastic scattering, then with the atom being in some initial state u_i the equation for ϕ is given by,

$$\left(\frac{-\hbar^2}{2m}\nabla_1^2 - E_1 + \langle u_i|\frac{e^2}{4\pi\epsilon_0|\mathbf{r}_1 - \mathbf{r}_2|}|u_i\rangle - \frac{e^2}{4\pi\epsilon_0|\mathbf{r}_1|}\right)\phi_i(\mathbf{r}_1) = 0. \quad (4.12)$$

This describes the elastic scattering of the fast electron with the scattering potential $V_{eff}(\mathbf{r}_1)$ being given by,

$$V_{eff}(\mathbf{r}_1) = \langle u_i|\frac{e^2}{4\pi\epsilon_0|\mathbf{r}_1 - \mathbf{r}_2|}|u_i\rangle - \frac{e^2}{4\pi\epsilon_0|\mathbf{r}_1|} \quad (4.13)$$

which has contributions from both the nucleus and the electron. Returning to the inelastic scattering case where the RHS of equation (4.11) is not insignificant, we require the source term ϕ_i to be on the right hand side. The atom is initially in state i allowing the sum over m to be simplified to the single state i. The equation for single inelastic scattering is now given by,

$$\left[\frac{-\hbar^2}{2m}\nabla_1^2 - (E_1 + E_2 - E_n) \quad + \quad \langle u_n|\frac{e^2}{4\pi\epsilon_0|\mathbf{r}_1 - \mathbf{r}_2|}|u_n\rangle - \frac{e^2}{4\pi\epsilon_0|\mathbf{r}_1|}\right]\phi_n(\mathbf{r}_1) = \langle u_n|\frac{e^2}{4\pi\epsilon_0|\mathbf{r}_1 - \mathbf{r}_2|}|u_i\rangle\phi_i(\mathbf{r}_1) \tag{4.14}$$

The energy of the fast electron is much greater than the scattering potential, i.e. the scattering potential is a perturbation of the total energy so that scattering from one atom is weak [84, 85] allowing the Born approximation to be made where we assume a single scattering event, i.e. elastic scattering of the inelastic wave is ignored. Thus we set $V_{eff}(\mathbf{r}_1) = 0$ in both equations (4.12) and (4.14), the equation for the inelastic wave is given by,

$$\left[\frac{-\hbar^2}{2m}\nabla^2 - (E_1 + E_2 - E_n)\right]\phi_n(\mathbf{r}_1) = -\langle u_n|\frac{e^2}{4\pi\epsilon_0|\mathbf{r}_1 - \mathbf{r}_2|}|u_i\rangle\phi_i(\mathbf{r}_1). \tag{4.15}$$

4.2.2 Independent Atom Object Function

We must now find a solution for $\phi_n(\mathbf{r}_1)$, this can be achieved using a Green's function method where [86],

$$\phi_n(\mathbf{r}) = \int d\mathbf{r}' G(\mathbf{r};\mathbf{r}')V(\mathbf{r}')\phi_i(\mathbf{r}'). \tag{4.16}$$

$\mathbf{r}_1$ has been replaced by the more usual symbol of $\mathbf{r}'$ when considering Greens functions. G is the free space Green's function, $V(\mathbf{r}')$ is the first term on the RHS of equation (4.15) i.e. $V(\mathbf{r}') = \langle u_n|\frac{e^2}{4\pi\epsilon_0|\mathbf{r}'-\mathbf{r}_2|}|u_i\rangle$ and is the matrix element for inelastic scattering the Dirac brackets imply an integral over $\mathbf{r}_2$.

In this case the incident fast electron can be described using a plane wave since there is no crystal surrounding the source atom. Therefore, the wave function is obtained by using the free space Green's function. However, in the next section we want to create a model including a surrounding crystal, in this case we will use the projection approximation (2.11) of chapter 2,

$$[-\nabla^2_{\mathbf{R}} + U^{(0)}(\mathbf{R})]\phi(\mathbf{r}) = 2ik\frac{\partial\phi}{\partial z}. \tag{4.17}$$

To keep the two models consistent we use this approximation but for the free space model we must set the crystal potential term $U^{(0)}(\mathbf{R}) = 0$. We split the incoming wave function into x-y and z components using the parabolic approximation also discussed in chapter 2 i.e.,

$$\psi_i = \exp(i\mathbf{K}.\mathbf{R})\exp(-iK_z^2/2k). \tag{4.18}$$

The free space Greens function is then,

$$G = \frac{1}{2ik}\int \mathrm{d}\mathbf{K}'\ \exp(K'(R-R'))\exp(-iK'^2(z-z')/2k)\Theta(z-z') \tag{4.19}$$

where $\Theta(z-z')$ is the step function which ensures forward propagation. The expression for $\phi_n(\mathbf{r})$ is given by,

$$\begin{aligned}\phi_n(\mathbf{R},z) &= \frac{1}{2ik}\int \mathrm{d}\mathbf{K}' \int \mathrm{d}\mathbf{r}'\ \exp(iK'(R-R')) \\ &\times \exp(-iK'^2(z-z')/2k)\Theta(z-z')V(\mathbf{r}').\end{aligned} \tag{4.20}$$

This equation then simplifies to,

$$\begin{aligned}\phi_n(\mathbf{R},z) &= \frac{1}{2ik}\int \mathrm{d}\mathbf{K}'\ \exp(iK'(R))\exp(-iK'^2(z)/2k) \\ &\times \int \mathrm{d}\mathbf{r}'\ \langle U_n \left|\frac{e^2\exp(-i\mathbf{q}.\mathbf{r}')}{4\pi\epsilon_0|\mathbf{r}'-\mathbf{r}_2|}\right| U_i\rangle.\end{aligned} \tag{4.21}$$

Where $\mathbf{q} = \mathbf{k}' - \mathbf{k}$. On integration over $\mathbf{r}'$ this becomes [84],

$$\phi_n(\mathbf{R},z) = \frac{e^2}{8\pi\epsilon_0 ik}\int \mathrm{d}\mathbf{K}' \frac{\exp(iK'(R))\exp(-iK'^2(z)/2k)}{Q^2+q_z^2}F(\mathbf{q}) \qquad (4.22)$$

where

$$F(\mathbf{q}) = \langle U_n|\exp(-i\mathbf{q}.\mathbf{r}_2)|U_i\rangle. \qquad (4.23)$$

If we assume that the incident electron always travels along $\hat{z}$ then $\mathbf{K} = 0$ and substituting $\mathbf{Q}$ (i.e. $\mathbf{K}' - \mathbf{K}$) into equation (4.22) gives,

$$\phi_n(\mathbf{R},z) = \frac{e^2}{8\pi\epsilon_0 ik}\int \mathrm{d}\mathbf{Q} \frac{\exp(i\mathbf{Q}.\mathbf{R})\exp(-iQ^2z/2k)}{Q^2+q_z^2}F(\mathbf{Q},q_z). \qquad (4.24)$$

This is the expression for the free space object function when recorded at some distance z below the source atom. The term $\exp(-iQ^2z/2k)$ will tend to defocus the object function, however, if the object function is recorded immediately below the source atom, where $z \sim 0$ or the object function is focused then this term reduces to 1 and the object function is given by,

$$I(\mathbf{R}) = \left|\frac{e^2}{8\pi\epsilon_0 ik}\int \mathrm{d}\mathbf{Q} \frac{\exp(i\mathbf{Q}.\mathbf{R})}{Q^2+q_z^2}F(\mathbf{Q},q_z)\right|^2. \qquad (4.25)$$

While this is the final expression for the intensity of the object function we can considerably simplify the calculation of this by splitting the integral into its two component parts which gives,

$$\begin{aligned} I(\mathbf{R}) &= \left|\frac{e^2}{8\pi\epsilon_0 ik}\int_0^\infty \frac{Q\mathrm{d}Q\, F(Q,q_z)}{Q^2+q_z^2}\right. \\ &\times \left.\int_0^{2\pi} \mathrm{d}\phi_Q \exp\left(i|\mathbf{Q}|\mathbf{R}|\cos(\phi_Q-\phi_R)\right)\exp(i\phi_Q)\right|^2. \end{aligned} \qquad (4.26)$$

The phase terms ϕ_Q and ϕ_R are the angles which the $\mathbf{Q}$ and $\mathbf{R}$ vectors make with an arbitrary direction so that $\mathbf{Q}.\mathbf{R} = |\mathbf{Q}|\mathbf{R}|\cos(\phi_Q - \phi_R)$, see figure 4.4. If we

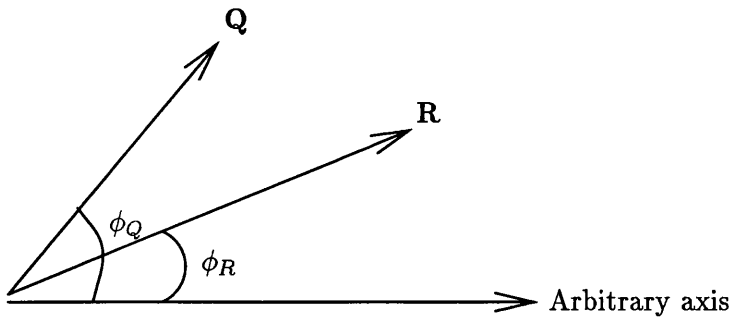

Figure 4.4: The phase angles ϕ_Q and ϕ_R arise from the angle the **Q** and **R** vectors make with some arbitrary direction in the image plane.

now make the substitution that $\phi = \phi_Q - \phi_R$ and note that the integral can range from 0 to π if it is multiplied by 2 then the integral becomes,

$$\begin{aligned} I(\mathbf{R}) &= \left| \frac{e^2}{4\pi\epsilon_0 ik} \int_0^\infty \frac{Q\mathrm{d}Q\, F(Q,q_z)}{Q^2+q_z^2} \exp(i\phi_R) \right. \\ &\times \left. \int_0^\pi \mathrm{d}\phi \exp\left(i|\mathbf{Q}||\mathbf{R}|\cos(\phi)\right) \exp(i\phi) \right|^2 \end{aligned} \tag{4.27}$$

The angular integral is now in the form of a standard integral where, [87]

$$J_n(x) = \frac{i^{-n}}{\pi} \int_0^\pi \exp(ix\cos\theta)\exp(in\theta)\mathrm{d}\theta. \tag{4.28}$$

Here $J_n(x)$ is the n^{th} order first Bessel function at value x. Thus, the intensity of the object function for a single atom in free space is given by,

$$I(\mathbf{R}) = \left| \frac{e^2}{4\pi\epsilon_0 ik} 2\pi \int_0^\infty \mathrm{d}Q\, \frac{J_1(QR)QF(Q,q_z)}{Q^2+q_z^2} \right|^2. \tag{4.29}$$

The phase term $\exp(i\phi_R)$ becomes one on squaring and is therefore not shown.

In this section we have used a Green's function method to find an expression for the inelastic wave function derived in section 4.2.1 and hence the intensity of the

object function. The model assumes that the source atom is independent from all other atoms, the case where it is surrounded by other atoms in a crystal will be considered in the next section.

4.2.3 Inclusion of a Crystal

In this section an equivalent expression for the object function will be found which will include the effects of dynamical diffraction due to a surrounding crystal. The effect of including a surrounding crystal is to require the fast electron to be described by Bloch waves while in the crystal and therefore allow the fast electron to be elastically diffracted.

An important approximation is made in the description of the system, the source atom from which the inelastic scattering takes place is assumed to have no disruptive effect on the crystal lattice which is assumed to be perfect. Thus, the only deviation from the ideal elastic scattering case is due to the atomic excitation in the source atom. By doing this we have isolated the effect of dynamical diffraction upon the original independent atom object function.

As a starting point for the calculation of the inelastic wave function (for the single inelastic scattering case) we should note that as in equation (4.16),

$$\Psi_{\text{inelastic}}(\mathbf{r}) = \int \mathrm{d}\mathbf{r}'\; G(\mathbf{r};\mathbf{r}')V(\mathbf{r}')\Psi_{\text{incident}}(\mathbf{r}') \tag{4.30}$$

where $\Psi_{\text{incident}}(\mathbf{r}')$ is the incident fast electron wave, $V(\mathbf{r}')$ is the inelastic scattering potential and is the same as previously and $G(\mathbf{r};\mathbf{r}')$ is the Green's function which provides the outgoing amplitudes. The projection approximation explained in chapter 2 is applied here so that only scattering in the zero layer is considered. Consider figure 4.5, the incident fast electron will undergo elastic scattering on entering the crystal and within the crystal is given by [88],

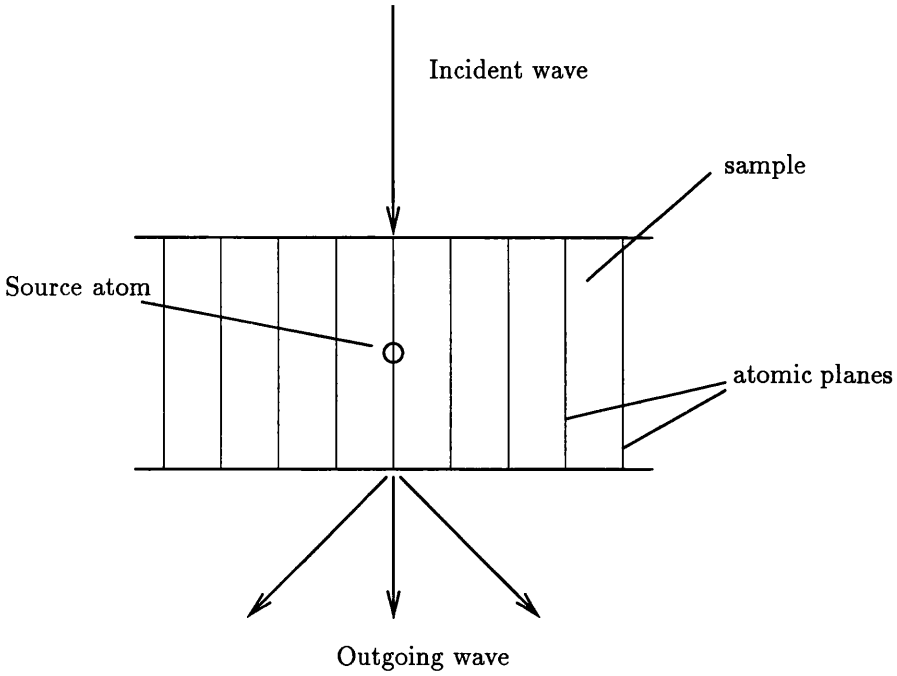

Figure 4.5: Source atom surrounded by crystal.

$$\begin{aligned}\Psi_{\text{incident}} &= \sum_j C_0^{j*}(\mathbf{K}) \sum_{\mathbf{G}} C_{\mathbf{G}}^j(\mathbf{K}) \exp(i(\mathbf{K}+\mathbf{G}).\mathbf{R}') \\ &\times \exp(-is^j(\mathbf{K})z'/2k) \exp(ikz'). \end{aligned} \tag{4.31}$$

Here C are the Bloch wave expansion coefficients with incident orientations of $\mathbf{K}$, j is the branch number, $\mathbf{G}$ is the 2d scattering vector, $\mathbf{K}$ is the transverse component of the incident electron wave vector, k is the magnitude of the incident wave vector, $\mathbf{R}'$ and z' are the radial and z components of the fast electron position respectively. Typically, the work on Electron Energy Loss chemical mapping uses thin crystals to prevent multiple scattering events from making the energy loss peak too weak to be significant. Therefore, we have assumed that no absorption is present i.e. all electrons which undergo inelastic scattering with the source atom are collected.

The Green's function is used to include the effects of elastic scattering of the inelastically scattered wave function and is given by [88],

$$
\begin{aligned}
G &= \frac{1}{8\pi^2 ik} \sum_{j'\mathbf{HG}'} \int \mathrm{d}\mathbf{K}'\, C^{j'}_{\mathbf{H}}(\mathbf{K}') C^{j'*}_{\mathbf{G}'}(\mathbf{K}') \exp(i(\mathbf{K}'+\mathbf{H}).\mathbf{R}) \\
&\times \exp(-is^{j'}(\mathbf{K}')z/2k) \exp(-i(\mathbf{K}'+\mathbf{G}').\mathbf{R}') \exp(is^{j'}(\mathbf{K}')z'/2k) \\
&\times \exp(-ik'(z-z'))\Theta(z-z'). \qquad (4.32)
\end{aligned}
$$

Here $\mathbf{H}$ and $\mathbf{G}'$ are sums over the scattering vectors, $\mathbf{K}'$ is the x-y component of the inelastically scattered electron wave vector, k' is the magnitude of the inelastically scattered wave vector, $\mathbf{R}$ and z are position coordinates of the inelastic wave, j' is the branch number and Θ is a step function which ensures forward propagation of the wave. Writing equation (4.30) in full gives,

$$
\begin{aligned}
\psi(\mathbf{R},z) &= \frac{1}{8\pi^2 ik} \sum_{jj'\mathbf{HGG}'} \int \mathrm{d}\mathbf{K}'\, C^{j'}_{\mathbf{H}}(\mathbf{K}') C^{j'*}_{\mathbf{G}'}(\mathbf{K}') C^{j*}_{0}(\mathbf{K}) C^{j}_{\mathbf{G}}(\mathbf{K}) \\
&\times \exp(i(\mathbf{K}'+\mathbf{H}).\mathbf{R}) \exp(-is^{j'}(\mathbf{K}')z/2k) \exp(ik'z) \\
&\times \int \mathrm{d}\mathbf{r}' \exp(-i\mathbf{Q}.\mathbf{R}') \exp(-iq_z z') V(\mathbf{r}') \qquad (4.33)
\end{aligned}
$$

where $\mathbf{Q}$ is defined as $(\mathbf{K}'+\mathbf{G}')-(\mathbf{K}+\mathbf{G})$ and q_z as $((s^j(\mathbf{K})-s^{j'}(\mathbf{K}'))/2k)-(k-k')$. Since we are only interested in the wave function at the exit surface of the crystal z will always be greater than z' and the step function can be considered as implicit in the expression. It should be noted that we are making an approximation here, the integration over $\int \mathrm{d}\mathbf{r}'$ is for all space but the crystal we are considering is finite. This should not matter since the scope of $V(\mathbf{r}')$ is limited and the integration can be over any range so long as it includes all the significant values of $V(\mathbf{r}')$.

To obtain an expression similar to $F(\mathbf{q})$ of equation (4.23) for the single atom case let us first define a function $M(\mathbf{q})$ as the integral over $\mathbf{r}'$ from equation (4.33) with $V(\mathbf{r}')$ written in full i.e.,

$$
M(\mathbf{q}) = \frac{e^2}{4\pi\varepsilon_0} \int \mathrm{d}\mathbf{r}' \int \mathrm{d}\mathbf{r}_2\, u^*_f(\mathbf{r}_2-\mathbf{r_0}) u_i(\mathbf{r}_2-\mathbf{r_0}) \frac{\exp(-i\mathbf{q}.\mathbf{r}')}{|\mathbf{r}'-\mathbf{r}_2|} \qquad (4.34)
$$

where $\mathbf{r}_0$ is the position of the source atom within the crystal. Let $\mathbf{r}_2 - \mathbf{r}_0$ be called $\mathbf{r}_a$ and $\mathbf{r}'' = \mathbf{r}' - \mathbf{r}_a - \mathbf{r}_0$, after integrating over $\mathbf{r}''$ $M(\mathbf{q})$ becomes,

$$M(\mathbf{q}) = \frac{e^2 \exp(-i\mathbf{q}.\mathbf{r}_0)}{4\pi\varepsilon_0 q^2} \int \mathrm{d}\mathbf{r}_a \, u_f^*(\mathbf{r}_a) u_i(\mathbf{r}_a) \exp(-i\mathbf{q}.\mathbf{r}_a). \tag{4.35}$$

The inclusion of the $\mathbf{r}_0$ term allows the source atom to be moved to any position within the crystal. This will be particularly useful in examining the differences arising from the source atom being placed at various depths and various horizontal positions, see chapter 5. We now define a function $F(\mathbf{q})$ as,

$$F(\mathbf{q}) = \int \mathrm{d}\mathbf{r}_a \, u_f^*(\mathbf{r}_a) u_i(\mathbf{r}_a) \exp(-i\mathbf{q}.\mathbf{r}_a) \tag{4.36}$$

which is the same as that defined in equation (4.23). An analytic expression will be found for the $1s$ to $2p$ and $2p$ to $3d$ transitions of this function in section 4.3.1.

The inelastic wave function of equation (4.33) can be further simplified by making the substitution $\mathbf{K}'' = \mathbf{K}' + \mathbf{H}$, noting that in general $C^j_{\mathbf{G}}(\mathbf{K} - \mathbf{G}') = C_{\mathbf{G}^{j'} - \mathbf{G}'}(\mathbf{K})$ [15] and the eigenvalues are periodic in G. The wave function can now be expressed as a sum over four variables since the sum over $\mathbf{G}'$ and $\mathbf{H}$ is equivalent to simply summing over $\mathbf{G}'$. So that,

$$\begin{aligned} \psi(\mathbf{R}, z) &= \frac{e^2}{16\pi^3 \varepsilon_0 i k} \sum_{jj'\mathbf{G}\mathbf{G}'} \int \mathrm{d}\mathbf{K}' \, C^{j'}_{\mathbf{0}}(\mathbf{K}') C^{j'*}_{\mathbf{G}'}(\mathbf{K}') C^{j*}_{\mathbf{0}}(\mathbf{K}) C^{j}_{\mathbf{G}}(\mathbf{K}) \\ &\times \exp(i\mathbf{K}'.\mathbf{R}) \exp(-is^{j'}(\mathbf{K}') z/2k) \\ &\times \exp(ik'z) \frac{\exp(-i\mathbf{q}.\mathbf{r}_0)}{q^2} F(\mathbf{q}) \end{aligned} \tag{4.37}$$

where $\mathbf{K}''$ has been replaced with $\mathbf{K}'$, $\mathbf{Q}$ is now given by

$$\mathbf{Q} = (\mathbf{K}' + \mathbf{G}') - (\mathbf{K} + \mathbf{G}), \tag{4.38}$$

and q_z by,

$$q_z = ((s^j(\mathbf{K}) - s^{j'}(\mathbf{K}'))/2k) - (k - k'). \tag{4.39}$$

Equation (4.37) is the final expression for the inelastic wave and defines the wave function at any point through the crystal. However, the expression can again be simplified if it is noted that it can be written in the form of a Fourier transform. In this case the amplitude of the inelastic wave at the bottom surface of the crystal is given by,

$$A(\mathbf{R},\mathrm{t}) = \int A(\mathbf{K}')\exp(i\mathbf{K}'\mathbf{R})\mathrm{d}\mathbf{K}'. \tag{4.40}$$

The amplitude at the bottom of the crystal has been chosen since this will be where any experimental measurements will be made and will therefore reveal how dynamical diffraction will affect the object function in reality. The term $A(\mathbf{K}')$ is the diffraction amplitude for the system and is given by,

$$\begin{aligned} A(\mathbf{K}') &= \sum_{jj'\mathbf{G}\mathbf{G}'} C_0^{j'}(\mathbf{K}')C_{\mathbf{G}'}^{j'*}(\mathbf{K}')C_0^{j*}(\mathbf{K})C_{\mathbf{G}}^{j}(\mathbf{K}) \\ &\times \exp(-is^{j'}(\mathbf{K}')t/2k)\frac{\exp(-i\mathbf{q}.\mathbf{r}_0)}{q^2}F(\mathbf{q}). \end{aligned} \tag{4.41}$$

The term $\exp(ik'z)$ from equation (4.37) has been dropped since it is only a phase factor and will not contribute to the intensity of the final object function. $A(\mathbf{K}')$ can be calculated from the above expression and the final object function is then given by $|A(\mathbf{R},t)|^2$.

We have now obtained general expressions for the intensity of the inelastic object function for both a single atom and an atom within a crystal. However, there are still a number of practical points which must be addressed. In particular the transition which takes place in the source atom has not been defined, nor has the resulting expression for $F(\mathbf{q})$ been derived.

4.3 Implementation of Scattering Models

Both of the proceeding sections rely on knowledge of the function $F(\mathbf{q})$ which depends upon the initial and final state of the source atom. Numerical calculation of this function can be time consuming, to over come this the expression is first simplified analytically and then changed into a dimensionless quantity. This allows a single set of numerical calculations to be made for each separate transition and the results put in a lookup table for future reference during calculations.

4.3.1 Source Atom Transition

For the work presented here it was decided that the source atom transition would be from either a $1s$ to $2p$ or $2p$ to $3d$. These transitions were chosen since they are effectively K and L edge transitions respectively which are popular experimental transitions in EELS [89] as well as being the easiest to simplify analytically.

We will derive an expression for $F(\mathbf{q})$ for only one transition and merely state the other expressions since it is a relatively long derivation and further derivations will not provide any significant insights into the physics of the process. We will consider the $1s \rightarrow 2p$ transition, excluding spin there is only one $1s$ state and three $2p$ states. We will concentrate on the $2p_1$ state whose matrix element, $\langle u_{2p1}|\exp(-i\mathbf{q}.\mathbf{r})|u_{1s}\rangle$, is equivalent to the integral

$$F(\mathbf{q}) = \int \exp(-i\mathbf{q}.\mathbf{r}) u^*_{2p1} u_{1s} \mathrm{d}\mathbf{r}. \tag{4.42}$$

The $1s$ state is given by [90],

$$u_{1s} = \frac{1}{\sqrt{\pi}} \left(\frac{Z}{a_0}\right)^{\frac{3}{2}} \exp(\frac{-\rho}{2})$$

where, Z is the atomic number, a_0 is the Bohr radius and ρ is given by $2Zr/na_0$

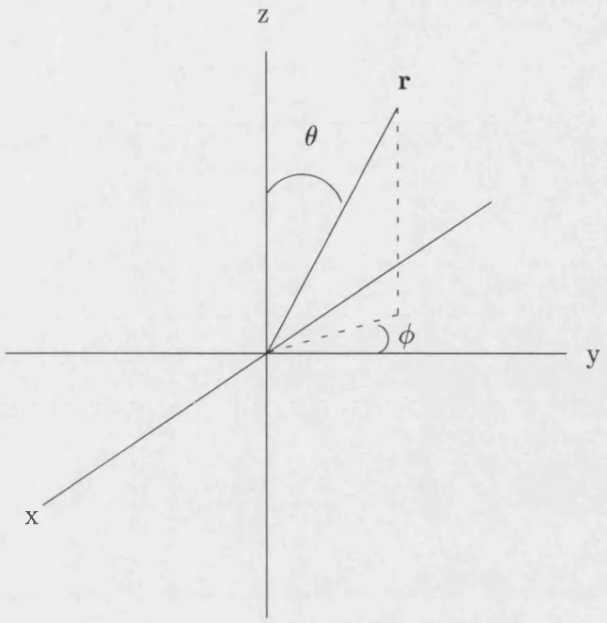

Figure 4.6: Definition of ϕ and θ for atomic states.

with n being the principle quantum number (equal to one here). u_{2p1} is given by,

$$u_{2p1} = \frac{1}{8\sqrt{\pi}} \exp(i\phi) \sin(\theta) \left(\frac{Z}{a_0}\right)^{\frac{3}{2}} \exp\left(\frac{-\rho}{2}\right)$$

where ϕ is the angle $\mathbf{r}$ makes with the x-y plane and θ is the angle $\mathbf{r}$ makes with the z axis as shown in figure 4.6. $\sin\theta$ can therefore be written as R/r, leaving the integral in equation 4.42 as,

$$F(\mathbf{q}) = \frac{1}{8\pi} \left(\frac{Z}{a_0}\right)^4 \int \mathrm{d}\mathbf{r}\, R \exp(-i\mathbf{q}.\mathbf{r}) \exp(i\phi) \exp\left(\frac{-3Zr}{2a_0}\right)$$

Splitting the integral into x-y ($\mathbf{R}$) and z components gives,

$$\begin{aligned} F(\mathbf{q}) &= \frac{1}{8\pi} \left(\frac{Z}{a_0}\right)^4 \int_{-\infty}^{\infty} \mathrm{d}z \, \exp(-iq_z z) \\ &\times \int_0^{\infty} R\mathrm{d}\mathbf{R} \, \exp(i\phi) \, \exp(-i\mathbf{Q}.\mathbf{R}) \exp\left(\frac{-3Z}{2a_0}(R^2+z^2)^{\frac{1}{2}}\right). \quad (4.43) \end{aligned}$$

If $q_z z$ is small enough $\exp(-iq_z z)$ can be simplified to $1 - iq_z z$ i.e. the dipole

approximation can be made. Let us consider if this is a good approximation here. z can clearly take any value but the approximation need only be valid while the integrand of $\mathbf{R}$ has a significant value, therefore, the dipole approximation need not hold when,

$$\exp\left(\frac{-3Z}{2a_0}(R^2+z^2)^{\frac{1}{2}}\right) \sim 0.$$

An extreme case might be when this term is considered insignificant only when it falls to e^{-15}. The maximum value of z, which is given when $\mathbf{r}$ is entirely in the z direction i.e. $\mathbf{R}$=0, is then given by,

$$\exp(\frac{-3Z}{2a_0}z) = \exp(-15) \tag{4.44}$$

and for an atomic number, Z, of 10 (the largest we consider in this work),

$$z = \frac{15 \times 2a_0}{3Z} = 0.529\text{Å}. \tag{4.45}$$

The corresponding value of q_z is 0.7482Å^{-1} since $q_z \sim k\theta_E$, where $k \sim 250\text{Å}^{-2}$ at 200keV and $\theta_E = 2.99 \times 10^{-3}$. This results in a true value of $\exp(-iq_z z)$ of $0.923 - i0.386$ as compared with the approximate value $1 - i0.396$, smaller atomic numbers will tend to increase this accuracy further. Thus the dipole approximation seems to be a good one to make here, it is investigated further in section 5.1.1.

Including this approximation in the integral and splitting the $\mathbf{R}$ integral into two components gives,

$$\begin{aligned} F(\mathbf{q}) &= \frac{1}{8\pi}\left(\frac{Z}{a_0}\right)^4 \int_{-\infty}^{\infty} \mathrm{d}z \int_0^{\infty} R^2 \mathrm{d}R \exp(\frac{-3Z}{2a_0}(R^2+z^2)^{\frac{1}{2}}) \\ &\times \int_0^{2\pi} \mathrm{d}\phi \, \exp(i|\mathbf{Q}||\mathbf{R}|\cos(\phi-\phi_Q)\exp(i\phi). \end{aligned} \tag{4.46}$$

The above integral does not contain the $q_z z$ term from the expansion of $\exp(-iq_z z)$ since it would leave an integration of an odd function and therefore give a zero contribution. The additional term ϕ_Q arises since, in general, the x-y scattering angle will not be identical to the angle **r** makes in the x-y plane so the angle between **Q** and **R** is given by $\phi - \phi_Q$, see section 4.2.2 and figure 4.4 for a similar example.

Making a substitution similar to that in section 4.2.2 allows $F(\mathbf{q})$ to be simplified using the standard integral given in equation (4.28), so that,

$$F(\mathbf{q}) = \frac{i}{4}\left(\frac{Z}{a_0}\right)^4 \exp(i\phi_Q)\int_0^\infty R^2 \mathrm{d}R J_1(QR)\int_{-\infty}^{\infty}\mathrm{d}z\,\exp(\frac{-3Z}{2a_0}(R^2+z^2)^{\frac{1}{2}}) \quad (4.47)$$

If the integral over z is changed to range from R to ∞ so that the integral over z (I_z say) is,

$$I_z = 2\int_R^\infty \mathrm{d}y\; y(y^2-R^2)^{-\frac{1}{2}}\exp(\frac{3Z}{2a_0}y)$$

then this is in a standard form [91] and $F(\mathbf{q})$ is given by,

$$F(\mathbf{q}) = \frac{i\exp(i\phi_Q)}{2}\left(\frac{Z}{a_0}\right)^4\int_0^\infty \mathrm{d}R\, J_1(QR)R^3K_1\left(\frac{3RZ}{2a_0}\right). \quad (4.48)$$

K_1 is the second order modified Bessel function and can be found in mathematical tables [87] or computer libraries [39]. The value for this integral can now be found numerically without difficulty, however if the integral is made dimensionless it will be possible to produce a look up table which is valid for all values of Z. Making the substitution $\tilde{Q} = Qa_0/Z$ and $x = RZ/a_0$ gives,

$$F(\mathbf{q}) = \frac{i}{2}\exp(i\phi_Q)\int_0^\infty \mathrm{d}x\, x^3 J_1(\tilde{Q}x)K_1(3x/2). \quad (4.49)$$

$1s, 2p_{\pm 1}$	$\frac{i}{4}\exp(\pm i\phi_Q)\int_0^\infty \mathrm{d}x\, x^3 J_1(\tilde{Q}x)K_1\left(\frac{3}{2}x\right)$
$1s, 2p_0$	$\frac{i\sqrt{2}}{3}\frac{q_z a_0}{Z}\int_0^\infty \mathrm{d}x\, x^3 J_0(\tilde{Q}x)K_2(3x/2)$
$2p_0, 3d_0$	$\frac{2i}{135\sqrt{3\pi}}\frac{q_z a_0}{Z}\left\{\frac{18\pi}{5}\int_0^\infty \mathrm{d}x\, x^4 J_0(\tilde{Q}x)K_3\left(\frac{5x}{6}\right) - \frac{i\pi}{2}\int_0^\infty \mathrm{d}x\, x^5 J_0(\tilde{Q}x)K_2\left(\frac{5x}{6}\right)\right\}$
$2p_0, 3d_1$	$\frac{i\sqrt{2}}{135}\exp(i\phi_Q)\int_0^\infty \mathrm{d}x\, x^4 J_1(\tilde{Q}x)K_2\left(\frac{5x}{6}\right)$
$2p_1, 3d_0$	$\frac{1}{72\sqrt{6}}\exp(i\phi_Q)i\left\{\frac{12}{5}\int_0^\infty \mathrm{d}x\, x^4 J_1(\tilde{Q}x)K_2\left(\frac{5x}{6}\right) - \int_0^\infty \mathrm{d}x\, x^5 J_1(\tilde{Q}x)K_1\left(\frac{5x}{6}\right)\right\}$
$2p_1, 3d_1$	$\frac{2i}{135}\frac{q_z a_0}{Z}\int_0^\infty \mathrm{d}x\, x^5 J_2(\tilde{Q}x)K_2\left(\frac{5x}{6}\right)$
$2p_1, 3d_{-1}$	$\frac{i}{135}\frac{q_z a_0}{Z}\int_0^\infty \mathrm{d}x\, x^5 J_0(\tilde{Q}x)K_2\left(\frac{5x}{6}\right)$
$2p_1, 3d_2$	$\frac{i}{324}\exp(i\phi_Q)\int_0^\infty \mathrm{d}x\, x^5 J_1(\tilde{Q}x)K_1\left(\frac{5x}{6}\right)$
$2p_0, 3d_2$	$\frac{i}{135\sqrt{2}}\exp(-i2\phi_Q)i\frac{q_z a_0}{Z}\int_0^\infty \mathrm{d}x\, x^5 J_2(\tilde{Q}x)K_2\left(\frac{5x}{6}\right)$
$2p_1, 3d_{-2}$	$\frac{-i}{324}\exp(i3\phi_Q)\int_0^\infty \mathrm{d}x\, x^5 J_3(\tilde{Q}x)K_1\left(\frac{5x}{6}\right)$

Table 4.1: Expressions for $F(\mathbf{q}, Z)$ for a fast electron having caused a transition from the $1s$ to $2p$ or $2p$ to $3d$ states.

Similarly, expressions can be found for the other 1s to 2p transitions and the 2p to 3d transitions (K and L edges). These are listed in table 4.1 without derivation.

4.4 Computer Implementation

The mathematical models of the systems we have been discussing are implemented using a set of Fortran routines. These were written from scratch except for the Numerical Algorithms Group (NAG) routines and the calculation of the Bloch waves which uses an adapted form of the CBED pattern matching code used in chapter 3.

The form of the codes is described using the flow charts in figures 4.7, 4.8, 4.9 and 4.10. The free space model was simple to code since the incident wave is simply a plane wave and the resulting image is circularly symmetric. However,

the crystal model was much more difficult to code since the incident and scattered waves can undergo elastic scattering by the crystal, resulting in the breakdown of circular symmetry.

The exact diffraction conditions used in the crystal model are described as well as the method of focusing the object function. Additionally the method of investigating some of the approximations made during this chapter are described.

4.4.1 Calculating F(q)

In the free space and crystal model equations (4.29) and (4.41) have to be calculated respectively. In both cases the value for $F(\mathbf{Q})$ is required and the time taken to calculate this number can be large. In general this value is a function of atomic number, Z, but as described in section 4.3.1 it can be made into a dimensionless quantity. In this case it is possible to calculate this function once and put it into a look up table for future reference, saving calculation time. This was done for each of the $1s$ to $2p$ and $2p$ to $3d$ transitions,see figure 4.7. In each case $\tilde{Q}$ was calculated at 1000 evenly spaced points between 0 and 10 where it was assumed to be no longer significant, see section 5.1.3. A NAG routine [39] is used to perform the necessary integral, with a second NAG routine being used to return the necessary values of the Bessel functions. The Final value of $F(\tilde{Q})$ was then written to a file for future reference. Calculation of the image intensity requires $F(\tilde{Q})$ to be know at any point which rather than predefined discrete values, so an interpolation method is used to provide the values not calculated [92].

4.4.2 Free Space Model

Let us first consider the implementation of the free space model. A separate code was developed for each transition since it can be seen from table 4.1 that there are significant differences between each of the expressions for image intensity.

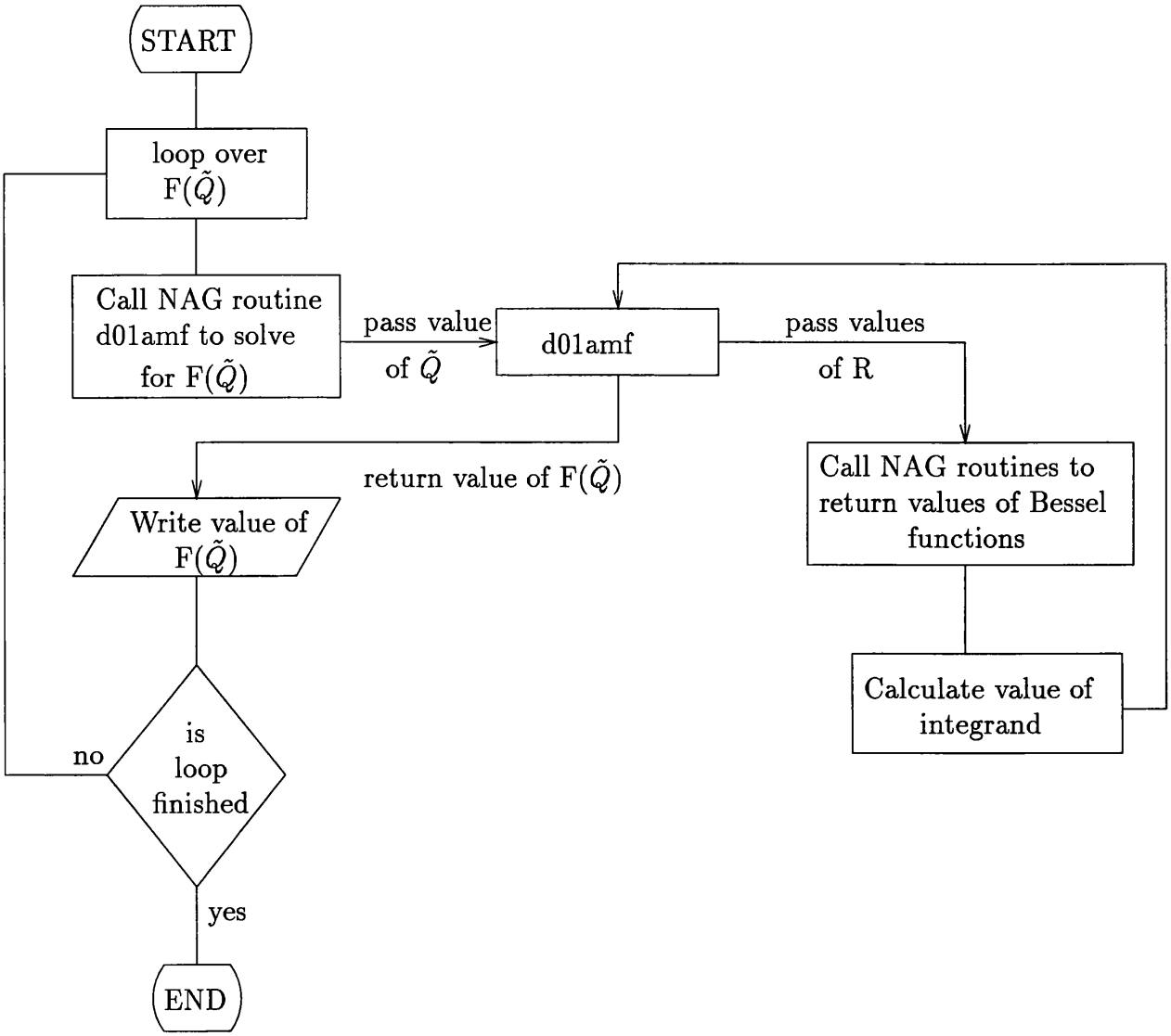

Figure 4.7: Flow chart of the code to calculate F($\tilde{Q}$).

However, they all followed the same pattern as figure 4.8. First, the constants were set and the 1000 dimensionless values of $F(\tilde{Q})$ were input. Next a loop was set up to range over the spatial region of interest, e.g. if the object function was to be determined over 5Å a loop was set up to run from 0 to 5 in steps of 0.05, giving 100 intensity points. Because in the free space case the object function is circularly symmetric it was only necessary to calculate the intensities from the centre of the object function along a single straight line. The results were then displayed as a line graph as shown in section 5.1.

A NAG routine [39] was then called to calculate the value of the integral in equation (4.29) at the spatial position under consideration. This NAG routine required a user subroutine to provide a value of the integrand at any point. This user routine took the table of 1000 points of $F(\tilde{Q})$ described above. Further NAG routines were called to provide the values of the Bessel functions at the points under consideration [39]. The value of the integral was passed back from the NAG routine to the main programme and the intensity value of equation (4.29) was calculated and stored in a file.

A number of approximations can be considered using this model with only a minimum of changes to the code necessary to consider the effects. These approximations are:

- non relativistic $\mathbf{k}$
- constant q_z
- dipole approximation
- varying objective aperture

The first two approximations have not been discussed previously. q_z is given by,

$$q_z = |\mathbf{k}| - |\mathbf{k}'| + \frac{Q^2}{2k'}. \tag{4.50}$$

In the non relativistic case $|\mathbf{k}| - |\mathbf{k}'|$ is given by $k\Theta_E$ where $\Theta_E = \Delta E/E$ whereas the correct relativistic expression is $\Theta_E = \Delta E/(E+m_oc^2)(v/c)^2$. Θ_E is defined at the start of the code and can easily be changed to investigate this approximation.

If q_z is kept constant then it is given by $q_z = |\mathbf{k}| - |\mathbf{k}'|$, which is nearly true for small values of $\mathbf{Q}$. If this approximation is made then q_z only needs to be defined once at the start of the code. The correct definition requires q_z to be calculated each time the integrand is evaluated. Although this increases CPU time, it is easily implemented and doing so allows the approximation to be tested.

To test the dipole approximation the function $F(\mathbf{q})$ had to be recalculated using the expression given in equation (4.43) rather than equation (4.48), this initial calculation took longer due to the additional integration over z but did not affect the speed of the final calculation of the object function.

Finally, the size of the objective aperture can be varied simply by altering the range over which the NAG routine calculates the value of the integral in equation (4.29). This is easily achieved by altering one parameter at the beginning of the code.

All of these approximations are considered in section 5.1.1 where it is shown that the dipole approximation is valid but that the non relativistic and constant q_z object function are slightly different from the full calculation. The coding for the crystal object function took this into account and neither of these approximations were used.

4.4.3 Crystal Model

The coding for the crystal object function was more complicated than the free space case. The values for $F(\mathbf{q})$ remained the same as did the subroutine to return the value of $F(\mathbf{q})$. However, the rest of the code was different. The circular symmetry of the object function no longer holds so a one dimensional

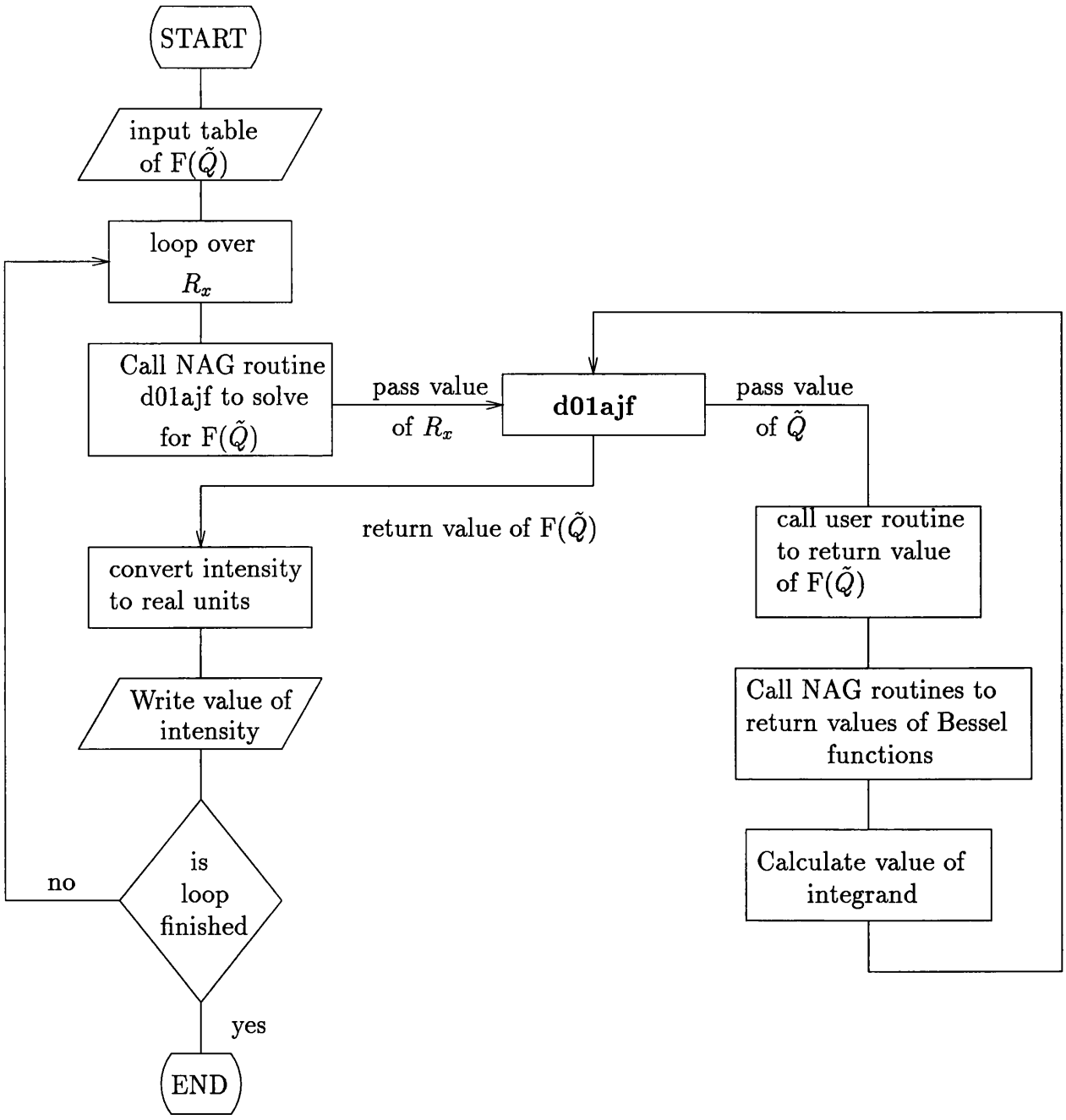

Figure 4.8: Flow chart of free space intensity programme.

representation of the intensity is no longer valid.

The intensity at a point $\mathbf{R}, t$ is now given by the modulus squared of equation (4.40), which is the Fourier transform of the diffracted amplitudes given in equation (4.41). The new code now calculates these diffraction amplitudes and stores them as a data file, a separate programme is used to perform the Fourier transform and either display the intensity pattern on the screen as an intensity picture, see chapter 5 for examples of this format, or as another data file.

There are three stages to the calculation of the diffraction amplitudes see figure 4.9. First, the host crystal is defined including the position and type of element as well as the source atom type, position and atomic number. Two loops over the scattered directions are set up, i.e. K'_x and K'_y are varied between -8 and +8 Bragg angles with 256 points in between, making a total of 65536 points to be calculated. A second routine is then called to calculate the value of the diffraction amplitude at each point.

For the work presented in this thesis we have chosen a Si crystal of 500Å thickness. At this thickness there will be very limited absorption and so the Doyle and Turner potential [5] is used. This is not an accurate potential for a crystal structure (see chapter 3) but it will not introduce any qualitative errors into the calculation. The accelerating voltage of the microscope is set to 200keV.

The diffraction amplitudes of equation (4.41) include all zero layer $\mathbf{G}$ vectors potentially making the calculation very large. However, the diffraction conditions can be chosen so that only a systematic row is included, this means that less calculations are needed than if a zone axis was chosen. If this is the case then the eigenvectors are independent of K'_y (for a systematic row along $\mathbf{G}_x$) and the eigenvalues are given by,

$$s^{j'}(\mathbf{K}') = s^{j'}(K'_x) + K'^2_y. \tag{4.51}$$

In this case $A(\mathbf{K}')$ is given by,

$$A(\mathbf{K}') = \sum_{jj'G_xG_x'} C_0^{j'}(K_x')C_{G_x'}^{j'*}(K_x')C_0^{j*}(0)C_{G_x}^{j}(0)$$
$$\times \exp(-i(s^{j'}(K_x') + K_y'^2)z/2k)\frac{\exp(-i\mathbf{q}.\mathbf{r}_0)}{q^2}F(\mathbf{q}) \qquad (4.52)$$

remembering that the incident direction is always perpendicular to the surface of the crystal, i.e. $\mathbf{K}$=0. $\mathbf{q}$ is now defined by,

$$\begin{aligned} Q_x &= K_x' - G_x + G_x' \\ Q_y &= K_y' \\ q_z &= ((s^j(K_0) - s^{j'}(K_x') - K_y'^2)/2k) - (k - k'). \end{aligned} \qquad (4.53)$$

For all the calculations done with this model the Si $(\bar{2}20)$ systematic row has been used with the 7 strongest reflections, i.e. $\bar{6}60$ to $6\bar{6}0$, evaluated in the sum over G.

Thus each of the sums in equation (4.41) is over a total of seven values, the eigenvalues and eigenvectors are calculated by calling an adapted form of the CBED programme used in chapter 3. $F(\tilde{Q})$ is found from the same routine used in the free space case and the final value of the diffracted wave amplitude is returned to the original programme where it is saved to file.

In the independent atom model it was stated that the term $\exp(-iQ^2z/2k)$ from equation (4.24) would tend to defocus the image. In this case the focusing of the object function could be achieved simply by imaging the source atom immediately below itself where $z \sim 0$ and this term then reduces to 1. However, in the case of a source atom within a surrounding crystal this is no longer possible, the closest that the object function can be measured is at the bottom surface of the crystal. In this case it is necessary to add a focusing term to the expression in equation (4.41). The diffraction amplitudes were saved in a separate data file so that the effect of the focusing term could be studied without having to recalculate the whole image. The focus was introduced by multiplying the diffracted wave

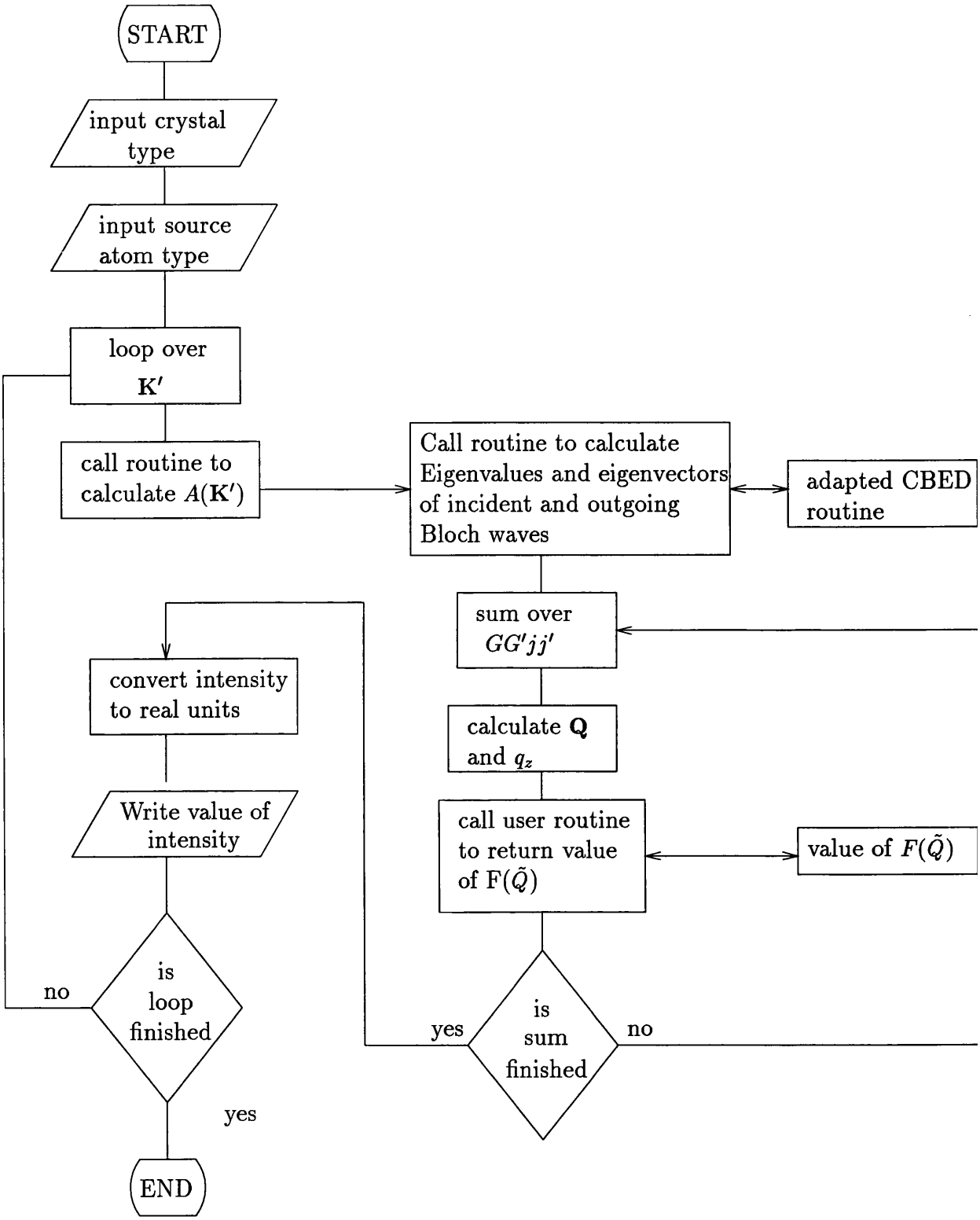

Figure 4.9: Flow chart describing calculation of inelastic amplitudes measured at the base of the crystal.

amplitudes by

$$\exp(ik'^2(t - z0)/2k) \tag{4.54}$$

where z0 is the depth of the impurity atom below the top of the crystal. This was done in the Fourier transform programme.

The Fourier transform programme see figure 4.10, input the name of the diffracted wave amplitude file to be used, the position of the focus and output a 256 by 256 picture of intensity values ranging from 0 (black) to 255 (white) as shown in chapter 5. In order to emphasise the less intense details of the images a gamma factor [93] of 2.0 has been used in the pictures shown in chapter 5 except where stated. For the $1s$ to $2p_{\pm}1$ case the transition can be split into separate x and y states. Table 4.1 showed that the only difference between the $1s$ to $2p_1$ and $1s$ to $2p_{-1}$ transitions is the sign on the phase term, therefore, the $1s$ to $2p_x$ and $2p_y$ transitions are given by adding and subtracting the amplitudes $A(\mathbf{K}')_{2p_1}$ and $A(\mathbf{K}')_{2p_{-1}}$ respectively with a normalisation term of $1/\sqrt{2}$. For the pictures shown here this normalisation term is not important since absolute values are not being considered.

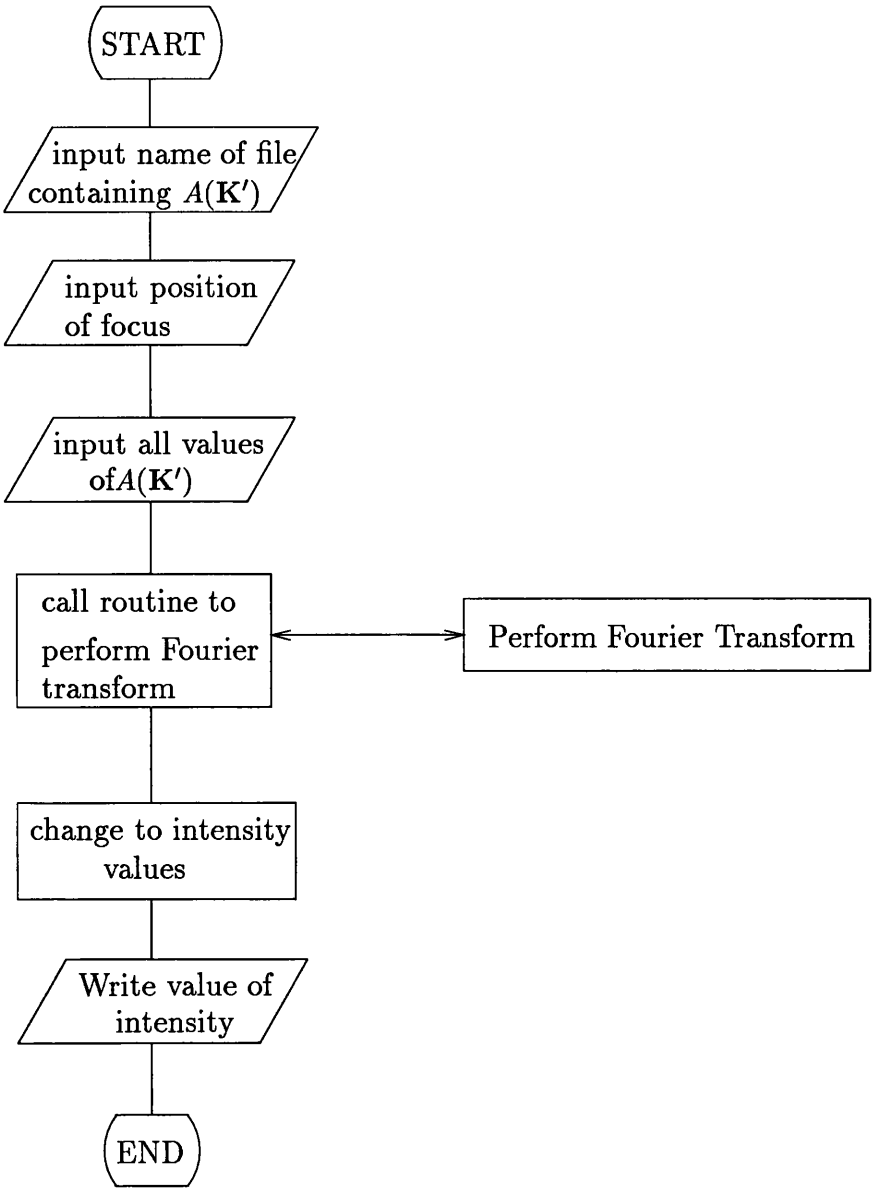

Figure 4.10: Flow chart describing conversion of $A(\mathbf{K}')$ to intensity values.

4.5 Summary

The use of energy filtering to investigate the atomic composition of materials has been discussed. The limitations on the resolution of these chemical maps such as signal to noise ratio and chromatic aberrations have been described. In order to investigate the limitations imposed by the surrounding crystal, i.e. the effects

of dynamical diffraction, a model for investigating the inelastic scattering of fast electrons due to atomic excitation has been developed. To keep the calculations as general and simple as possible a number of simplifications have been used.

The source atom where the atomic transition takes place has been taken to be hydrogenic and the atomic electron has been assumed to be excited from one bound state to another rather than from a core state into a conduction band state. These approximations to the true physical processes allow a simple and versatile analytic expression to be derived for the inelastic wave function which can give good qualitative information on spatial localisation.

The starting point for the analysis of the effects of dynamical diffraction is a system where no elastic diffraction is present. The object function for such a system has been derived and is given in equation (4.29). The inclusion of a surrounding crystal requires the fast electron to be described in terms of Bloch waves while in the crystal. However, it is assumed that the source atom does not alter the crystal structure in anyway, it merely acts as a source for the inelastic event.

The inelastic wave function is derived and the final expression is given in equation (4.37). The calculation of the final object function was considerably simplified by using a Fourier transform, equation (4.40). The diffraction amplitudes are then defined in equation (4.41). The position of the source atom can be changed easily which will allow investigation into the effects of dynamical diffraction in the next chapter.

Both the free space model and the crystal model required the function $F(\mathbf{q})$ to be known. This is different for each transition and so only the $1s$ to $2p_z$ transition was derived. The final expression for this transition is given in equation (4.49) while the other expressions for the $1s$ to $2p$ and $2p$ to $3d$ transitions are given in table (4.1) without derivation.

The Computer implementation of these models has been described. The diffrac-

tion conditions for the crystal model were chosen as a systematic row for ease of calculation. The focus of the free space model was achieved by imaging immediately below the source atom, whereas for the crystal model a focusing term, given in equation 4.54 was needed.

These models can now be used to study the underlying physical limits to the resolution of chemical mapping using imaging PEELS.

Chapter 5

Inelastic Diffraction and Imaging Results

Both the free space and crystal models have now been developed and we are in a position to begin studying their object functions. In section 5.1 we will consider the free space object functions, their shape and spatial extent will be examined. Some of the approximations made when creating the model will be investigated to ensure there is no significant effect upon the object functions. In particular, we will consider relativistic effects, the dipole approximation, constant q_z and how a realistic collection aperture of $\sim 10 - 20$ mrads affects the final function.

In section 5.2 the inclusion of a surrounding crystal will be considered. Comparisons are made between the free space object functions and the crystal object function, showing the effects of dynamical diffraction. However, the source atom in a crystal can be moved through the crystal either through depth or across the x-y plane, i.e. parallel to the surface of the crystal. In section 5.3 we show that moving the source atom from on plane to between planes results in a different object function, indicating that the interaction between a fast electron and a source atom is to some extent localised to within a lattice spacing. Later in this section we show that moving the source atom through the depth of the crystal

results in large variations in intensity. This is accounted for by considering the intensity of the Bloch waves at each depth which correlates to the intensity of the final object function. Fringe reversal is also observed as the depth of the source atom is changed. It is shown that this is a result of changing the focus, choosing a single focus prevents reversal. A single focus is also shown to reduce the variation in the intensity especially if carefully chosen.

In section 5.4 we consider a single column of source atoms, it is seen that in this case intensity variations are less important due to the averaging effect of integrating through the whole column. However, it is also demonstrated that these columns must be some distance apart to be able to resolve them. This is due to fringes from nearby columns adding to make it seem as if there is a column even when none is present.

5.1 Single Atom Object Functions

Despite considering only the $1s$ to $2p$ and $2p$ to $3d$ transitions presenting all these transitions would result in an excessive number of results. Consequently only the $1s$ to $2p_z$, the $1s$ to $2p_{xy}$ and the $2p_z$ to $3d_1$ transition are considered. These transitions were chosen as representative of all the possible transitions, the $2p_z$ being an even state with respect to the incident direction of the fast electron, $\hat{z}$, and the $2p_{xy}$ being an odd state. The $2p_z$ to $3d_1$ transition is only considered in section 5.1 where it is demonstrated that it has many similarities to the s to p transitions.

5.1.1 Validation of Approximations

In the last chapter a number of approximations were made when creating the model. Here we will consider four approximations. First, although the dipole ap-

label	constant q_z	no relativistic correction	dipole approximation
constant q_z	Y	Y	Y
non relativistic	N	Y	Y
relativistic	N	N	Y
no dipole approx	N	N	N

Table 5.1: Table explaining the use of labels when considering the validity of approximations.

proximation has been investigated in similar work [9] and briefly in section 4.3.1 it is important to demonstrate that this approximation is valid. Second, it was unclear how important relativistic effects described in section 4.4 would prove, these are investigated. Third, using a constant value of q_z as described in section 4.4 will reduce the calculation time but may affect the accuracy of the results. Finally, using the object function implies that all the significant diffracted beams are used when creating an image, this is never the case and the difference that a finite collection angle makes needs to be understood.

Initially only the relativistic, dipole and constant q_z approximations are tested, the collection angle is considered later. Figure 5.1 shows the differences between these approximations for the $1s$ to $2p_z$ transition at $Z = 5$. Table 5.1 explains the labelling system for each plot, e.g. the label 'relativistic' has a varying value of q_z, uses the relativistic correction factor but makes the dipole approximation.

It can be seen that there is is no significant difference between the results obtained from using the dipole approximation and those which calculate $\exp(-iq_z z)$ (from equation(4.43)) exactly. There are some differences between these results and those calculated without a relativistic correction factor although even here the results are qualitatively very similar, reaching half maximum intensity at approximately the same distance of 0.35Å. However, using a constant value of q_z significantly reduces the maximum intensity and half maximum is not reached

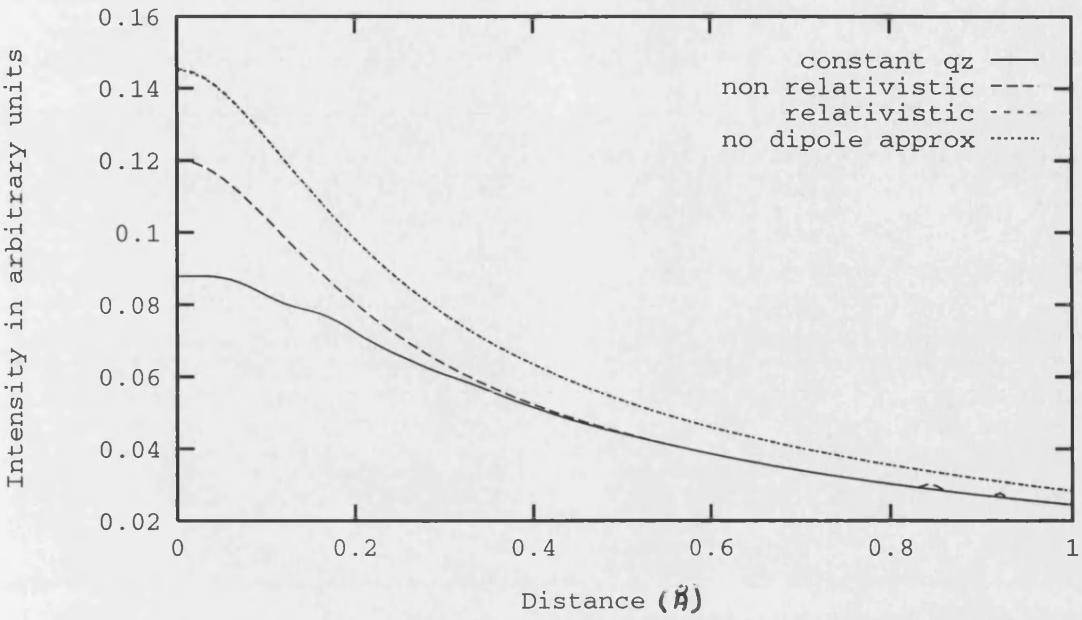

Figure 5.1: Comparisons of object function obtained with different approximations. The transition is the $1s$ to $2p_z$ at energy loss 250eV. See text for details.

until nearly 0.6Å.

Figure 5.2 show the same plots for a much higher energy loss of 1000eV with the same transition. Again the differences between the object functions calculated using the dipole approximation and exact $\exp(-iq_z z)$ are very small. The calculation without the relativistic correction again gives some small differences with the constant q_z being the most inaccurate approximation. Because of the differences already shown by using a constant value of q_z this approximation is not used elsewhere in this work.

Figure 5.3 shows the remaining approximations but for the $2p_z$ to $3d_1$ transition at $Z = 12$, i.e. an energy loss of 260eV. This time the only noticeable difference in the approximations is that the object function calculated without making the dipole approximation has a slightly lower maximum intensity than for the other approximations. However, the radial spread of the object function remains the same whatever approximations are used.

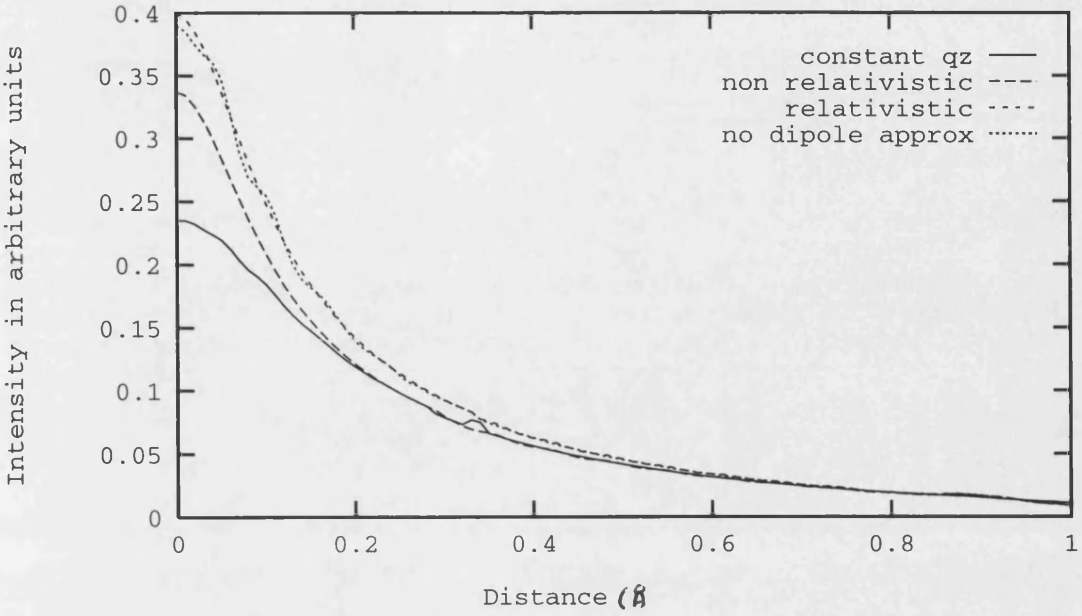

Figure 5.2: Comparisons of object function obtained with different approximations. The transition is the $1s$ to $2p_z$ at energy loss 1000eV. See text for details.

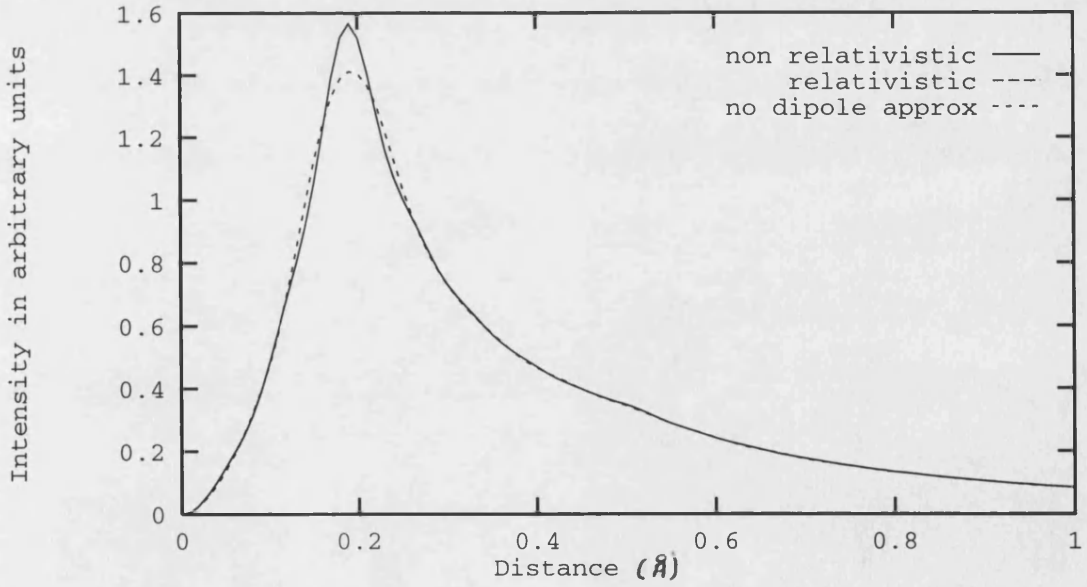

Figure 5.3: Comparisons of object function obtained with different approximations. The transition is the $2p_z$ to $3d_1$ at energy loss 260eV. See text for details.

Since the inclusion of the relativistic correction makes some differences to the object functions this correction is used in the rest of the work presented here. However, the change in the object function is only slight if the dipole approximation is used. Therefore, since calculation time is significantly reduced by using this approximation, it is implemented throughout the rest of this work. Before considering the effect of the collection aperture let us first examine what information we can obtain from the object function itself.

5.1.2 Resolution of Object Functions

While we have shown that the above approximations are valid we must remember that our models are not intended to give an exact representation of the real world. However, it is still possible to get a qualitative understanding of the size and shape of the object functions from these models, this is done for the free space model in this section.

Let us first consider the object functions of the $1s$ to $2p_z$ transition. Figure 5.4 shows the object functions for atomic number, Z, of 4,5,7 and 10 which correspond to energy losses of approximately 160eV, 250eV, 500eV and 1000eV respectively.

An interesting feature in this graph is the sharper fall off in intensity at higher energy losses. This clearly shows that, as might be expected, higher energy losses lead to more localised object functions. At the highest energy loss ($Z = 10$) the object function has fallen well below half maximum by 0.3Å, giving an overall half maximum spread of less than 0.6Å. However, even at low energy losses ($Z = 4, \Delta E = 160$eV) the intensity has fallen to half maximum by $\sim$ 1Å giving an overall half maximum spread of $\sim$ 2Å. If these levels of spread were repeated within a crystal it is likely that adjacent atoms could be resolved.

We now compare these results to those for the $1s$ to $2p_{xy}$ shown in figure 5.5 which also has atomic numbers of 4,5,7 and 10. It can be seen that the one

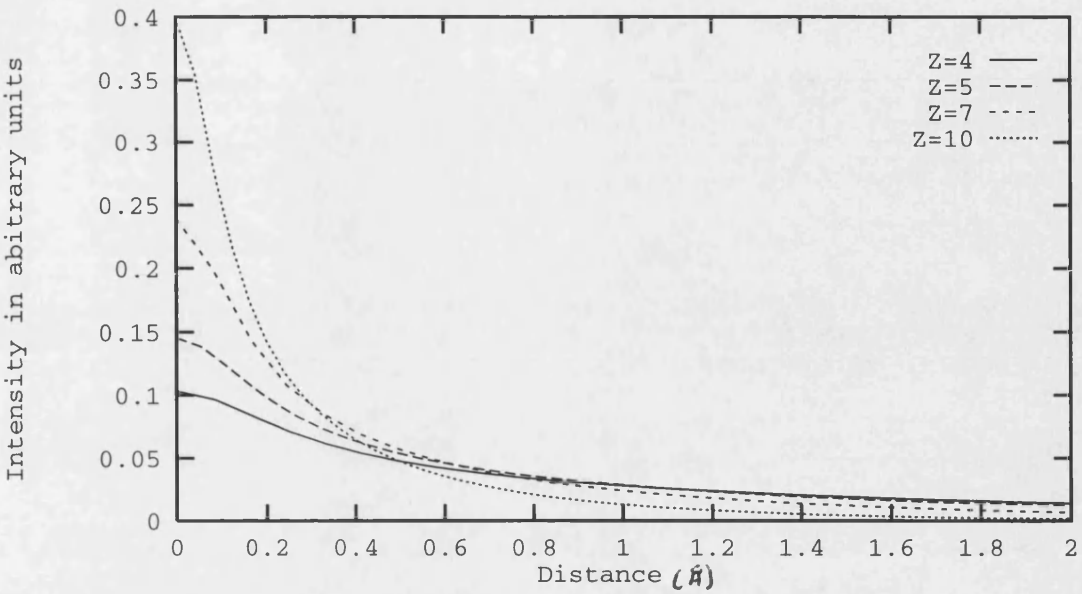

Figure 5.4: Object functions for various atomic numbers for the $1s$ to $2p_z$ transition, showing that higher energy losses lead to more localised object functions with higher maximum intensities.

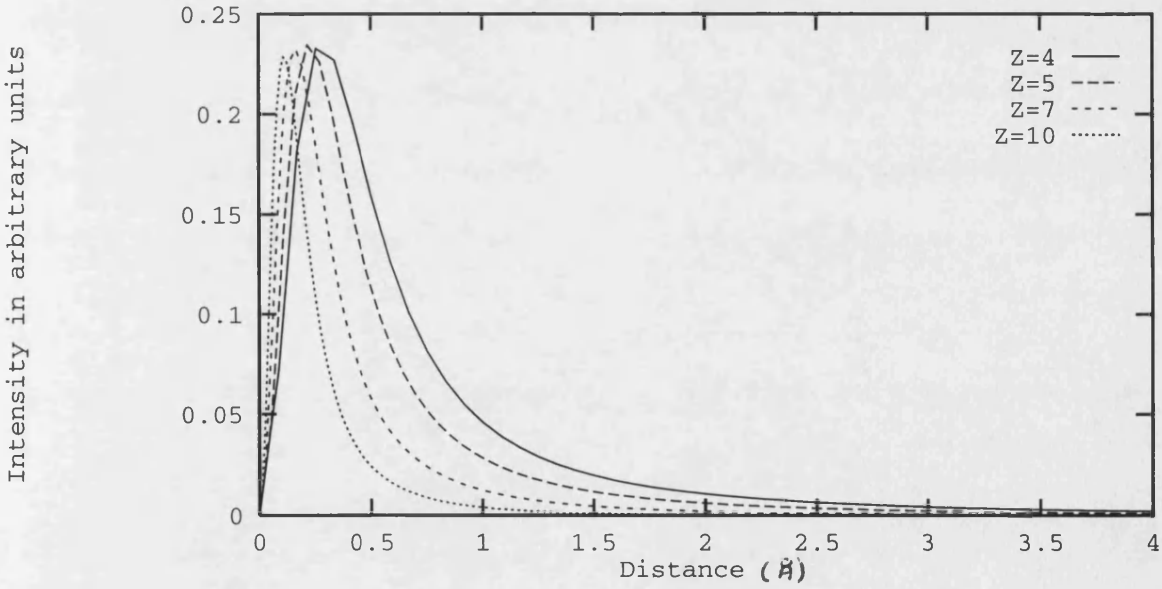

Figure 5.5: Object function for the $1s$ to $2p_{xy}$ transition at energy losses ranging from 160eV to 1000eV.

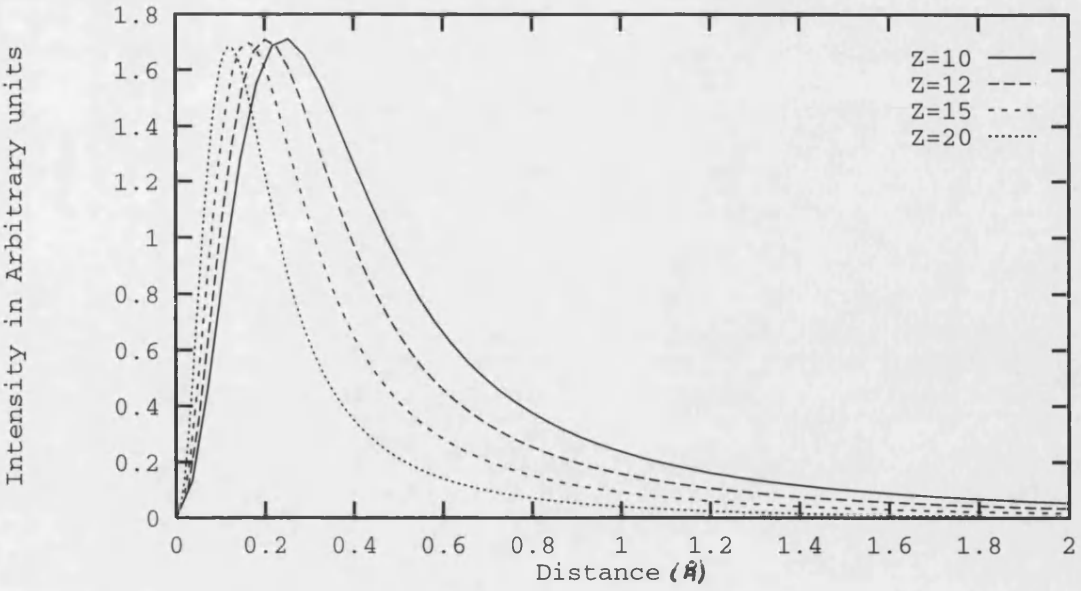

Figure 5.6: object function for the $2p$ to $3d$ transition at various energy losses, showing that at higher energy losses the object function becomes more localised.

major difference is that the intensity falls to zero at the centre of the image. This can be understood since the $2p_{xy}$ state is an odd function. Again the increased localisation of the object functions at higher energy loss is demonstrated, although this time there is no variation in maximum intensity, equation (4.40) is not a function of atomic number here. All object functions fall to below half maximum within 1Å, indicating that it may be possible to resolve adjacent atoms using these transitions in a real crystal.

Consider now the $2p_z$ to $3d_1$ transition with atomic numbers 10,12,15 and 20 with energy losses of 190eV, 260eV, 430eV and 750eV as shown in figure 5.6. The plots are very similar to those of the $1s$ to $2p_{xy}$ transition, again the intensity can be seen to drop off to zero at the centre. Even for low energy losses half maximum spread will be less than 1.5Å.

5.1.3 Effect of Varying the Collection Aperture

We have seen in the last section that the object functions for an atom in free space are well localised even at relatively low energy losses. However, the assumption that all diffracted waves will be collected is unrealistic, typically the objective aperture is 10 - 20 mrads [94]. The object function is given in the limit that the change in $F(\mathbf{Q})$ from equation (4.42) tends to zero as $\mathbf{Q}$ gets large. Noting that we have previously defined $\tilde{Q} = Qa_o/Z$ then for the $1s$ to $2p_z$, $1s$ to $2p_{xy}$ and $2p_z$ to $3d_1$ transitions the value of $F(\tilde{Q})$ is plotted against $\tilde{Q}$ in figure 5.7. It can be seen that by $\tilde{Q} = 8$ the value of $F(\tilde{Q})$ is less than 1% of the maximum value of $F(\tilde{Q})$ even for the $1s$ to $2p_{xy}$ transition.

Therefore, when calculating the true object function it is only necessary to use values of $\tilde{Q}$ up to this point. However, it should be noted that for an electron microscope voltage of 200keV this corresponds to a large collection aperture. For example, if the atomic number is 4, then for $\tilde{Q} = 8$, $Q = 8 \times 4/a_0$. At an accelerating voltage of 200keV, $k = 250\text{Å}^{-1}$ and the collection angle is 240 mrads, see figure 5.8. For higher atomic numbers this gets larger, e.g. for Z=10 the collection angle is 600 mrads. The reduced collection angle under real experimental conditions will lead to differences between observation and the theoretical limits even if aberrations could be overcome. To quantify this figure 5.9 shows line graphs of the $1s$ to $2pz$ transition at $Z = 4$ with several values of collection angle.

It can be seen that the size of the collection aperture has an important effect on the spread of the object functions. For a collection angle of 23mrads the maximum intensity is reduced by only a small amount and the radial spread is increased slightly. However, when the collection angle is reduced to 8 mrads half maximum intensity is reached at about 2Å from the centre. This would make it more difficult to resolve adjacent atoms in a crystal.

In this section we have demonstrated a number of important points. First, we

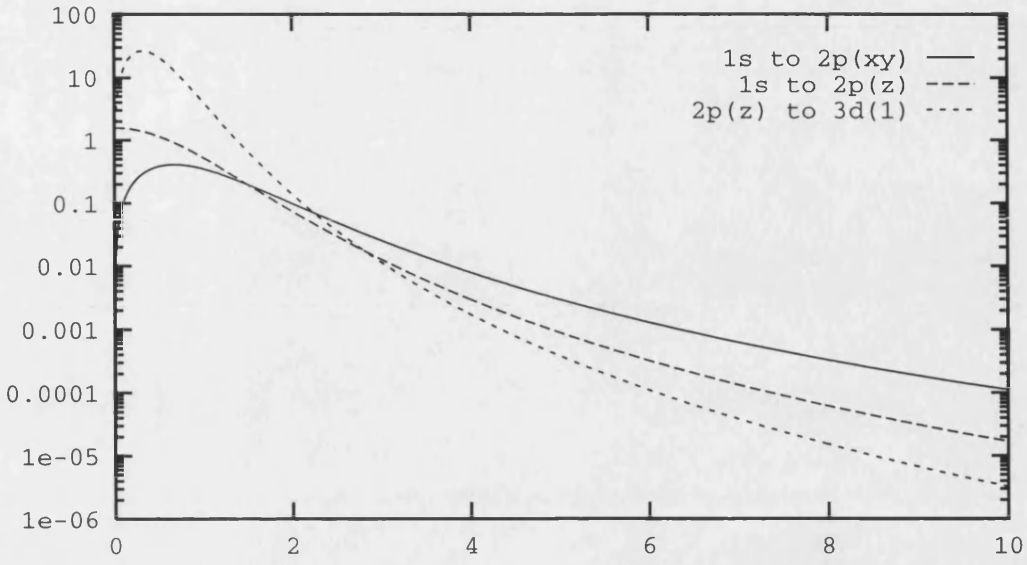

Figure 5.7: example of how $F(\tilde{Q})$ varies with $\tilde{Q}$.

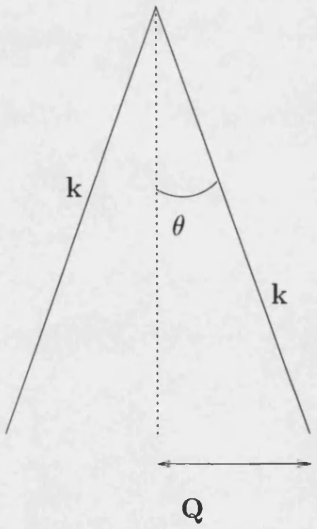

Figure 5.8: The collection angle θ is given by $|\mathbf{Q}|/|\mathbf{k}|$, see text for details.

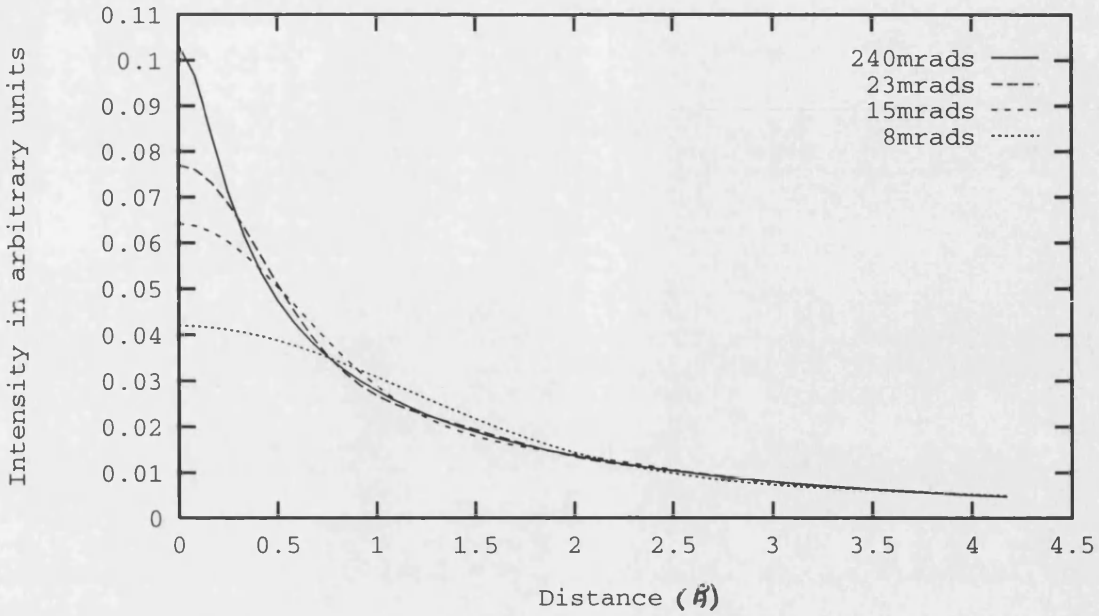

Figure 5.9: Various collection angles for the $1s$ to $2p_z$ transition at $Z = 4$, showing that smaller collection angles lead to greater spread.

have seen that the dipole approximation is valid for this model but that a varying q_z and a relativistic correction is required. The object functions found using this model have been shown to be well localised even for transitions with low energy loss. This indicates that atomic resolution may be possible. However, it has also been seen that the objective aperture size plays a role in the radial spread of the object function although, even with realistic aperture sizes of 20mrad, atomic resolution may be possible. We will now investigate the affect that dynamical diffraction has on the object functions and whether adjacent atoms within a crystal are resolvable.

5.2 Crystal Object Functions

5.2.1 Diffraction Conditions

The crystal in which the dynamical diffraction occurs has been chosen as Si with a thickness of 500Å. As explained earlier, the potential is treated as real since there will not be a significant amount of absorption at this thickness. Therefore, the crystal potential is assumed to be made up from the Doyle and Turner potential [5] which although not accurate for a crystal structure (see Chapter 3) will not introduce any qualitative errors into the calculation. The accelerating voltage has been set to 200 keV which is a typical value for both diffraction and imaging.

The diffraction amplitudes of equation (4.41) include all zero layer **G** vectors potentially making the calculation very large. However, the diffraction conditions can be chosen so that only a systematic row is included, this means that less calculations are needed than if a zone axis was chosen. The systematic row chosen was the Si $(\bar{2}20)$ with the 7 strongest reflections i.e. $\bar{6}60$ to $6\bar{6}0$ as described in section 4.4.

5.2.2 Comparison of Free Space and Crystal Object Functions

Inclusion of the surrounding crystal destroys the circular symmetry which was apparent in the free space model of section 5.1. Therefore, the line graph format for displaying intensity values is no longer as useful. The object functions will now be displayed in a 2 dimensional pictorial format where increased intensity is indicated by a whiter colour as discussed in section 4.4. This format has the additional advantage that it is similar to the images produced using a CTEM.

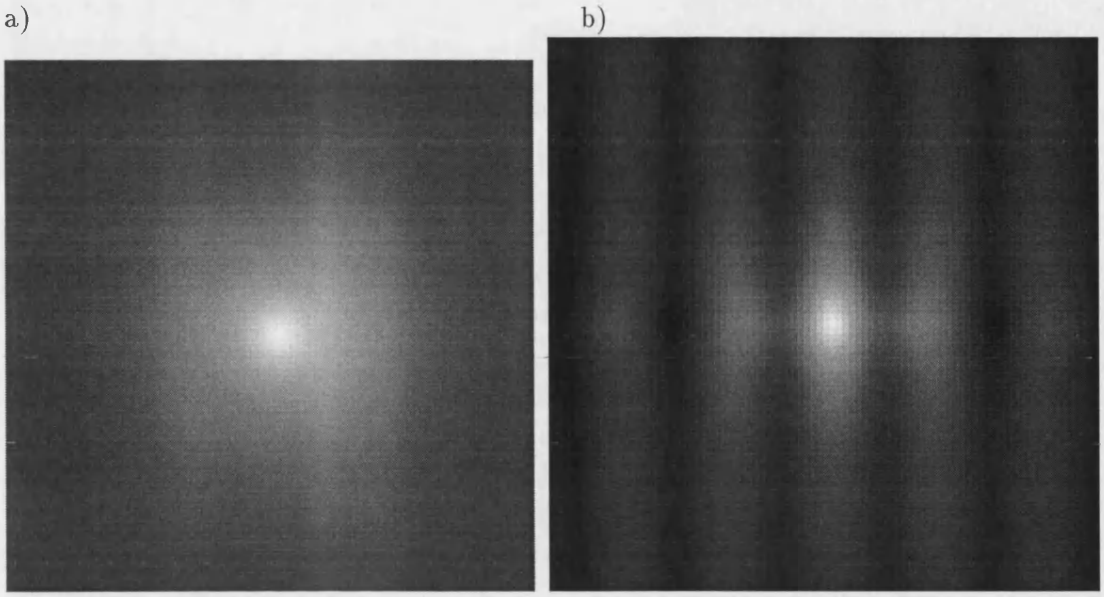

Figure 5.10: $1s$ to $2p_z$ transition at Z=4 and on a crystal plane.

With this new format we can compare the results from the $1s$ to $2p_z$ transition shown originally in figure 5.4. Figure 5.10 shows the 2 dimensional object function for the $1s$ to $2p_z$ transition at Z=4, a) is the free space function equivalent to figure 5.4 and b) is found from placing the source atom 150Å through a 500Å crystal and lying on a crystal plane. For both functions the focus of the microscope is exactly on the source atom. Thus the two functions are identical except that one source atom has a crystal of Si surrounding it, therefore all the differences must be due to the effects of dynamical diffraction from the surrounding crystal.

Both pictures have a bright spot at the centre indicating the position of the source atom, however, figure 5.4b also exhibits background fringes of atomic spacing which reveal the underlying lattice. This underlying lattice spacing is 1.92Å and gives the scale for the pictures shown here.

As described in section 4.4 the separate x and y states can be displayed using this 2 dimensional pictorial format. These are shown for both the free space and crystal conditions in figure 5.11 for atomic number 4. Again the central bright spot corresponding to the position of the source atom can be seen with, in the case of the surrounding crystal, fringes of the lattice spacing. In these examples

the intensity has been normalised so that the most intense pixel is represented by pure white, i.e. the relative intensities are not shown. However, these relative intensities are similar to the free space case where the maximum intensity of the $1s$ to $2p_z$ case is about 1/2 to 1/3 that of the $1s$ to $2p_{\pm 1}$ case at $Z = 4$.

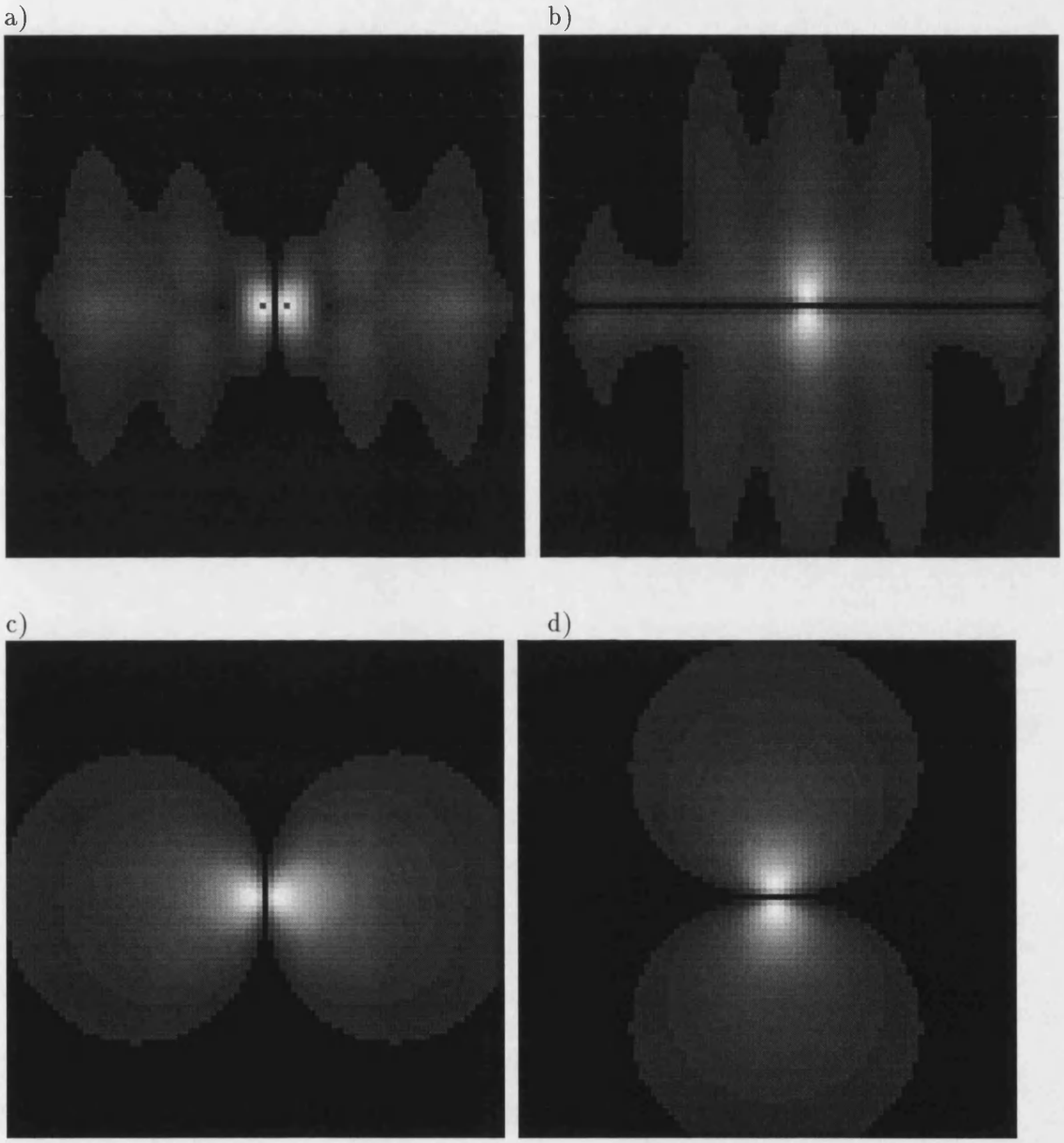

Figure 5.11: $1s$ to $2p_x$(a and c) and $1s$ to $2p_y$ (b and d) object functions for Z=4. a and b are within a crystal, c and d are in free space. The crystal object functions are found at a depth of 150Å, the source atom lies on the crystal plane.

It can be seen from these two examples that the most significant difference between the independent atom and crystal models is the inclusion of fringes at a

spacing equivalent to the distance between atomic planes. Thus the dynamical diffraction does play an important role in the forming of an object function from a source atom in a crystal.

5.3 Moving the Source Atom

In the above cases the source atom was positioned on a crystal plane, however, we are free to move it anywhere within the crystal. Because of the diffraction conditions we have chosen, only movement in the x and z directions will have any effect on the final object function.

5.3.1 Movement in the x-y Plane

In figure 5.12 we can see the effect of moving the source atom to the central point between planes. All other conditions are identical to figure 5.10b i.e. a crystal of Si surrounding the source atom which is at a depth of 150Å and the transition is the $1s$ to $2p_z$ at energy loss of 160eV (Z=4). It can clearly be seen that the bright spot has moved from the central point on the fringe to an intermediate point between fringes. This indicates that the interaction between the source atom and the fast electron is at least partially localised to within a lattice spacing since a fully delocalised interaction would result in the similar patterns being produced whether the atom was on or between planes. This has been done for the other $1s$ to $2p$ transitions with similar movement of the bright spot being found.

5.3.2 Moving the Source Atom to Different Depths

So far we have concentrated on looking at the effect of the surrounding lattice on a source atom in a single z plane within the crystal i.e. $z_0 = 150$Å however, this

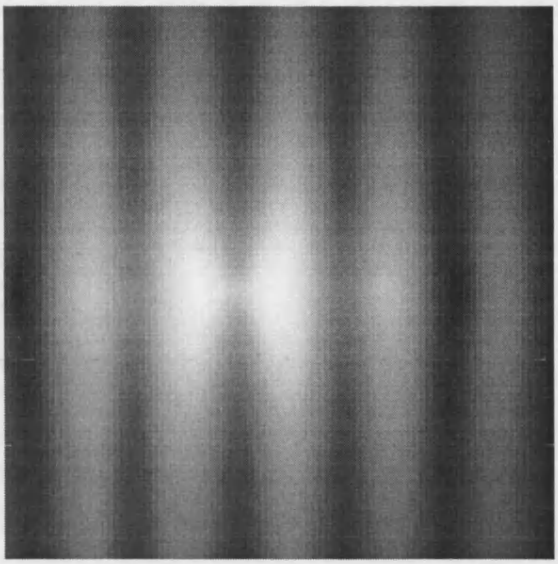

Figure 5.12: $1s$ to $2p_z$ transition with Z=4. The source atom is between planes in this example.

does not reveal where the fringes are coming from. It may be that the dynamical diffraction before the fast electron interacts with the source atom is causing the fringes or it may be the diffraction afterwards or it may be a combination of both. We are able to investigate this point by adjusting the depth of the source atom using the present model. Figure 5.13 shows a sequence of object functions with the source atom moving from the top of the crystal to the bottom. The transition is the $1s$ to $2p_z$ with the source atom placed between atomic planes and with an atomic number of 4 corresponding to an energy loss of 160eV. The depths are a)0Å b)100Å c)200Å d)300Å e)400Å f)500Å. In this case the relative intensities have been preserved between images.

a)

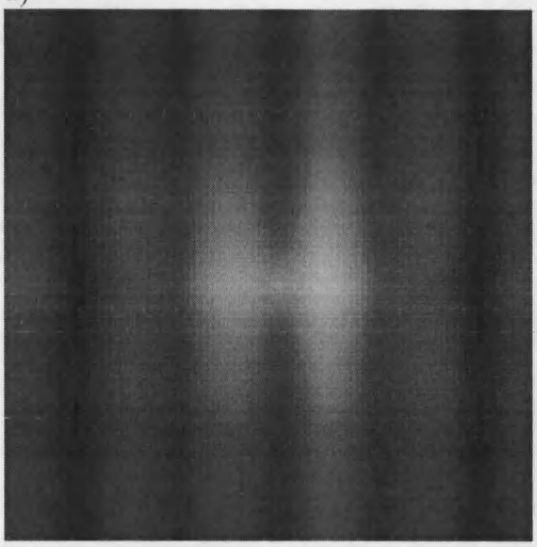

b)

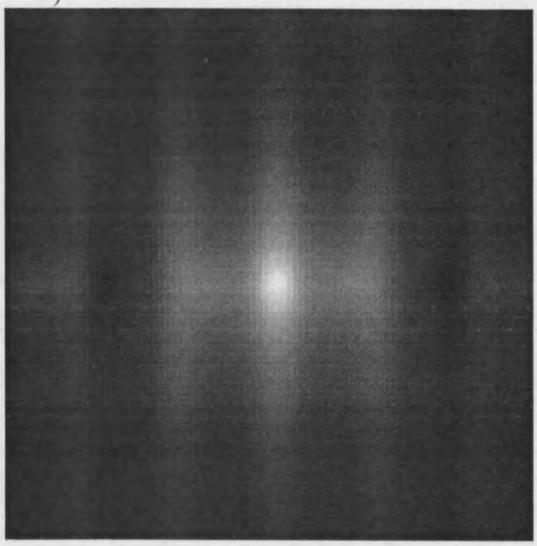

c)

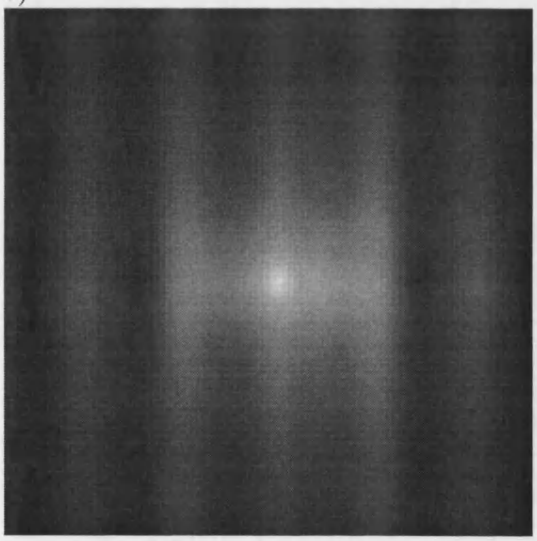

d)

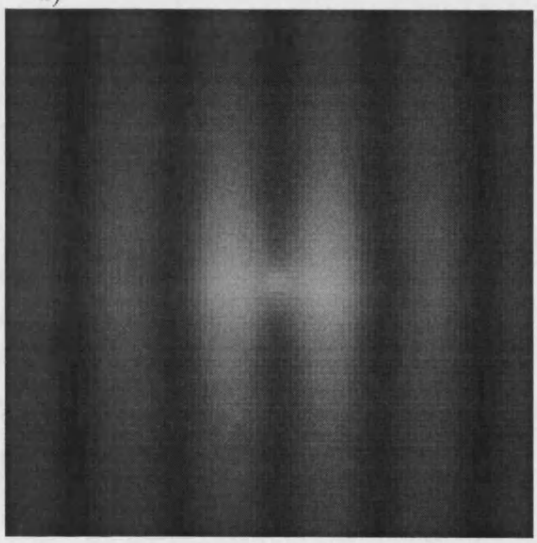

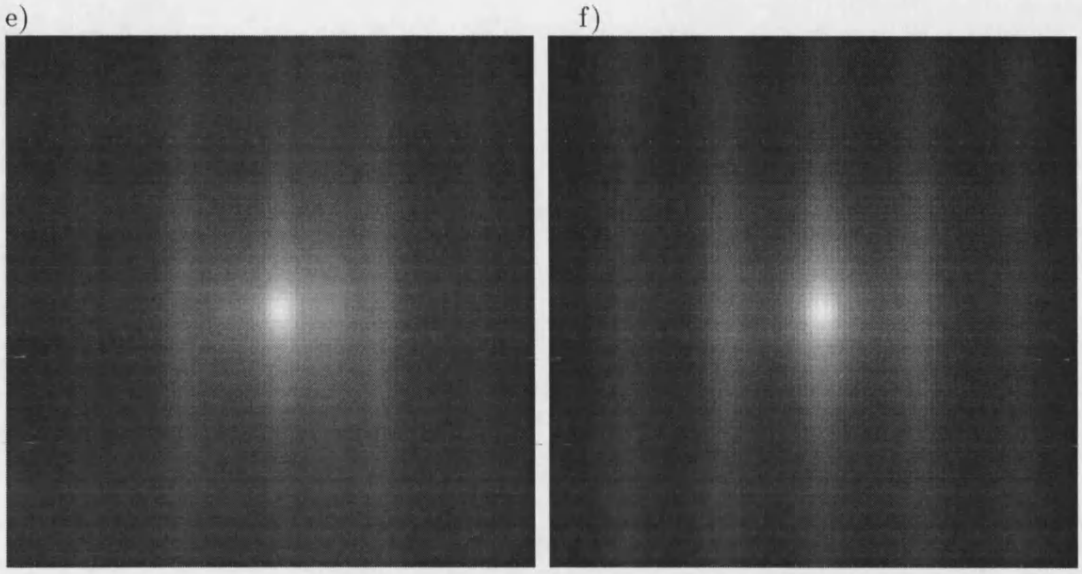

Figure 5.13: $1s$ to $2p_z$ transition showing variation in intensities and fringes through the depth.

There are a number of points which this sequence brings out. First, there is a significant change in intensity through the sequence. The line graph in Figure 5.14 shows this more clearly. The maximum intensity of the object function is displayed with the source atom placed at 50 equally spaced depths through the crystal. The intensity variation is shown with the source atom both placed on a crystal plane and between crystal planes.

It is noticeable that the wavelength of this intensity variation is comparable to the extinction distance of a Bloch wave [21]. To investigate if this is the cause of the intensity variations the incident Bloch wave, $|\Psi(\mathbf{R}_0, z)|^2$ at $x = 0$ (off plane) and $x = 0.5$ (on plane) has been plotted in figure 5.15. Comparisons of these graphs clearly shows that when the Bloch wave is at a maximum over the position of the source atom the corresponding intensity pattern is also at a maximum. Therefore, it is reasonable to assume that the intensity of the incident Bloch wave at the position of the source atom plays an important role in dictating the final intensity of the pattern.

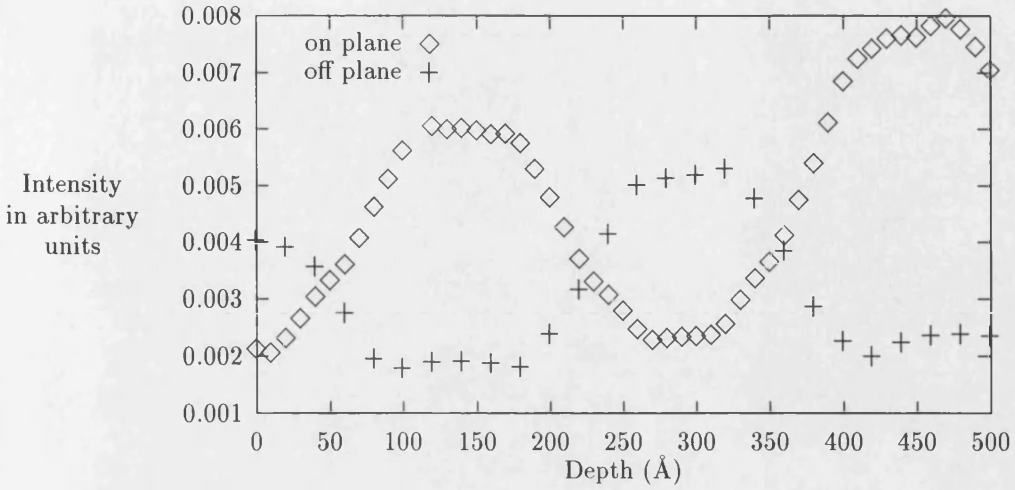

Figure 5.14: Intensity variation of $1s$ to $2p_z$ transition as a function of depth for the $x = 0$ (off plane) and $x = 0.5$ (on plane) condition.

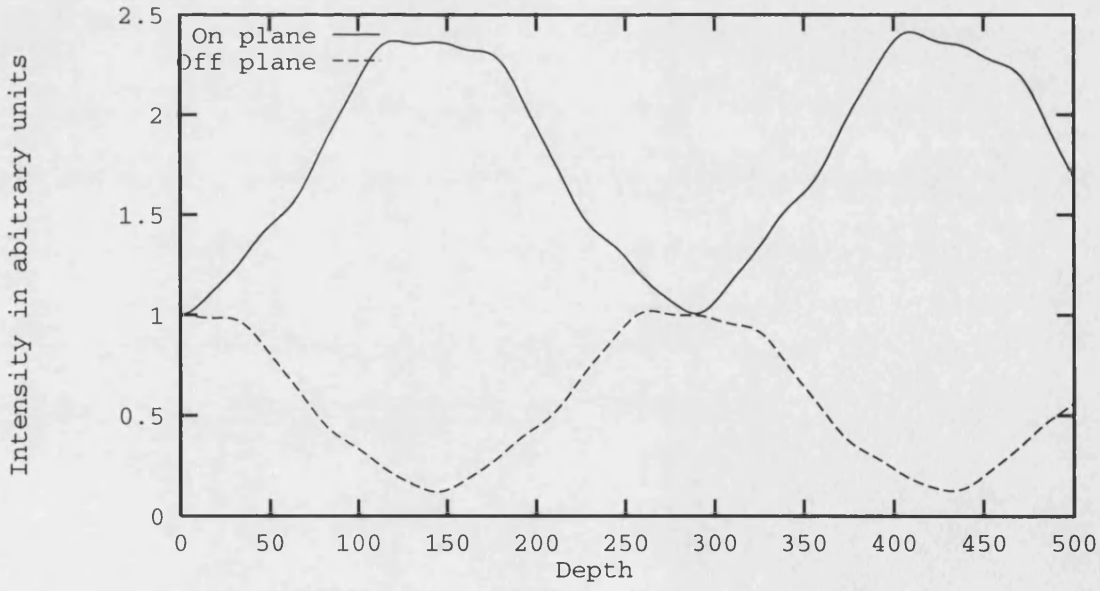

Figure 5.15: Bloch wave intensity on and off plane for 500Å Si crystal in the $(2\bar{2}0)$ systematic row configuration.

5.3.3 Using a Single Focus

Another striking feature of the sequence shown in figure 5.13 is the way in which the source atom appears to move from being between fringes to being on a fringe. Clearly the source atom does not move and it must be the fringes which are reversing their contrast as happens in High Resolution Electron Microscopy (HREM). It was explained in section 4.4 that the object function is given by focusing it onto the position of the source atom. Figure 5.16 shows the same sequence as figure 5.13 with the focus set to 250Å and without showing the relative intensities. As expected the patterns become defocused away from the centre of the crystal but the source atom remains between fringes throughout. This indicates that the focusing of the object function onto the source atom causes the fringe reversal as is observed in conventional HREM. If the maximum intensity is also plotted, see figure 5.17, this reveals that the variation in intensity is smaller than for the ideally focused case although the intensity values are also lower.

a) b)

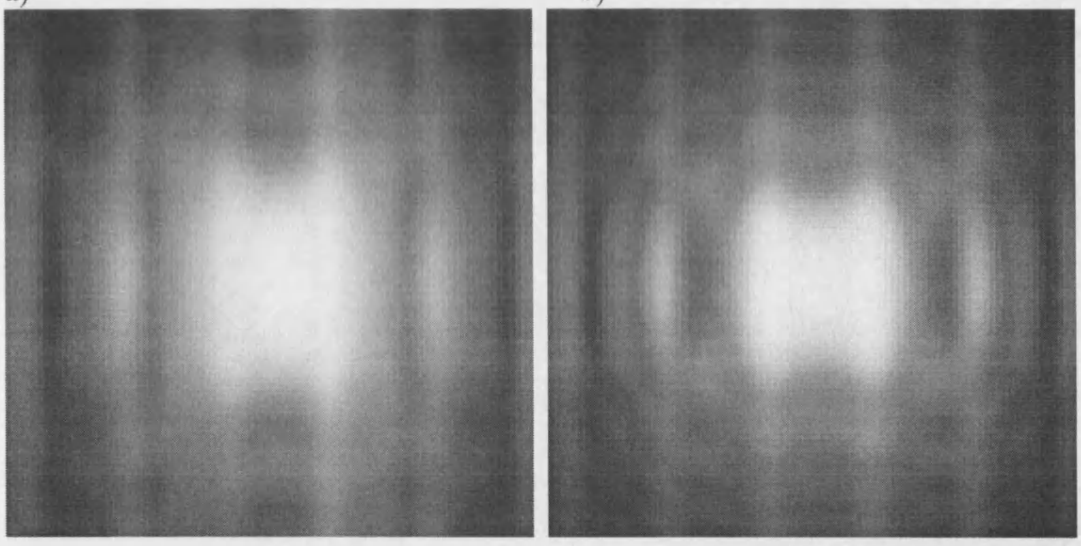

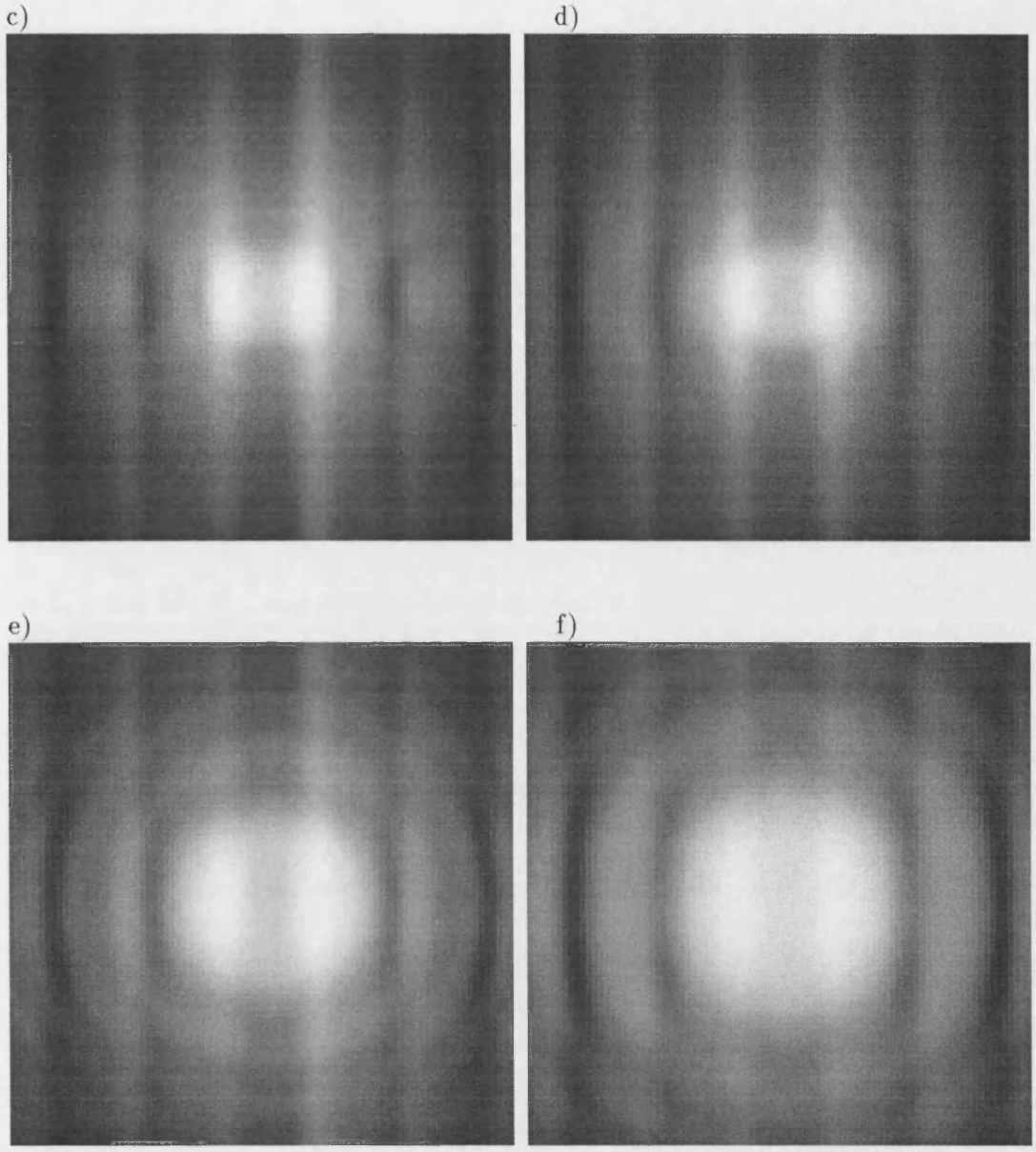

Figure 5.16: Series of $1s$ to $2p_z$ transitions at various depths through the crystal, see text for details.

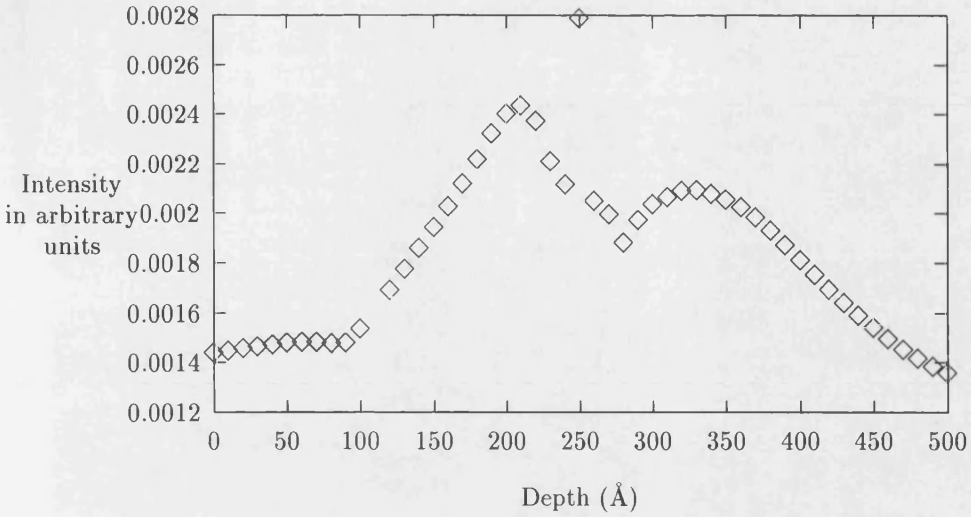

Figure 5.17: Plot of intensities of $1s$ to $2p_z$ transition for a single focus of 250Å at x=0.

Another important point that can be seen from figure 5.13 is that the pictures with the source atom at the top of the crystal and at the bottom of the crystal both display the characteristic background fringes associated with the crystal object function. This implies that there is a much more complicated interaction than the simple explanation that the fringes are due to dynamical diffraction effects after the interaction of the fast electron with the source atom.

The above set of results reveal a number of important restrictions on how well an image of an atom can be seen. First, the fall off in intensity is not as sharp as for the free space model due to the background fringes. Therefore, the image has a slightly larger spatial extent than the free space object functions. Second, the intensity varies with the depth of the source atom. However, if the image is focused onto a single plane as in figure 5.16 then the intensity variation is much less (figure 5.17) although the resolution is not as good with the image spreading out due to defocus. This combination of image spread due to background fringes and defocus as well as the variation of intensity due to depth may make atomic resolution difficult using this method. One recent claim of atomic resolution is investigated in the next section. As explained previously, only one transition

and one energy loss have been shown here to keep the number of results to a realistic level, however, the broad conclusions are the same for other transitions and energy losses.

5.4 Inelastic Imaging of Whole Crystals

So far we have considered a single impurity atom within a surrounding crystal. Endoh et al [1] extended the use of energy loss images to considering whether the whole crystal could be imaged in this way. He used a Si crystal and concluded that the bright spots which appeared in the images are the images of individual atomic columns containing Si atoms. However, we have seen from the work in section 5.2.2 that dynamical diffraction effects produce fringes at a distance of an atomic plane. If these fringes are intense enough then it may be that these bright spots appearing in the images in the paper by Endoh et al are not images of individual atomic columns and this type of high resolution chemical imaging is not possible.

It is possible to use our model developed in section 4.2.3 to examine the possibility of this type of high resolution chemical mapping. To do this we need to take the images at a set of depths and add them together. The calculations we have been using up until now have assumed a systematic row as the diffraction condition. If we are considering a column it may appear that this geometry is no longer valid. However, to investigate the importance of the fringes it is not necessary to accurately describe the system used by Endoh et al. Rather, we need a source of inelastic electrons so that we can see how important the fringes arising from the dynamical diffraction are.

There are three stages to this analysis. First, we must add several images together through the thickness of the crystal in order to determine the intensity of the fringes which arise. Clearly a single focus must be taken as would be the case in a

real system. For this analysis we have taken the $1s$ to $2p_z$ transition and an atomic number of 4. The focus has been set to 250 Å, half way through the crystal. The relative intensity of the fringes with respect to the central bright spot is crucial in determining whether high resolution chemical mapping can be achieved this way. Therefore, no gamma correction factor has been used during this section. Figure 5.18 shows the integration through depth of the object functions. It can be seen that the brightest fringes are in the centre but that image is very localised as expected from the previous work.

The second stage of this analysis consists of adding a set of these depth integrations along a row with inter atomic spacing as would be the case in the work of Endoh et al. Because the fringes have the same spacing so they will also add to the intensity at the bright spots. Figure 5.19 shows a row of these columns.

The final part of this analysis is to remove one column and compare the resulting intensities at this column with the surrounding columns. This is shown in figure 5.20. It can be seen that while the intensity at the missing column does fall off it would be difficult in practice to distinguish the difference between figure 5.19 and figure 5.20. It must be concluded, therefore, that it is not possible to produce the high resolution chemical maps using the method suggested by Endoh et al.

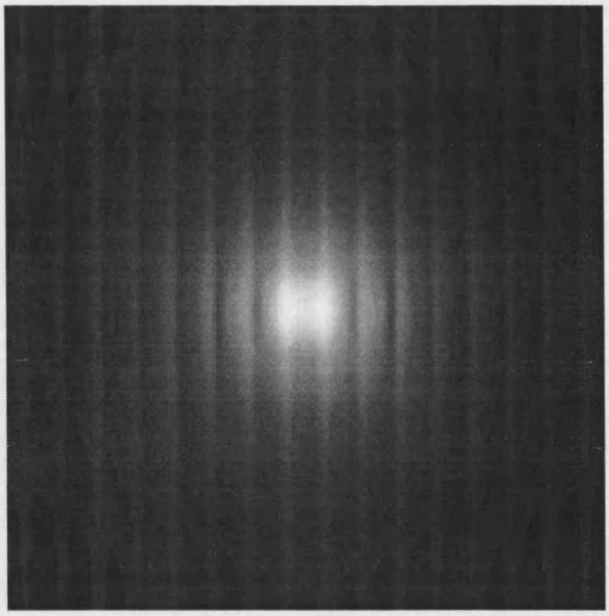

Figure 5.18: Column of source atoms for $Z = 4$ and the $1s$ to $2p_z$ transition, the focus is on 250Å. The same fringes are present as for single impurity atoms.

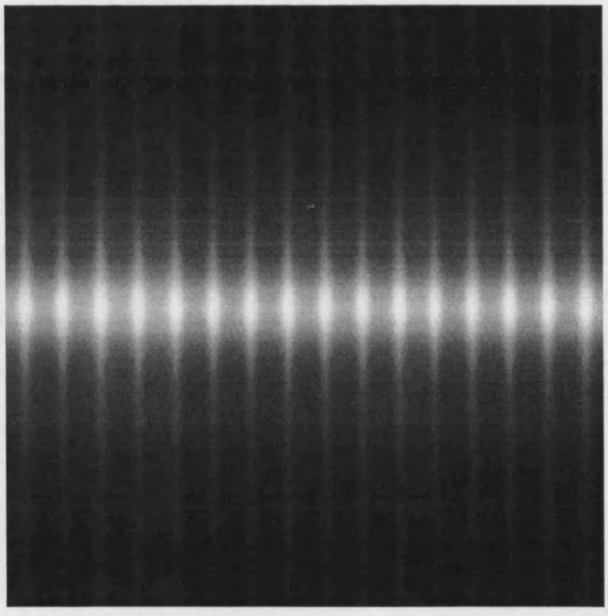

Figure 5.19: Shows a row of columns of source atoms as in figure 5.18.

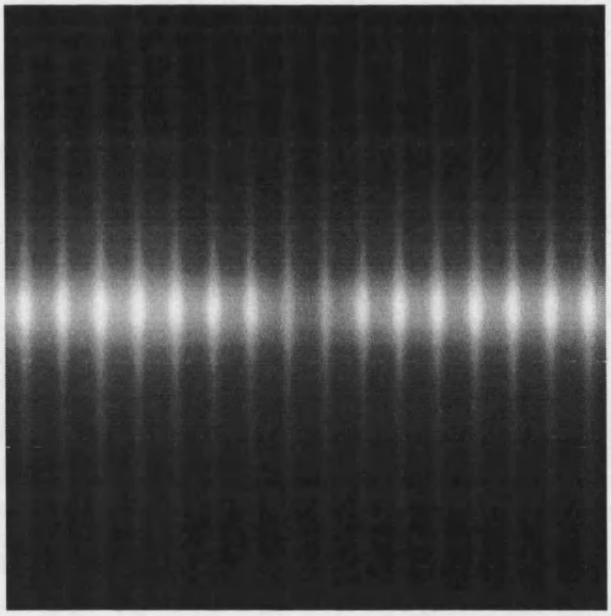

Figure 5.20: One column of source atoms has been removed completely, compare with figure 5.19.

5.5 Summary

In this chapter we have tested assumptions and applied the models developed in the last chapter. Initial tests showed that a relativistic correction factor was required but that the dipole approximation was a good one. These initial investigations into the free space model also revealed that the object functions were well localised and that it may be possible to resolve images from adjacent atoms within a crystal. However, it was also shown that for low energies and small collection angles the image becomes more spread out and resolution is degraded.

Comparisons were then made between the free space and crystal object functions which showed that the inclusion of a crystal causes fringes on the object function. It was shown that the bright centre of the object function moved as the source atom was moved in the x-y plane indicating that the interaction between the fast electron and source atom was localised to some extent to within an atomic spacing. Additionally, as the source atom was moved to different depths through the crystal the intensity varied by 2 to 3 times. It was shown that this variation was due to a large extent to the variation of the incident Bloch wave through the

crystal. Fringe reversal was also noted as the source atom was moved through the crystal, but this could be prevented by choosing a single focus. A single plane for the focus was also shown to reduce the variation in intensity under some circumstances although the resolution was also degraded.

One way of overcoming this variation was to integrate over the depth of the crystal, although this requires columns of atoms. In this case the resolution was affected due to the single focus. It was demonstrated that if a number of columns were close to one another this would lead to the fringes adding constructively, making it appear that there were atomic columns present even if this was not the case. This showed that high resolution chemical imaging of whole crystals could not be achieved in this manner.

Chapter 6

Conclusions

It has been shown that an energy filter combined with a CCD is a vital piece of equipment when studying crystalline materials quantitatively. It increases the accuracy with which we can study elastic and inelastic scattering of electrons by a crystal. This thesis has concentrated on two areas where energy filtering has been used. That is, in structure factor determination using elastic scattering and chemical mapping via inelastic scattering.

6.1 Elastic Scattering

It was first shown that energy filtering allows us to study the distribution of electronic charge within a crystalline material and hence gain a better understanding of atomic bonding within that crystal. This is achieved using the CBED pattern matching method of Bird and Saunders. To be able to use this method we needed to have a number of factors in place. First, only elastic scattering could be considered, inelastic events will disrupt the scattering of the electrons and make it very difficult to interpret the final electron intensity patterns. This requires energy filtering to be used where most of the collected electrons have only been elastically scattered. Hence, contrast is preserved and comparisons can be

made between theory and experiment. Next, we must have an accurate theory for elastic scattering so that we can compare the energy filtered results with the theory. The theory of elastic scattering in a perfect crystal has been understood for some time and is developed in chapter 2.

Structure factor determination using CBED has the advantage that small areas of near perfect crystal can be used in experiment to ensure that the theory and experiment are as close as possible. The method used by Bird and Saunders calculated the theoretical electron intensity pattern using free atom structure factors. It then uses the quasi Newton minimisation routine to alter the free atom values until the best fit between theory and experiment is found. This defines the 'best fit' structure factors and, consequently, atomic bonding. Using this method has two advantages. First, CBED produces detailed intensity patterns, ideal for pattern matching. Second, the method uses a crystal zone axis ensuring that there is a large amount of dynamical diffraction, i.e. the electrons are diffracted through the relevant scattering vectors more often than for the systematic row approach, increasing accuracy. The theory for CBED was developed in chapter 2 where it is shown that to calculate the pattern a many beam matrix must be solved. However, this method can be very time consuming. By using a zone axis the calculations of the CBED pattern must use a large number of beams, making the many beam matrix large. The time taken to solve this matrix scales as N^3 where N is the order of the matrix and the calculation time can become prohibitively slow.

Previously, second order perturbation theory had been successfully applied as a means of overcoming this limitation. However, the quasi Newton minimisation method requires the gradients of the structure factor values with respect to the total error to be known. An analytic expression for these gradients had been developed for use with second order perturbation theory but was only exact while the eigenvectors were unperturbed, i.e. only the eigenvalues could be perturbed. In chapter 3 the Bethe approximation was investigated as an alternative approach. In this approximation the eigenvectors are altered, making the analytic gradients

inexact but improving the accuracy of the eigenvectors used in the amplitude equation. A set of tests were performed to ensure that the Bethe approximation gave improved performance over the original second order method. These tests were used to show

- Under what conditions the approximations break down
- Relative convergence of methods for different materials
- Accuracy of new gradients using Bethe approximation
- How well the theoretical pattern would converge for a realistic system

Initially, a very simple case was taken where only three beams were considered, two diffracted strongly and one weakly. It was shown that while the analytic solutions to the many beam matrix (now a three beam matrix) were different, expanding the Bethe approximation to the second order gave similar expressions for the eigenvalues. The intensity values produced using the two approximations were then compared for a range of diffraction conditions, i.e. the strength of the diffraction into the third beam was altered. It was shown that the second order value would blow up as the approximation became invalid, whereas the Bethe approximation did not. Thus the second order approximation requires an additional subjective cut off between the inner and outer beam set where the original eigenvalues are left unperturbed, this is likely to reduce the accuracy of this method.

Next a more realistic system was considered with several hundred beams included. An 'experimental' pattern was calculated using independent atom structure factors and a large number of beams. The number of inner beams required by each method for convergence was investigated. It was found that for both a Si and Ga As test crystal the Bethe approximation converged more quickly. This allowed fewer beams to be included in the matrix diagonalisation and reduced calculation time. However, this only demonstrated that the Bethe approximation could cal-

culate a single pattern with fewer beams. In order to determine atomic bonding it was necessary to alter the low order structure factors to produce a best fit with experiment. The quasi Newton minimisation routine was used to for this but this required the gradient of each structure factor being altered with respect to the χ^2 error to be calculated. Analytic gradient expressions had been developed for the original second order perturbation approximation, however these were no longer exact for the Bethe approximation and it was important to show that they were not significantly altered by the use of the Bethe approximation. The structure factors which were used to calculate the 'experimental' pattern were randomly altered and the pattern recalculated using the Bethe approximation. The gradients produced using the Bethe approximation were compared to numerical gradients and shown to vary by less than 0.3%, indicating that these gradients could be used. Finally, the calculation was allowed to run to completion and the resulting values for the structure factors were found to be very close to those used in the original calculation.

Finally, this method was used with real experimental data in a Si system. The structure factors found were in close agreement with results from previous X-ray analysis.

It has been shown that the pattern matching technique of Bird and Saunders can be used to determine the low order structure factors and, therefore, the bonding of atoms within a crystal. This relies on accurate collection of experimental elastic data using CCD cameras and energy filtering. The Bethe approximation method should be used to reduce calculation time since it has been shown to give a converged pattern with fewer beams without any detrimental effect on the minimisation routine.

6.2 Inelastic Scattering

The second situation in which the energy filter combined with the CCD has been shown to be of great value is in the study of inelastically scattered electrons and how these provide information about the crystal under study. In particular, the excitation of core electrons allows chemical maps of the crystal to be made. These maps have been used to examine the elemental make up of a material to a few nm resolution. Resolution depends upon a number of factors. First, the inelastic image must be clear, this requires energy filtering to eliminate the elastically scattered electrons and the inelastically scattered electrons of different energy and a CCD to collect the image data. Next, the microscope parameters such as chromatic aberrations have been shown to play an important role in limiting the maximum resolution which these maps can achieve. Finally, even if perfect energy filtering were achieved and an ideal microscope was used there would still be a limit to the resolution of these maps due to the underlying physics of the scattering processes. These underlying limits were investigated here.

In order to investigate these physical limitations it was necessary to create a theoretical model of the inelastic scattering. Unlike the first section, we were not trying to reproduce an exact experimental situation but rather determine what limited the resolution of these experimental images. Therefore, it was necessary only to obtain a source of inelastically scattered electrons rather than exactly model the inelastic process. This enabled a number of approximations to be used. First, the source atom was assumed to by hydrogenic, allowing the energy loss to be altered by changing the atomic number of this atom. Second, the atomic excitation was considered to be from one bound state to another rather that from a bound state to a free state. Third, the imaging process was considered to be perfect, i.e. the object function was found rather than an image. Finally, the dipole approximation was assumed. This model was developed in chapter 4.

In this first model the source atom was considered as being independent from

other atoms and therefore, not subject to any elastic diffraction effects. In chapter 5 some of the assumptions which were made in the model were tested and it was shown that the dipole approximation did not significantly affect the resulting object function and could therefore, be used in the rest of the work.

A second model was developed in chapter 4 which was similar to the first model but included a surrounding crystal. Again several approximations were made The surrounding crystal was chosen to be Si but since only the independent atom values for the Si structure factors were readily available these were used. The crystal orientation was chosen along the $1\bar{1}0$ direction and diffraction was allowed on only the 6 strongest $\mathbf{G}$ vectors. i.e. from $\bar{6}60$ to $6\bar{6}0$.

The independent atom model was used to show that, depending on the energy loss, images from core loss excitation will be localised to within $\sim$ 1 to 2Åwith the spread increasing as the objective aperture decreases below 20mrads. Results from the two models were then compared and it was found that the addition of the surrounding crystal made the image formation much more complicated with fringes now being present around the central bright spot. The intensity of the image varied strongly as a function of depth due to variation of the Bloch wave intensity as a function of depth. Changing the depth of the source atom also caused the fringes to reverse contrast but it was shown that this contrast reversal was stopped if a single focus was taken. A single focus also tended to reduce variations in the intensity but caused the object function to become less localised. Thus reducing the capability of atomic resolution images. It was also found that the interaction of the fast electron and the source atom was localised to within an atomic layer since moving the source atom from on plane to between planes resulted in different object functions. While these were the important differences noted from the models it was also possible the use use these model to investigate claims of atomic resolution.

It had been stated that imaging the crystal atoms themselves would allow atomic resolution to be attained. However, the results described above indicate that

the fringes, intensity variations and increased spread at a single focus may make atomic resolution imaging very difficult. Therefore, to investigate this claim a set of object functions varying in depth but with a single focus were calculated. These functions were then added in intensity, effectively giving a column of source atoms. Finally, a number of these columns were added together separated by the atomic spacing of a Si 110 systematic row axis. It was found that removal of a single column did not make a significant difference to the final pattern, indicating that claims of atomic resolution were not accurate.

6.3 Summary

The energy filter does not rank as one of the great breakthroughs of 20th century science, however, it has been demonstrated in this thesis that for the electron microscope and our over all understanding of crystalline materials it is a very important tool. Both elastic and inelastic events can be studied in greater detail allowing us to understand the atomic bonding of crystalline materials and their chemical make up more accurately than ever before.

Appendix A

Derivation of the Three Beam Analytic Expressions

In this appendix we derive expressions for the change in eigenvalue for the three beam system of section 3.5.1. This will be done for both second order perturbation theory and the Bethe approximation.

The full matrix of our three beam case can be written,

$$H = \begin{pmatrix} w - s^j & U_1 & U_2 \\ U_1 & -w - s^j & U_2 \\ U_2 & U_2 & \beta - s^j \end{pmatrix}. \tag{A.1}$$

If this is split into two components as in section 3.4.3 we get

$$H^0 = \begin{pmatrix} w - s^j & U_1 & 0 \\ U_1 & -w - s^j & 0 \\ 0 & 0 & \beta - s^j \end{pmatrix} \tag{A.2}$$

and

$$V = \begin{pmatrix} 0 & 0 & U_2 \\ 0 & 0 & U_2 \\ U_2 & U_2 & 0 \end{pmatrix}. \tag{A.3}$$

Considering second order perturbation first the eigenvalue is given by,

$$s^j = s_0^j + \sum_{i \neq j} \frac{\langle j|V|i\rangle^2}{s_0^j - s_0^i} \tag{A.4}$$

where j represents the inner beam set and i the outer beam set. The change in the eigenvalue can be written as,

$$\delta s = \frac{|V'_{ij}|^2}{s_0^j - s_0^i} \tag{A.5}$$

where i has only 1 value in this case allowing the sum over i to be dropped, V' is found from the matrix formed by the operation$\Psi^\dagger V \Psi$ where Ψ is the normalised eigenvector matrix formed by diagonalising the inner matrix H^0. Diagonalising H^0 gives $s^j = \pm(w^2 + U_1^2)^{1/2}$ and an eigenvector matrix of,

$$\Psi = \begin{pmatrix} -U_1 & -U_1 & 0 \\ w - (w^2 + U_1^2)^{1/2} & w + (w^2 + U_1^2)^{1/2} & 0 \\ 0 & 0 & 1 \end{pmatrix}. \tag{A.6}$$

However, for V' to be defined as $\Psi^\dagger V \Psi$, Ψ must be normalised. Substituting $\kappa = (w^2 + U_1^2)^{1/2}$ gives Ψ as,

$$\Psi = \begin{pmatrix} \frac{-U_1}{(2(\kappa^2 - w\kappa))^{1/2}} & \frac{-U_1}{(2(\kappa^2 + w\kappa))^{1/2}} & 0 \\ \frac{w-\kappa}{(2(\kappa^2 - w\kappa))^{1/2}} & \frac{w+\kappa}{(2(\kappa^2 + w\kappa))^{1/2}} & 0 \\ 0 & 0 & 1 \end{pmatrix} \tag{A.7}$$

and

$$\Psi^\dagger = \begin{pmatrix} \frac{-U_1}{(2(\kappa^2 - w\kappa))^{1/2}} & \frac{w-\kappa}{(2(\kappa^2 - w\kappa))^{1/2}} & 0 \\ \frac{-U_1}{(2(\kappa^2 + w\kappa))^{1/2}} & \frac{w+\kappa}{(2(\kappa^2 + w\kappa))^{1/2}} & 0 \\ 0 & 0 & 1 \end{pmatrix}. \tag{A.8}$$

It is now possible to form $\Psi^{\dagger}V\Psi$ with the above matrices and therefore obtain the change to the eigenvalue. $\Psi^{\dagger}V\Psi$ is given by,

$$\Psi^{\dagger}V\Psi = \begin{pmatrix} 0 & 0 & \frac{U_2(-U_1+w-\kappa)}{(2\kappa^2-2w\kappa)^{1/2}} \\ 0 & 0 & \frac{U_2(-U_1+w-\kappa)}{(2\kappa^2+2w\kappa)^{1/2}} \\ \frac{U_2(-U_1+w-\kappa)}{(2\kappa^2-2w\kappa)^{1}/2} & \frac{U_2(-U_1+w-\kappa)}{(2\kappa^2+2w\kappa)^{1}/2} & 1 \end{pmatrix}. \tag{A.9}$$

δs^1 is now given by $\sum_i |V'_{ij}|^2/s_0^j - s_0^i$. For an Hermitian matrix the sum over i means that for the first eigenvalue all the components in the first row of $\Psi^{\dagger}V\Psi$ must be squared and added together, similarly for the second eigenvalue all the components in the second row must be squared and added. Thus the change in s^1 is given by,

$$\delta s^{(1)} = \frac{(U_2(w-\kappa-U_1))^2}{2(\kappa^2-w\kappa)(\kappa-\beta)}. \tag{A.10}$$

If κ is replaced with it's original definition of $(w^2+U_1^2)^{1/2}$ and the expression is simplified we get,

$$\delta s^{(1)} = \frac{-U_2^2(w^2+U_1^2)^{1/2} - U_1U_2^2}{\beta(w^2+U_1^2)^{1/2} - (w^2+U_1^2)}. \tag{A.11}$$

The full expression for $s^{(1)}$ can be written as,

$$s^{(1)} = (w^2+U_1^2)^{1/2} + \frac{U_2^2(w^2+U_1^2)^{1/2} + U_1U_2^2}{(w^2+U_1^2) - \beta(w^2+U_1^2)^{1/2}} \tag{A.12}$$

Similarly the change in the second eigenvalue can be found and is given by,

$$s^{(2)} = -(w^2+U_1^2)^{1/2} + \frac{U_2^2(w^2+U_1^2)^{1/2} - U_1U_2^2}{(w^2+U_1^2) - \beta(w^2+U_1^2)^{1/2}}. \tag{A.13}$$

These are the changes that second order perturbation theory introduces into

the three beam case of section 3.5.1. Although the Bethe approximation uses a different approach to changing the eigenvalues it is still possible in the simple three beam case to find an expression giving the changes in eigenvalues. Consider the full 3×3 H matrix given in equation (A.1) above, given the equation $H-s\Psi = 0$ then the third row is equivalent to the equation,

$$U_2C_0 + U_2C_1 + (\beta - s)C_2 = 0. \tag{A.14}$$

If we make the assumption that $\beta \gg s$ then this can be rearranged to to define C_2 in terms of the other components i.e. ,

$$C_2 = -\frac{U_2}{\beta}(C_0 + C_1). \tag{A.15}$$

Now consider the first two rows which are given by,

$$(w - s)C_0 + U_1C_1 + U_2C_2 = 0$$

and

$$U_1C_0 + (-w - s)C_1 + U_2C_2 = 0.$$

If the right hand side of equation (A.15) is substituted into the above equations they become,

$$(w - s - \frac{U_2^2}{\beta})C_0 + (U_1 - \frac{U_2^2}{\beta})C_1 = 0$$

and

$$(U_1 - \frac{U_2^2}{\beta})C_0 + (-w - s - \frac{U_2^2}{\beta})C_1 = 0.$$

The matrix can now be considered to be a 2×2 matrix which is the particular form of the general equation (3.19) in chapter 3. It is written,

$$\begin{pmatrix} w - U_2^2/\beta - s^j & U_1 - U_2^2/\beta \\ U_1 - U_2^2/\beta & -w - U_2^2/\beta - s^j \end{pmatrix} \tag{A.16}$$

The eigenvalues and eigenvectors of our system are now given by diagonalising this matrix. This gives the value of the eigenvalues as,

$$s^j = -\frac{U_2^2}{\beta} \pm \frac{1}{2}\left(\frac{4U_2^2}{\beta} - 4(\frac{2U_1U_2}{\beta}) - w^2 - U_1^2\right)^{\frac{1}{2}} \tag{A.17}$$

Here, we are particularly interested in comparing the eigenvalue expression with that from second order perturbation theory. Therefore, we expand the determinant of this matrix to give,

$$(w - \frac{U_2^2}{\beta} - s)(-w - \frac{U_2^2}{\beta} - s) - (U_1 - \frac{U_2^2}{\beta})(U_1 - \frac{U_2^2}{\beta}) = 0.$$

Expanding this and neglecting all terms involving U_2^4 which are small gives,

$$s^2 + \frac{2sU_2^2}{\beta} - w^2 - U_1^2 + \frac{2U_1U_2^2}{\beta} = 0. \tag{A.18}$$

This gives the value of s as

$$s = \frac{-U_2^2}{\beta} \pm \sqrt{\frac{U_2^4}{\beta^2} - \frac{2U_1U_2^2}{\beta} - w^2 - U_1^2}. \tag{A.19}$$

However, this is very dissimilar to the second order perturbation theory making it difficult to compare the two. Standard perturbation theory [95] can be applied to this problem in order to produce an analytic solution of the same form as second order perturbation theory. The perturbation expansion,

$$s = s_0 + \delta s_1 + \delta^2 s_2 + \cdots$$

and its square,

$$s^2 = s_0^2 + 2\delta s_0 s_1 + O(\delta^2)$$

can be used to determine s in equation (A.18) if it is noted that $2U_2^2/\beta$ is small and represented by δ. Thus equation (A.18) is now given by,

$$s_0^2 + 2\delta s_0 s_1 + \delta s_0 + \delta^2 s_1 - w^2 - U_1^2 + U_1\delta = 0.$$

To solve this we must first eliminate all δ^2's since they will be small and equate the other coefficients as shown below,

$$\delta^0 : \quad s_0^2 - w^2 - U_1^2 = 0 \quad , s_0 = (w^2 + U_1^2)^{1/2}$$

$$\delta^1 : \quad 2s_0 s_1 + s_0 + U_1 = 0 \quad , s_1 = \frac{-s_0 - U_1}{2s_0}.$$

s is defined as $s_0 + \delta s_1$ so by replacing δ with $2U_2^2/\beta$ gives the two eigenvalues of the system as,

$$s^{(1)} = (w^2 + U_1^2)^{1/2} + \frac{2U_2^2}{\beta}\frac{(-(w^2 + U_1^2)^{1/2} - U_1)}{2(w^2 + U_1^2)^{1/2}}$$

$$s^{(2)} = -(w^2 + U_1^2)^{1/2} + \frac{2U_2^2}{\beta}\frac{((w^2 + U_1^2)^{1/2} - U_1)}{-2(w^2 + U_1^2)^{1/2}}.$$

Simplifying and rearranging these expressions gives,

$$s^{(1)} = (w^2 + U_1^2)^{1/2} + \frac{U_2^2(w^2 + U_1^2)^{1/2} + U_1 U_2^2}{-\beta(w^2 + U_1^2)^{1/2}} \qquad \text{(A.20)}$$

and

$$s^{(2)} = -(w^2 + U_1^2)^{1/2} + \frac{U_2^2(w^2 + U_1^2)^{1/2} - U_1U_2^2}{-\beta(w^2 + U_1^2)^{1/2}}. \qquad \text{(A.21)}$$

These consist of the basic eigenvalues which can be obtained by diagonalising the H^0 matrix (the first term on the right hand side) and the changes in this value (second term on the right hand side). These changes are the Bethe approximation equivalent to the $s^{(j)}$ of equations (A.12) and (A.13). The only difference between these equations being that the Bethe approximation assumes that $\beta \gg (w^2+U_1^2)^{1/2}$ and alters the denominator accordingly. However, the true Bethe expression given in equation (A.17) includes all the terms in the expansion, the above equations only include the first term.

References

[1] H. Endoh, H. Hashimoto and Y. Makita (1994) *Ultramic* **56** 108.

[2] W.J. de Ruijter and J.K. Weiss (1992) *Rev. Sci. Instrum.* **63** No. 10 4314.

[3] A.J. Gubbens, O.L. Krivanek (1993) *Ultramicroscopy* **51** 146.

[4] A.J. Gubbens, B. Kraus, O.L.Krivanek and P.E. Mooney (1995) *Ultramic.* **59** 255.

[5] P.A. Doyle and P.S. Turner, (1968) *Acta Crystalogr.* **A24** 390.

[6] J.C.H. Spence, J.M. Zuo (1992) *Electron Microdiffraction* Plenum Press, New York.

[7] J.M. Zuo and J.C.H. Spence (1991) *Ultramicroscopy* **35** 185.

[8] D.M. Bird, M. Saunders (1992) *Ultramicroscopy* **45** 241.

[9] A. Berger and H. Kohl (1992) *Microsc. Microanal. Microstruct.* **3** 159.

[10] H. Kohl and A. Berger (1995) *Ultramicroscopy* **59** 191.

[11] O.L. Krivanek, M.K. Kundmann and K. Kimoto *J. of Microscopy* **180** pt. 3 227.

[12] M. Saunders, D.M. Bird, O.F. Holbrook, P.A. Midgley (1996) *Ultramicroscopy* **65** 45.

[13] M. Saunders, P.A. Midgley, R. Vincent (1995) *Institute of physics conference series* **147** 125.

[14] D.M. Bird, (1989) *J. Electron Microscopy Technique* **13** 77.

[15] D.M. Bird, J.C. Walmsley, R. Vincent (1983) In Electron Microscopy and Analysis 1983 Inst. Phys. Conf. Ser. **68** 41.

[16] B.F. Buxton, (1976) *Proc. R. Soc.* **A350** 335.

[17] A. Howie (1966) *Phil. Mag.* **14** 223.

[18] C.J. Humphreys, (1979) *Rep. Prog. Phys.* **42** 1825.

[19] W. Cochran, H.B. Dyer (1952) *Acta Cryst.* A**24** 390.

[20] R. Vincent, D.M. Bird, J.W. Steeds (1984) *Phil. Mag. A* **50** 765.

[21] N.W. Ashcroft and D.N. Mermin (1976) *Solid State Physics* Holt,Rinehart and Winston, New York.

[22] H. Yoshoka, (1957) *J. of the Physical Soc. of Japan* **12** 618.

[23] G. Radi (1970) *Acta Cryst.* A**26** 41.

[24] P.H. Dederichs (1972) *Solid Stat Phys.* **27** 135.

[25] C.J. Humphries, P.B. Hirsh (1968) *Phil. Mag.* **18** 115.

[26] D.M. Bird and Q.A. King (1989) *Acta Cryst.* A**46** 202.

[27] J.H. Wilkinson (1965) *The Algebraic Eigen Value Problem* OUP.

[28] M. Saunders (1993) *Measurement of Low Order Structure Factors by Convergent Beam Electron Diffraction* University of Bath PhD Thesis.

[29] E. Hecht(1987) *Optics* Addison-Wesley Publishing Reading.

[30] D.M. Bird (1985) *J. Phys. C: Solid State Phys.* **18** 481.

[31] J. Mansfield, D.M. Bird and M. Saunders (1993) *Ultramic.* **48** 1.

[32] P.B. Hirsh, A. Howie, R.B. Nicholson, D.W. Pashley, M.J. Whelan (1965) *Electron Microscopy of Thin Crystals* Butterworths, London.

[33] C.J. Humphries (1979) *Rep. Prog. Phys.* **42** 122.

[34] M.H. Loretto (1994) *Electron Beam Analysis of materials* Chapman and Hall, London.

[35] R.F. Egerton (1986) *Electron Energy Loss Spectroscopy in the Electron Microscope* Plenum Press, New York.

[36] A. Paxton (1992) *Physics World* **5** No. 11 35.

[37] J.M. Zuo, J.C.H. Spence and M. O'Keeffe (1989) *Phys. Rev. Lett.* **62** 2329.

[38] Z.W. Lu, A. Zunger amd M. Deutsch (1993) *Phys. Rev. B* **47** no. 15 9385.

[39] (1990) *Numerical Algorythms Group FORTRAN Library Manual* Mark 14, NAG Ltd, Oxford.

[40] W.H. Press, B. Flannery, S. Teukolsky and W. Vetterling (1986) *Numerical Recipies* Cambridge University Press, Cambridge.

[41] B.F. Buxton, J.A. Eades, J.W. Steeds and G.M. Rackham (1976) *Phil. Trans. Roy. Soc.* **281** 171.

[42] J.C.H. Spence (1993) *Acta. Cryst.* A**49** 231.

[43] P.H. Dederichs (1972) *Solid State Phys.* **27** 135.

[44] J. Daberkov, K.H. Herrmann, Libin Liu and W.D. Rau (1991) *Ultramic.* **38** 215.

[45] W. Nuchter, A.L. Weickenmeier and J. Mayer (1995) *Proc. IOP Elec. Mic. and Anal.* ed. D. Churns No. 147 309.

[46] C. Deininger, G. Necker and J. Mayer (1994) *Ultramic* **54** 15.

[47] M.Saunders, P.a. Midgley, T.D. Walsh, E.S.K. Menon, A.G. Fox and R. Vincent (1997) *Scanning Microscopy Supplement 11, Proc. of 15th Pfeffercorn Conf. on Elec. Image and Sig. Proc.*

[48] D.M. Bird and M. Saunders (1992) *Acta. Cryst.* A**48** 555.

[49] P.E. Gill, W. Murray, M.H. Wright (1981) *Practical Optimization*, Academic Press, London.

[50] L.I. Schiff (1968) *Quantum Mechanics* McGraw-Hill Kogakusha, Tokyo.

[51] J.M. Zuo, A.L. Weickenmeier (1995) *Ultrmicroscopy* **57** 375.

[52] C. Birkeland, R. Holmestad, K. Marthinsen and R. Hoier (1996) *ultramicroscopy* **66** 89.

[53] K. Tsuda and M. Tanaka (1995) *Acta Cryst.* **51** pt. 1 7.

[54] R. Holmestad, J.M. Zuo, J.C.H. Spence, R. Hoier and Z. Horita (1995) *Phil. Mag. A* **72** No. 3 579.

[55] L.E. Murr (1982) *Electron and Ion Microscopy and Analysis* Marcel Dekker, New York.

[56] A. Berger and H. Kohl (1993) *Optik* **92** 175.

[57] J.P.R. Bolton and M. Chen (1995) *ultramic.* **60** 247.

[58] S. Tremblay and G. l'Esperance (1994) *Proc. 13th ICEM*, eds. B. Jouffrey and C. Colliex (les editions de Physique) 1 627.

[59] A.P. Somlyo (1984) *J. Ultrastruct. Res.***83** 135.

[60] K.E. Gorlen, L.K. Barden, J.S. Del Priore, C.E. Fiori, C.C. Gibson and R.D. leapman (1984) *Rev. Sci. Instrum.* **55** 912.

[61] P. Rez and C. Ahn (1982) *Ultramic.* **8** 341.

[62] A.J. McGibbon, M.F. Chrisholm and S.J. Pennycook *J. Vac. Sci. Technol. B* **13** no. 4 1751.

[63] P.A. Crozier (1995) *Ultramic.* **58** 157.

[64] K. Kimoto, T. Hiriano, K. Usami and H. Hoshiya (1994) *Jap. J. Appl. Phys.* **33** L1642.

[65] F. Hofer, P. Warbichller, W. Grogger (1995) *Ultramic.* **59** 15.

[66] A. Berger, J. Mayer and H. Kohl (1994) *Ultramic.* **55** 101.

[67] J.C.H. Spence and J. Lynch (1982) *Ultramic.* **9** 267.

[68] J. Silcox, P. Xu and R.F. Loane (1992) *Ultramic.* **47** 173.

[69] P.E. Batson and G. Trafas (1982) *Ultramicroscopy* **8** 293.

[70] A. Howie (1979)*J.Microsc.* **117** 11.

[71] H. Kohl and R. Rose (1985) *Adv. Electr. Electr. Physics* **65** 173.

[72] P.E. Batson (1992) *Ultramicroscopy* **47** 133.

[73] N.D. Browning, M.F. Chrisholm and S.J. Pennycook (1993) **Nature 366** 143.

[74] A.J. Craven (1995) *Inst. of Phys. Conf. Series* **147** 267.

[75] Z.L. Wang and A.J. Shapiro (1995) *Ultramic.* **60** 115.

[76] A. Berger and H. Kohl (1993) *Microsc. Microanal. Microstruct.* **3** 159.

[77] N.D. Brown and S.J. Pennycook (1995) *J. of Microsc.* **180** 230.

[78] S.J. Pennycook (1982) *Contemp. Phys.* **23** 371.

[79] D.A. Muller and J. Silcox (1995) *Ultramicroscopy* **59** 195.

[80] K. Kimoto, T. Hirano and K. Usami (1995) *J. Electron. Microsc.* **44** 86.

[81] R.F. Egerton and P.A. Crozier (1997) *Micron.* **28** No. 2 117.

[82] V.W. Maslan and C.J. Rossouw (1984) *Phil. Mag. A* **49** 735.

[83] C.J. Rossouw and V.W. Maslan (1984) *Phil. Mag. A* **49** 743.

[84] L.D. Landau and E.M. Lifshitz (1976) *A Shorter Course of Theoretical Physics* Pergamon Press, London.

[85] R. Eisberg and R. Resnick (1985) *Quantum Physics of Atoms, Molecules, Solids, Nuclei and Particles* Wiley, Chichester.

[86] E.N.Economou (1990) *Green's Functions in Quantum Physics* Springer-Verlag, London.

[87] M. Abramowitz and I.A. Stegun *Handbook of Mathematical functions with formulas, graphs and mathematical tables* National Bureau of Stndards.

[88] D.M. Bird (1990) *Acta Cryst.* A**46** 208.

[89] F. Hofer and P. Golob (1987) *Ultramic.* **21** 379.

[90] L. Pauling and E.B. Wilson *Introduction to quantum mechanics.*

[91] I.S. Gradshteyn and M. Ryzhik (1980) *Table of integrals, series and products* Academic Press, London.

[92] I.N. Bronshtein and K.A. Semendyayev (1964) *A guide book to Mathematics* Pergamon Press, London.

[93] W. Davidson and J. Poskanzer (1991) *SunOS 5.4 man pages* pnmgamma (1).

[94] M. Saunders (1995) *Private Communication*

[95] A.W. Bush (1992) *Perturbation Methods for Engineers and Scientists* CRC Press, London.